

FLORIDA INTERNATIONAL UNIVERSITY

MIAMI, FLORIDA

EMBEDDED HEAT PIPES IN COFIRED CERAMIC SUBSTRATES FOR
ENHANCED THERMAL MANAGEMENT OF ELECTRONICS

A dissertation submitted in partial fulfillment of the
requirements for the degree of

DOCTOR OF PHILOSOPHY

in

MECHANICAL ENGINEERING

by

Marc Anthony Zampino

2001

To: Interim Dean Richard K. Irey
College of Engineering

This dissertation, written by Marc Anthony Zampino, and entitled Embedded Heat Pipes in Cofired Ceramic Substrates for Enhanced Thermal Management of Electronics, having been approved in respect to style and intellectual content, is referred to you for judgment.

We have read this dissertation and recommend that it be approved.

Yiding Cao

James Moore

Richard K. Irey

Kirk L. Yerkes

W. Kinzy Jones, Major Professor

Date of Defense: April 18, 2001

The dissertation of Marc Anthony Zampino is approved.

Interim Dean Richard K. Irey
College of Engineering

Dean Douglas Wartzok
Graduate School

Florida International University, 2001

© Copyright 2001 by Marc Anthony Zampino

All rights reserved.

DEDICATION

I dedicate this thesis to my late uncle, Giuseppe (Joseph) Agoglia, an Italian immigrant who came to America at the age of two in 1915. He tinkered with all things technical, an inventor out of necessity, and eventually an engineer by trade, but most of all, a dreamer of the future and the technical wonders it would hold and the achievements man would make with his new technologies. In all ways, he was a true engineer, with logical thought, mechanical aptitude, mathematical calculation, and wisdom gained through mentoring and experience. He did not have the opportunity to obtain an engineering degree, denied him by the culture, economics and politics of his time. Nonetheless, I still consider him more of an engineer than most graduates with an engineering degree.

I remember him for teaching me to understand how and why things worked, but more importantly I remember his excitement when we talked about the latest scientific achievements. It was that excitement that led me to my profession in engineering. I knew that my uncle was proud when I received my undergraduate engineering degree. Now, I regret that he was not still alive to see me accomplish my doctoral degree. I reflect on this not out of desire for admiration, but rather because I understand now he would also be getting his doctoral degree, not in reality, but through me, someone he profoundly touched.

ACKNOWLEDGMENTS

I wish to thank my wife, Sandra, for supporting me through this arduous journey, my parents for their support of my educational progress throughout my life, and the members of my committee for their support, insight, and comments. In particular, I would like to thank my Major Professor, Dr. Kinzy Jones, for giving me the project to work on, the latitude to work the project in my fashion, and for just plain putting up with me. Also, I would like to give my appreciation to Mincong Gao, a research colleague, for his assistance in charging the prototype heat pipes. I would like to acknowledge that my research was funded by the U.S. Air Force, Wright Patterson AFB, Contract No. F33615-96-C-2656.

ABSTRACT OF THE DISSERTATION

EMBEDDED HEAT PIPES IN COFIRED CERAMIC SUBSTRATES FOR ENHANCED THERMAL MANAGEMENT OF ELECTRONICS

by

Marc Anthony Zampino

Florida International University, 2001

Miami, Florida

Professor W. Kinzy Jones, Major Professor

A novel and new thermal management technology for advanced ceramic microelectronic packages has been developed incorporating miniature heat pipes embedded in the ceramic substrate. The heat pipes use an axially grooved wick structure and water as the working fluid. Prototype substrate/heat pipe systems were fabricated using high temperature co-fired ceramic (alumina). The heat pipes were nominally 81 mm in length, 10 mm in width, and 4 mm in height, and were charged with approximately 50-80 μL of water. Platinum thick film heaters were fabricated on the surface of the substrate to simulate heat dissipating electronic components. Several thermocouples were affixed to the substrate to monitor temperature. One end of the substrate was affixed to a heat sink maintained at constant

temperature. The prototypes were tested and shown to successfully and reliably operate with thermal loads over 20 Watts, with thermal input from single and multiple sources along the surface of the substrate. Temperature distributions are discussed for the various configurations and the effective thermal resistance of the substrate/heat pipe system is calculated. Finite element analysis was used to support the experimental findings and better understand the sources of the system's thermal resistance.

TABLE OF CONTENTS

CHAPTER	PAGE
I. Introduction.....	1
Background	1
Objectives of the Research	5
Significance of the Research.....	7
II. Literature Review	8
III. Cofired Ceramic Embedded Heat Pipes	19
Cofired Ceramic Substrate Manufacturing	19
Lamination and Firing Processes.....	22
Ceramic Substrate Materials	28
Wetting Angle of Cofired Ceramic Materials	29
General Heat Pipe Operation and Design.....	34
Embedded Ceramic Heat Pipe Design	43
Evolution of Ceramic Heat Pipe Prototypes	47
Fabrication of Embedded Heat Pipe Prototypes.....	50
IV. Modeling and Simulation	57
Theoretical Overview of FEA for Heat Transfer.....	58
FEA Models of Embedded Heat Pipes.....	64
V. Experimental Set-Up and Procedure	76
Experimental Set-Up	76
Uncertainty Analysis	83
Experimental Procedures.....	86
Heat Pipe Samples Tested	88
VI. Thermal Performance Testing.....	92
Overview of Testing.....	92
Comparison of Charged and Uncharged Samples.....	94
Overall Thermal Performance	100
Single Heater Operation	111
Multiple Heater Operation	119
Comparison of Experimental and FEA Results.....	127
System Thermal Resistance	134
VI. Conclusions.....	136
List of References.....	141
Appendix.....	144
VITA	152

LIST OF TABLES

TABLE		PAGE
Table 3-1.	Physical properties for HTCC alumina [Sergent, 1995]	29
Table 4-1.	Comparison of thermal resistance from heater to vapor for various wick structures and dry-out conditions.	69
Table 4-2.	Comparison of conduction only solutions for both heat pipes.	74
Table 5-1.	Summary of elemental uncertainties for measured voltage and current and the propagated error in the heater power calculation.	85
Table 5-2.	Overall dimensions of heat pipe samples.....	88
Table 5-3.	Wick dimensions of the of heat pipe samples.....	89
Table 5-4.	Heater locations on the heat pipe samples.	90
Table 5-5.	Thermocouple (T/C) locations on the heat pipe samples.	90
Table 6-1.	Summary of experimental configurations. Blank indicates no data available for that configuration.....	93
Table 6-2.	Comparison of thermal resistance for various paths through the substrate and the insulation blanket during uncharged heat pipe testing.....	98
Table 6-3.	Summary of calculations for estimating the ambient heat loss through the ceramic from the heater to the heat sink.....	100

LIST OF FIGURES

FIGURE	PAGE
Figure 3-1. Typical cofired ceramic process for multilayer fabrication.	20
Figure 3-2. Lamination stresses in green tape when a cavity exists in the tape stack.	24
Figure 3-3. Schematic showing basic heat pipe operation.	35
Figure 3-4. The effect on the capillary limit due to variations in groove width for groove depths of: (A) 0.64 mm, (B) 0.38 mm, and (C) 0.25 mm.	40
Figure 3-5. The effect on the capillary limit due to variations in vapor space height for groove depths of: (A) 0.64 mm, (B) 0.38 mm, and (C) 0.25 mm.	41
Figure 3-6. The effect on the capillary limit due to variations in vapor space height for groove widths of: (A) 0.10 mm, (B) 0.25 mm, and (C) 0.38 mm.	42
Figure 3-7. Axially cross section of an axially grooved heat pipe with the wick oriented on the top and bottom surfaces of the heat pipe.	44
Figure 3-8. Micrograph showing top/bottom axial groove wick structure fabricated in high temperature cofire ceramic using a micro end-milling process.	45
Figure 3-9. Axial cross-section of a heat pipe with the axial grooves oriented along the side walls.	46
Figure 3-10. Micrograph showing “side-wall” axial groove wick structure fabricated in low temperature cofire ceramic.	46
Figure 3-11. Thick-film platinum heater geometry. Dimensions are in inches.	52
Figure 3-12. Typical artwork for thick film heater metalization on substrate surface.	53
Figure 3-13. Picture of typical assembled heat pipe showing heaters, lead wires, and filling tube.	54
Figure 4-1. Composite showing representative parts of FEA models (HP#7 model shown): One-half symmetry model, mesh detail, and cross-section of model.	65
Figure 4-2. Axial temperature distribution for HP#7 and HP#10 with 10 W thermal load at heater location H1 and three wick conditions.	68
Figure 5-1. Schematic of experimental set up showing major components.	76
Figure 5-2. Schematic of test cell (top) showing heat pipe mounting, cold plate, wiring, lab stand and insulation jacket.	77
Figure 5-3. Cross-section of clamping arrangement used to secure heat pipe to cold-plate. ...	77
Figure 5-4. Heat pipe axial orientation relative to gravity and the axial orientation angular convention.	78
Figure 5-1. Cross-section of HP#7 showing internal geometry for top/bottom grooved wick heat pipe samples. Dimensions shown are in millimeters.	91

Figure 5-2. Cross-section of HP#9 showing internal geometry for side wall grooved wick heat pipe samples. Dimensions shown are in millimeters.	91
Figure 6-1. Conduction mode (uncharged) operation of samples HP#7 and HP#10 at various power levels. A representative comparison is provided for each sample operating with a liquid charge (CH) at 0° axial orientation. Vertical axis has been normalized using the sink temperature.	96
Figure 6-3. Average temperature rise at the evaporator region over the sink temperature for heat pipe samples which had Top-Bottom wick structure.	102
Figure 6-4. Average temperature rise for the evaporator region over the sink temperature for heat pipe samples which had Side-Wall wick structure.	103
Figure 6-5. Temperature distribution for HP#7 with a Top/Bottom wick structure operating at various power levels in both horizontal and vertical (evaporator side down) orientations. Heater is located at x = 20 mm.	107
Figure 6-6. Temperature distribution for HP#10 with a Side-Wall wick structure operating at various power levels in both horizontal and vertical (evaporator side down) orientations. Heater is located at x = 18 mm.	108
Figure 6-7. Comparison of temperature distributions on the heater side (HS) and the condenser side (CS) of the heat pipe for HP#9.	110
Figure 6-8. Temperature distribution along HP#10 for H1 configuration at various power levels for (A) 0° and (B) 90° axial orientation. Heater 1 is located at x=18mm and the sink temperature was 35 °C.	113
Figure 6-9. Temperature distribution along HP#10 for H2 configuration at various power levels for (A) 0° and (B) 90° axial orientation. Heater 2 is located at x=28mm and the sink temperature was 35 °C.	114
Figure 6-10. Temperature distribution along HP#10 for H3 configuration at various power levels for (A) 0° and (B) 90° axial orientation. Heater 3 is located at x=38mm and the sink temperature was 35 °C.	115
Figure 6-11. Average evaporator region for HP#10 for single heater operation. Note: Heater 2 and 3 data combined for fitted line analysis.	117
Figure 6-12. Temperature distribution along HP#10 for H12 configuration at various power levels for (A) 0° and (B) 90° axial orientation. Sink temperature was 35 °C. Heaters are located at x = 18 and 28 mm.	121
Figure 6-13. Temperature distribution along HP#10 for H123 configuration at various power levels for (A) 0° and (B) 90° axial orientation. Sink temperature was 35 °C. Heaters are located at x = 18, 28, and 38 mm.	122
Figure 6-14. Temperature distribution along HP#10 for H1234 configuration at various power levels for (A) 0° and (B) 90° axial orientation. Sink temperature was 35 °C. Heaters are located at x = 18, 28, 38 and 48 mm.	123
Figure 6-15. Average evaporator region temperature for HP#10 for single (H1) and multiple heater configurations. For each heater configuration, data is included for all axial orientations tested.	125

Figure 6-16. Comparison of experimental and numerical temperature data for HP#10 at various axial orientations and single heater configurations. Legend indicates Power Level (W) / Axial Orientation (degrees)..... 129

Figure 6-17. Comparison of experimental and numerical data for HP#10 at various axial orientations and multiple heater configurations. Legend indicates Power Level (W) / Axial Orientation (degrees). 130

LIST OF SYMBOLS

A_C	cross sectional area	(m ² or mm ²)
A_S	surface area	(m ² or mm ²)
D_g	capillary wick groove depth	(m or mm)
D_h	hydraulic diameter	(m or mm)
F	frictional factor	(1/m ² -s)
$f(Re)$	friction coefficient	(unitless)
g	gravity	(m/s ²)
H_{cap}	capillary rise height	(m or mm)
h_{fg}	latent heat of vaporization	(J/kg)
h	convection heat transfer coefficient	(W/m ² -K)
k	thermal conductivity	(W/m-K)
L	length	(m or mm)
N_g	number of grooves	(unitless)
P	wetted perimeter	(m or mm)
p_{cap}	capillary pressure	(Pa)
Q_{cap}	capillary heat transfer limitation	(W)
Re	Reynolds number	(unitless)
R_T	thermal resistance	(°C/W)
T	temperature	(°C or K)
t	thermal path length	(m or mm)
t_v	vapor space height	(m or mm)
w_g	capillary wick groove width	(m or mm)
x	axial location along heat pipe	(m or mm)

Greek Symbols

α	wetting angle	(degrees)
ω	elemental or total uncertainty	
ρ	density	(kg/m ³)
σ	surface tension	(N/m)
θ	angular orientation	(degrees)
μ	viscosity	(kg/m-s)

Subscripts

eff	effective
g	groove
h	hydraulic
l	liquid
max	maximum
rss	root sum of the squares
tot	total
v	vapor

LIST OF ACRONYMS

H1	Denotes heater 1 is active.
H2	Denotes heater 2 is active.
H3	Denotes heater 3 is active.
H12	Denotes heaters 1 and 2 are active.
H123	Denotes heaters 1, 2, and 3 are active.
H1234	Denotes heaters 1, 2, 3, and 4 are active.
HTCC	High Temperature Cofired Ceramic
I/O	Input / Output
LTCC	Low Temperature Cofired Ceramic
MCM	Multi-Chip Module
MCIC	Multilayer Ceramic Integrated Circuit
NEMI	National Electronics Manufacturers Initiative
RAM	Random Access Memory
SIA	Semiconductor Industry Association

I. Introduction

Background

Ceramic technology has a well established history in microelectronics, being initially used as a substrate for thick film hybrid circuits, and with subsequent development providing multilayer electrical interconnection within the substrate. Ceramic technology began to see popular use in the late 1970's as a method for fabricating mid- to high-reliability electronic substrates with multiple interconnection layers. Hence, the technology is typically used in military, space, and biomedical applications. Cofired ceramic provides a hermetic structure after firing, with a coefficient of thermal expansion close to that of silicon. Current packaging trends using ceramic cofire technology demonstrate the concept of "the substrate becoming the complete electronic package."

Alumina (Al_2O_3) provided the substrate material for both ceramic substrates and high temperature cofired ceramic (HTCC) technology, and it eventually led to the first low temperature cofired ceramic (LTCC) materials. Cofired ceramic materials are divided into two groups. The older group is the HTCC materials such as Al_2O_3 (aluminum oxide or alumina), BeO (beryllium oxide or beryllia), and AlN (aluminum nitride). Alumina is the most popular of the HTCC materials, of the three mentioned, mainly because it is the lowest in cost and it is the easiest to manufacture. Subsequent development

of alumina led to the LTCC materials which started as essentially alumina with a higher glass content, but has recently expanded into several other formulations.

Ceramic technology has been the leading technology in packaging where thermal management has been an issue, due to its thermal conductivity being greater than that of organic laminate technology (i.e. FR-4, printed circuit card). Organic laminate materials have a thermal conductivity around 0.1 W/m-K, as compared to about 30 W/m-K for alumina, 150 to 200 W/m-K for aluminum nitride, and about 380 W/m-K for beryllium oxide. It should be noted that the LTCC materials have the lowest thermal conductivity in the range of 3-4 W/m-K and, although being better than the organic laminates for heat transfer, is not thought of as a suitable alternative when thermal management is an issue.

In the past two decades, two packaging forms have taken an important focus in the ceramic packaging industry. The older of the two is called Multi-Chip Module (MCM) technology and the more recent is Multilayer Ceramic Integrated Circuit (MCIC) technology. MCM is based strongly on HTCC technology and was developed to meet the needs of high performance digital electronic interconnect semiconductor packages; it has actually been around since the 1970s, although industry use of the term MCM came later in the 1980s [Wilcox, 1971]. An MCM is an electronic package which contains several large Input/Output (I/O) semiconductor devices, and some passive

components. MCM technology is typically used for high speed circuitry, such as those found in telecommunications, avionics, and guidance systems. The high packaging density of these semiconductors produces high dissipated heat fluxes into the substrate material and thus, the thermal management of the MCM becomes a design issue. Many times these systems are racked mounted or stacked in such a manner that edge cooling is the primary heat removal technique.

The newer technology, MCIC, came out of the explosive growth of the hand-held wireless market. These applications required circuitry and packaging suitable for high frequency applications and the integration of passive components [Wilcox, 1997]. In MCIC applications, the material of choice has been the LTCC materials over that of the HTCC materials, mainly due to easier fabrication, lower cost, and the ability to manipulate the material to provide desired dielectric constants for high frequency circuits. With the development of MCIC technology, the embedding of hundreds of passive components is feasible, further extending the concept of the substrate becoming the complete electronic package.

Following the history of cofired ceramic technology, it can be seen that it started as a substrate technology, and evolved into a multilayer interconnect structure with enhanced (passive) thermal management capability. More recently, it has evolved also containing embedded passive components. This evolution has not ceased, with the underlying concept of

MCIC technology driving research in the development of meso-scale electromechanical systems embedded in the multilayer structure, including bridge structures and membranes [Espinoza-Vallejos, et al., 1997], piezoelectric transducers [Lynch et al., 1998], and single phase liquid cooling channels [Thelemann, et al., 1999].

The concept of embedding a heat pipe into the ceramic substrate becomes a natural extension of current trends in electronic packaging. Review of the National Electronic Manufacturers Initiative (NEMI) technology roadmap in 1995, indicates that "significant improvement in thermal management is required to support power requirements within target cost" and that "power dissipation will limit chip size for hand-held applications." Additionally, the roadmap calls for the "integration of design, chip fabrication, assembly and packaging, and test technologies will be critical to support requirements in 2001 and beyond" [NEMI, 1995]. The technology roadmap shows that for high performance systems, semiconductor chips will have dissipated powers reaching 140 W per die with a heat flux of about 16 W/cm² and operating at speeds over 1200 MHz. Another technology roadmap by the Semiconductor Industry Association (SIA) predicts that for computer processors, dissipated power will be 200 W per die by 2004 [SIA, 1995]. Both roadmaps indicate that package size will continue to shrink, typically indicating more electronics with a higher system dissipated heat.

Embedding heat pipes into the ceramic substrate will provide a thermal transport mechanism capable of transporting heat over the length of the substrate at an effective thermal conductivity at least ten times higher than typical metals and over 100 times that of the substrate material. If the substrate is bonded to a heat sink material, then the heat pipe serves to spread the heat over a larger area, utilizing more of the heat sink. The result being a smaller temperature rise across the substrate from the heat sink to the heat dissipating parts. However, a most powerful use of the heat pipe is in applications where cooling can only be provided along an edge of the substrate. In this situation, the thickness of the substrate is very small when compared to its length or width. Hence, the combination of a small cross-sectional area available for conduction heat transfer through the substrate material and a low thermal conductivity material leads to a thermal resistance which is too high for adequate cooling of the electronics.

Objectives of the Research

The overall objective of the proposed research is to fabricate prototype miniature heat pipes using cofired ceramic technology, thereby allowing the heat pipe to be fabricated as part of the ceramic substrate. The prototype heat pipes are meant to provide validation of this concept. The use of cofired ceramic technology makes the heat pipe compatible with the manufacturing processes and eliminates compatibility issues which would arise if a

conventional metal heat pipe were inserted into or bonded to the surface of a ceramic substrate.

Specific objectives of the proposed research are as follows:

(1) Identify key parameters for optimized heat pipe design. Determine design parameter values and ranges for optimum heat pipe design which are compatible with current thermal management and typical packaging requirements.

(2) Development of heat pipe designs and manufacturing processes, which can be readily adapted to current electronics manufacturing technology. Hence, ease of manufacture and low cost are important parameters which will enter into the proposed pipe design and fabrication techniques.

(3) Perform modeling of the substrate with an embedded heat pipe using finite element analysis. The purpose of this modeling is to assess the thermal resistance from the surface of the substrate to the vapor space of the heat pipe, i.e. the conduction heat transfer through the shell material of the heat pipe.

(4) Perform an experimental evaluation of the operation of the prototype heat pipes to characterize their thermal performance under various thermal loads, single and multiple heat sources, various axial orientations with respect to gravity etc.

Significance of the Research

The proposed research is unique in that heat pipe operation has been demonstrated using ceramic materials, embedded in electronic substrates, and fabricated as an integral part of the substrate's structure, and, to the knowledge of the candidate and his committee, the work performed to date has been the first of its kind. Furthermore, the heat pipes are unique in that they are constructed in materials that has a very low thermal conductivity with a relatively high specific heat, whereas, all heat pipes presented by other researchers are made using typical structural metals which have a high thermal conductivity with a low specific heat. A consequence of this materials selection is that the thermal response of the ceramic heat pipes may not be similar to that seen previously for heat pipes constructed using conventional materials. The successful development of embedded heat pipes in electronic substrates will provide a major advance in the thermal management of electronic packages.

II. Literature Review

There is a large quantity of published work, starting in the late 1960s, related to experimental, numerical, and analytical work involving heat pipes. However, much of the early work is published in corporate technical reports describing the performance of prototype heat pipe systems for aerospace applications rather than more scientifically oriented work published in peer-reviewed journals. These early systems were generally macro-scale heat pipes with lengths near one meter. The exponential growth in electronics technology since the 1970s has led to higher component density, greater miniaturization, and greater power handling capability, which in turn, has made thermal management of microelectronic systems increasingly important. Hence, an interest in using miniature and micro-scale heat pipes for electronic cooling applications emerged. The heat pipe technology presented in this dissertation is in direct response to the need for advanced thermal management in advanced ceramic microelectronic packaging applications. Hence, its form and function falls in the scale of miniature and micro-scale heat pipe technologies.

To provide a historical background for the work discussed in this dissertation, a review of the relevant literature related to experimental work in small scale heat pipes will be presented. Although a significant body of work exists in the heat pipe community, a review of the literature will show that no work exists for heat pipes made out of a ceramic material, or

fabricated as an integral part of a laminated structure. Furthermore, it will be shown that the body of experimental data available for miniature heat pipes utilizing axially grooved wick structures is also limited.

It is generally accepted that miniature and micro-scale heat pipe theory began with Cotter (1984), and from this work, the working definition of a micro-scale heat pipe was introduced. In general, micro-scale heat pipes are defined as a heat pipe in which the mean curvature of the vapor-liquid interface is comparable in magnitude to the reciprocal of the hydraulic radius of the total flow channel. Typically, micro-scale heat pipes don't have a wick structure, but rely on the cusp-like corners of the channel to provide a location for a meniscus to form. Early research for micro-scale heat pipes continued with work by Babin et al. (1989), Wu and Peterson (1991), Gerner et al. (1992), and Longtin et al. (1994). These researchers fabricated and tested heat pipes with copper, aluminum, and silver shell materials, with water as a working fluid. The heat pipes had lengths from 25 to 120 mm, and cross-sectional areas of under 2 mm^2 . The total heat transport capacity of micro-scale pipes is typically near one Watt. Throughout the decade, micro-scale heat pipe research, both experimental and theoretical, has been continued by G.P. Peterson and his colleagues: Ma and Peterson (1996), Ha and Peterson (1998). However, in all these cases, the heat pipes have been fabricated with metal shells, minimal or no formal wick structure, and have

had power transport capacities near one Watt. Most of the work presented has been theoretical and experimental work is very limited.

Except for the working fluid selection and the operational temperature range of these heat pipes, the work presented to date for micro-scale heat pipes is not very comparable to the form and function of the embedded heat pipe presented in this dissertation. The micro-scale heat pipes presented by other researchers have fairly inefficient capillary wick systems which can not provide the necessary capillary pumping of the working fluid for high power transport levels and/or long effective heat pipe lengths. It should also be noted that the micro-scale heat pipes presented by the researchers mentioned are at the top end of the micro-scale, since the same heat pipe design has been demonstrated at much smaller sizes in silicon wafer technology [Peterson, 1993]. The works cited have been included because the heat pipe technology presented in this dissertation can be scaled down slightly to be considered at the top end of the micro-scale (i.e. lengths of one inch and cross-sectional areas of 1 mm^2), however, heat pipes at scales smaller than this would not be very effective using the cofired ceramic technology.

Miniature scale heat pipes with axially grooved wicks were available in the 1980s as commercial prototypes and/or products. However, published work in this period is non-existent until the 1990s. The continued exponential growth rate of microprocessor speeds with increased chip sizes has exacerbated the need for more aggressive research in electronic cooling.

In response, researchers in the last decade have begun to address miniature heat pipes in both experimental and analytical work.

Plesch et al. (1991) tested two miniature heat pipes with axially grooved wick structures. The dimensions of both heat pipes were 7 x 2 x 120 mm. In one case, the grooves were oriented in the transverse direction, and in the other case, the grooves were oriented in the longitudinal direction. The heat pipe was made of metal with water as a working fluid. The design with the longitudinally oriented wick had a heat transport capacity of 70 W with a temperature drop over the heat pipe of 35 °C. Following this work, interest in the operation of miniature heat pipes with a formal wick structure increased. Immediately, a variety of researchers investigated the fundamental operation of the miniature heat pipe and established some of the primary phenomenological differences between miniature heat pipes and the conventional heat pipes commonly in industrial applications. These researchers included Kojima et al. (1992), Lee et al. (1992), Chen et al. (1992), Zhou et al. (1992), and Li et al. (1992).

Lee et al. (1992) and Chen et al. (1992) focused on visualization experiments to document the two phase flow patterns found in thermosyphons. Zhou et al. (1992) performed experiments on a copper heat pipe using acetone as a working fluid. These researchers found the maximum operating limit of the heat pipe was the capillary limit, which was independent on the cooling air temperature. This work helped to introduce

the importance of optimal design for miniature heat pipes and the importance of the capillary limit which is mainly a geometry based limit. Lee et al. (1992) investigated the effect that the amount of the working fluid has on the performance of the heat pipe. These researchers provided data to support the observation that the effect of the working fluid volume is greater for miniature heat pipes than for conventional heat pipes, and that the influence of entrainment on the capillary limit was greater for a smaller diameter heat pipe than for a larger diameter heat pipe.

With the increased interest in miniature heat pipes, researchers began to focus on analytical and numerical modeling of the various processes occurring within the heat pipe. The operating limitations of miniature heat pipes was reviewed and summarized by Cao et al. (1993). However, experimental data to validate the analytical operating limitations were not presented at this time. Soon after, these same researchers fabricated miniature heat pipes with axially grooved wicks to obtain experimental results.

Cao et al. (1997) tested two copper-water miniature heat pipes with an axially grooved wick structure fabricated by an electric discharge machining process (EDM). The smaller pipe had outer dimensions of 80 x 7 x 2 mm and the larger pipe had outer dimensions of 82 x 7 x 2.8 mm. Both pipes had a vapor space width of 5 mm, with vapor space heights of 0.8 and 1.0 mm. The grooves in the smaller pipe were 0.1 mm wide with a depth of 0.25 mm on a

0.2 mm spacing. The grooves in the larger pipe were slightly wider (0.12 mm) and also had a slightly wider spacing (0.24 mm). Heat was applied to the heat pipes at one end by a resistive heating element formed by wrapping stainless steel wire tightly around the outer shell. The other end of the pipe was inserted and sealed into a cooling jacket through which coolant flowed in direct contact with the outer shell of the heat pipe. Data were presented for the two heat pipes showing the outer shell temperature along the length of the pipe at a few coolant temperatures and thermal loads. Testing was performed to estimate the capillary limit for each of the pipes in the horizontal and vertical orientations. Additionally, the researchers presented the ratio of the effective thermal conductivity of the heat pipe and that of copper for each experimental configuration. Also presented was the capillary limit analysis, which compared the theoretical capillary limit with the experimental values. It was found that the maximum heat input was 31 W with a heat flux of 20.6 W/cm². The researchers also showed that the analytical results for the capillary limit were in good agreement (within 10%) with experimental values for one of the heat pipes. However, the analytical and experimental values differed largely for the second pipe due to some uncertainty in the actual dimensions of the wick structure. In this case, the experimental capillary limit was as much as one-half of the predicted values.

The work of Cao et al. (1997) was extended in Gao et al. (1999), where the data from the two heat pipes was augmented by experimental data for a

third heat pipe. In Gao et al. (1999), the researchers applied numerical optimization techniques to design the third heat pipe. The third heat pipe was identical in materials and manufacture to the first two pipes [Cao et al. (1997)], except that the length was slightly longer and the axially grooved wick dimensions were optimized numerically. The third heat pipe had outer dimensions of 120 x 7 x 3 mm. The axial grooves in the wick had a depth, width, and spacing of 0.30, 0.13, and 0.21 mm, respectively.

Using the same experimental set up and procedure as in Cao et al. (1997), Gao et al. (1999) found that the optimized heat pipe had a maximum capillary limit of 50 and 70 Watts, in the horizontal and vertical orientations, respectively. Comparing the optimized heat pipe to the two earlier heat pipes showed about a 66% increase in performance. However, the researchers did report that there was an approximately 20% difference between the analytically predicted capillary limit and the empirical value, and that the deviation increased with increased operating temperature of the heat pipe. Additionally, the researchers showed that the capillary limit analysis is well suited for numerical optimization, thus providing a stable optimized solution method. However, the value of such optimization is overshadowed by the relatively large deviations between the analytical prediction of the capillary limit and the empirical values, a phenomena not exclusive to just these researchers. Furthermore, the variability in the thermal performance of miniature heat pipes due to variations in the volume of the working fluid are

not well understood nor addressed by any researchers. Hence, even non-optimized designs can outperform optimized designs in some cases.

Hopkins et al. (1999) performed an experimental investigation of three miniature copper-water heat pipes with axially grooved wick structures. The heat pipes were from 100 to 120 mm in length. The smaller heat pipe had a height and width of 7.01 and 2.01 mm, respectively. The larger heat pipe was 13.4 x 8.92 mm. The axial grooves ranged in size from 0.2 mm (width) by 0.42 mm (height) for a rectangular shaped groove to a slightly larger trapezoidal design with dimensions of 0.45 mm (width) by 0.20 mm (height). The performance of these heat pipes was determined for various operating vapor temperatures from 60 to 95 °C. It was found that the orientation of the heat pipes had a significant effect on the total amount of heat that could be transported. The researchers found that the majority of the experimental data show that the primary controlling mechanism on the maximum heat load was the capillary limit. However, especially in the vertical orientation, the pooling of excess working fluid in the evaporator region caused the maximum heat load to be restricted by the boiling limit. It was surmised that the pooling of the excess fluid may have increased the thermal resistance of the heat pipe at lower heat loads.

The data collected by Hopkins et al. (1999) also shows that axially grooved wicks with deeper, more narrow grooves have better performance. Additionally, heat pipes with thicker shell material also have better

performance. Critically speaking, these conclusions are not too enlightening since the results are expected from the analytical models. In any case, the experimental data does permit some validation of the foundation theory of the analytical models, making them more credible for use in the optimum design of miniature axially grooved heat pipes. What is more significant in the data presented by Hopkins et al. (1999) is that in all cases, the experimental performance of the three heat pipes met or exceeded the capillary limits predicted by the popularly accepted analytical models (which is presented and discussed in this dissertation). This result is in contrast to other research which typically shows the opposite trend.

What is important to note about the work presented by both Cao et al. (1997) and Hopkins et al. (1999), is that the thermal load was applied to the heat pipe around the full circumference of the outer shell. This provides for a well distributed thermal load over all of the capillary wick structure. In contrast, the heat pipes presented in this dissertation are heated by very localized heating elements which better represent electronic components. Additionally, this form of heating is more known as spot heating or block heating and has associated with it some additional problems caused by very large heat fluxes which may not transfer effectively to the entire capillary wick structure.

All of the work presented thus far for miniature heat pipes has not investigated the effect of multiple heaters. Upon initial inspection, one may

conclude that for very small scales, the heat from multiple heaters would conduct through the shell material and blend, essentially making a single larger heating zone. However, the ceramic material used in the present research has a thermal conductivity an order of magnitude lower than conventional metal heat pipes. Hence, it can not be assumed that large local temperature variations don't exist just because the scale of the heat pipe is small.

Lastly, in all of the work cited, the heat pipes were cooled by having the entire circumference of the outer shell cooled in the condenser region. In reality, this method of cooling may be appropriate for research on heat pipe operation, but it is not very representative of how actual electronic systems are mounted and cooled. The use of edge cooling rails is common in electronic packages, whereby the substrate material is bonded on one side to a metal frame which provides cooling by conduction. This method of attachment will have serious consequences on the performance of the condenser due to a reduction in area which has effective cooling. More realistic configurations can actually have the thermal load on one side of the substrate with the cooling rail attachment on the other side of the substrate. Hence, the path the working fluid must take from the evaporator to the condenser is different than that in a more conventional heat pipe arrangement. The experimental set-up used for the work discussed in this dissertation attempts to address

this by providing cooling on one side of the substrate by attachment to a temperature controlled cold plate.

III. Cofired Ceramic Embedded Heat Pipes

In this section, the design and manufacture of the heat pipes developed in this study will be discussed. For the benefit of the reader, the discussion will include background information relating to the ceramic materials used in cofire ceramic electronic packages and the cofire ceramic manufacturing process. The inclusion of this background material should assist the reader unfamiliar with this technology in understanding why certain approaches were taken in the design of the heat pipes. The successful development of embedded heat pipes in cofire ceramic technology requires an understanding of the materials and the processing that is inherent in the technology.

Cofired Ceramic Substrate Manufacturing

Cofired ceramic substrates are created by the lamination of several layers of unfired ceramic materials into a single structure which is then fired at high temperature to produce a monolithic structure. Each layer of unfired “green” tape can be processed to provide an electrical interconnect layer in the final substrate structure. Electrical conductors are patterned on each layer using thick film processing. Electrical interconnection between layers is accomplished by vias which are formed by punching holes in the tape layer, which are then filled with conductive thick film ink. In this manner, a high interconnect density can be achieved, allowing for high miniaturization of the electronic package.

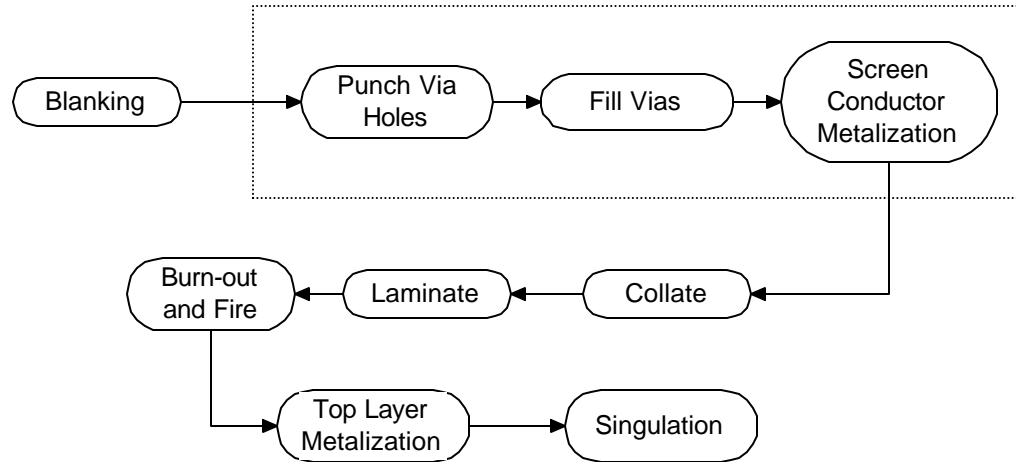


Figure 3-1. Typical cofired ceramic process for multilayer fabrication.

The fabrication process of a multilayer cofired ceramic substrate is shown in Figure 3-1. As the initial tape cast ceramic can have widths up to three feet, the tape is blanked into a working sheet which has registration holes punched into the tape to allow for spatial orientation to be maintained throughout the fabrication process. Some manufacturers prefer to mount the tape onto a carrier frame which has various registration holes and slots punched into it. After blanking the working sheet, via holes are punched into the tape. Vias are typically made by numerically controlled mechanical punching, although laser and mechanical drilling is also used. Vias are then filled with a metalization using a vacuum assisted screen printing process. The screen printing process can use either metal stencils, aligned over the via holes or by a plastic mask which is bonded to the tape prior to punching, and punched simultaneously with the tape. Following the via formation and filling, interconnect metalization is screen printed onto the tape and allowed

to dry. Each layer of tape in the substrate can be processed sequentially or in parallel until all the necessary layers of interconnection are obtained. With all of the tape layers punched, filled and patterned, the multiple layers of tape are then stacked and laminated under heat and pressure to mechanically adhere the layers together. The advantage of the parallel fabrication of the tape layers is that it reduces time. Another advantage of multilayer processing is that each tape layer can be inspected prior to collating the layers together. Following the lamination process, the tape is still in the "green" state. The process continues with the laminated stack being fired at high temperature with a specified temperature profile creating a monolithic ceramic structure. The fired ceramic may be ground or polished for flatness, and then, additional metalizations may be applied to the top and bottom surfaces of the fired ceramic. To further increase productivity, multiple units are typically fabricated together on the same blanked piece of tape, also known as a "ganged" piece. After the final metalizations are applied, and sometimes after electrical testing, a process called "singulation" is performed, in which the individual units may be cut apart from the ganged piece. Furthermore, additional ceramic is usually required around the actual unit for handling and registration purposes. During the singulation process, the excess material is trimmed away.

Lamination and Firing Processes

The lamination process used to bond the individual tape layers together serves a few purposes. The first effect of laminating the green tape is to bond the individual tape layers together tightly prior to firing. This is important if geometric registration is to be maintained between the tape layers. The lamination also causes a high densification of the material, required for effective sintering to occur between the ceramic particles in the tape. Without densification of the ceramic, the fired structure may be porous, making the ceramic non-hermetic, and hence, capable of allowing water, sodium and other contaminants harmful to the electronics to migrate into and through the ceramic substrate or package. Finally, lamination, causes the ceramic material of each tape layer to intimately contact the material in the other layers. Again, this is required for proper sintering and for avoiding the layers from separating from each other during the firing cycle.

The lamination process for cofired ceramic tape is specified by the manufacturer of the material. However, the lamination process is fairly universal among the various manufacturers. Lamination is recommended to be performed at 3000 psi and at 70-80 °C for a period of about ten minutes. As simple as that appears, sometimes this process is modified to accommodate specialized structural needs. For example, very thick stacks with many layers of tape may be warmed up to temperature prior to the application of pressure. The reason being that the very low thermal conductivity of the material prevents the entire stack from being at the

desired temperature when the pressure is applied. This can have critical implications as the binder and solvents in the tape react at specific temperatures. Lamination at too low a temperature usually results in poor adhesion of the layers since the binder material isn't activated and flowing. Lamination at too high a temperature usually results in excessive in-plane (x-y) tape deformation due to increased viscoplastic response. Additionally, at higher temperatures, the solvents in the tape may become activated and the tape can dry-out.

In the construction of heat pipes and other cavity structures in cofired ceramic tape, lamination becomes much more complex due to the sagging of the tape layers above and below the heat pipe or cavity. Excessive sagging results in a loss of flatness in the top and bottom layers of the tape, which causes problems for device attachment and top surface metalizations. Furthermore, excessive sagging can also lead to the tape cracking during firing which results in a non-hermetic structure (hence, a "leaky" heat pipe).

The solution to the problem of tape sag is not plainly evident and not clearly understood in industry. In this study, part of the fabrication process included the investigation of the sagging problem and the techniques needed to overcome it. However, in reality, there is no all purpose solution, but rather, solutions have to be found on a continuing basis as new materials become available and different heat pipe designs are attempted. In many ways, the fabrication process is more art than science.

When green ceramic tape is laminated, the entire tape stack has a uniform compressive stress in the z-axis (vertical, normal to applied load). The tape material undergoes viscoplastic deformation giving z-axis shrinkage (densification) with the density of the tape material rapidly increasing. In addition, there is a small expansion of the material in the x-y plane, hence indicating a tensile stress state in the x-y axes. In any case, the compressive stresses in the z-axis and the tensile stresses in the x-y plane are relatively uniform throughout the tape stack, resulting in a flat, highly compacted monolithic structure.

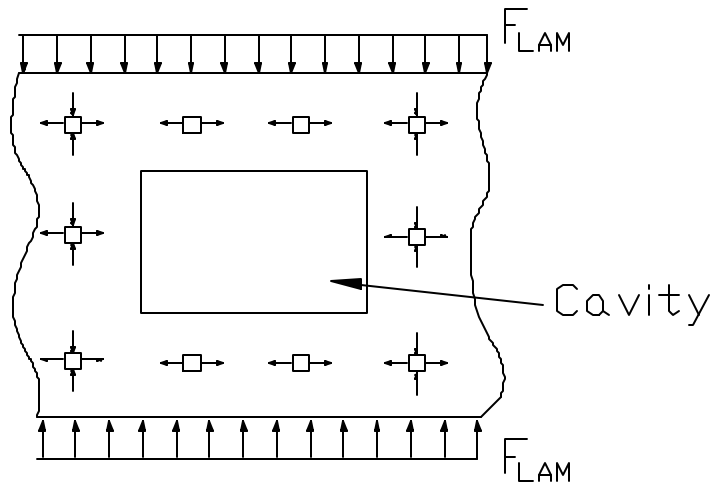


Figure 3-2. Lamination stresses in green tape when a cavity exists in the tape stack.

When a cavity exists in the tape stack, the stress distributions in the material are not uniform, especially in the regions of an interior cavity [Bauer et. al, 1997]. This can lead to sag in the tape on the top and bottom of the cavity, an inward bowing of the side walls of the cavity, and non-uniform expansion of the tape stack in the x-y plane. As shown in Figure 3-2, the

material on the top and bottom layers of the cavity are unsupported, hence, there is no resisting force inside the cavity to cause a compressive stress state in the z-axis. Consequently, the unsupported regions of material have little or no reason to expand in the x-y direction. As the remaining material undergoes x-y expansion due to the compressive load, excess material will flow toward the unsupported regions on the top and bottom of the cavity. This flow of material causes the unsupported regions to gain material without any densification, and hence, the material deforms causing the unsupported material to sag into the cavity.

To overcome excessive sagging in the tape above and below a cavity or heat pipe, modifications to the conventional lamination process was investigated. Several techniques for cavity fabrication in cofired ceramic structures have been proposed by others [Bauer et al., 1997]. These methods include using dummy inserts to fill the cavities during the lamination process so that all of the tape material is compressed uniformly. The inserts are removed prior to firing the ceramic. In fact, the use of inserts is typical for large open faced cavity structures where the ceramic is fired with the cavity exposed, and sealed after the firing process by means of a metal cover plate. This method was not suitable for heat pipe applications as the heat pipe is fully enclosed within the substrate and hence there would be no way to remove the insert prior to firing.

In the fabrication of the prototype heat pipes in this study, it was found that sagging could be minimized by laminating parts of the total tape stack individually (for densification) and then laminating the parts together as a final group (tacking for adhesion). The tape stack should be broken into three groups, the top and bottom layers and the cavity layers. The top and bottom layers are the layers above and below the cavity. By laminating these layers individually, the problem with having some of the tape being unsupported and not achieving an increased density is removed. The inner (cavity) layers can also be laminated separately, to form a single piece. Finally, the top, cavity, and bottom pieces can be laminated again to tack and adhere the pieces together for the firing process. If necessary, the fired structure can be polished to increase the flatness of the final top and bottom surfaces. It has also been found additional sacrificial layers can be added to the top and bottom sides of the tape stack. The additional layers of tape provide increased strength and resistance to sag in the top and bottom layers. After firing, the fired piece is polished, hence, grinding off the additional layers of tape to achieve the desired thickness of the final product. The addition of sacrificial layers is not uncommon in industrial applications because increased flatness and surface quality is achieved in the final product while making the fabrication process more forgiving.

The firing process is a key step in the manufacture of ceramics and converts the flexible green tape material to a true ceramic. The firing process

uses a temperature profile with specified ramp rates and usually two temperature dwells. The first temperature dwell is near 450 °C for two to four hours, and is used to burn-out the organic binders, plasticizers and solvents from the material. It is necessarily a slow process, since the removal of the organic materials involves thermal decomposition and evaporation followed by mass transfer of the materials out of the ceramic matrix. Performing this process too fast can lead to gas bubble formation inside the laminated stack, causing deformation and delamination of the tape layers. If the pre-fire stage is not performed long enough, there may be insufficient time for adequate burn-out of the organic materials which may then become trapped in the fired ceramic.

The second temperature dwell in the profile is the sintering stage of the firing process, which involves bringing the material up to 1650 °C in a reducing atmosphere for 10-15 minutes. Sintering causes the remaining particles to shrink and compact and recrystallization of the particles to occur promoting grain growth. Large grains primarily govern the shrinkage of the material during sintering. Small grains promote higher density of the material and increased strength through less porosity. Shrinkage can be considerable during shrinkage, with up to 50% reduction in volume with 12 to 25% shrinkage in planar dimensions. This dimensional change is significant and must be accounted for in the design of the interconnection, holes, and cavities.

Because of the shrinkage of ceramic, typical substrates have areas of under 16 in² with thickness' typically under 0.100 inches. Large area cofire substrates are more difficult to fabricate with high yield due to non-uniform shrinkage in all directions, causing lack of geometric registration of the top and bottom layer component pads, and z-axis via connections.

Ceramic Substrate Materials

Ceramic substrates are primarily composed of metal oxides mixed with glasses, and are fired at elevated temperatures. The resulting material is hard and brittle and offers many advantages over conventional printed circuit board materials for hybrid microelectronic applications. As compared to organic substrates (e.g. printed circuit board), ceramic substrates have a higher thermal conductivity and an expansion coefficient closer to that of silicon. Additionally, the ceramic materials have a much higher tolerance to temperature extremes, a higher mechanical strength, better electrical properties, and they are non-hydroscopic and hermetic. Ceramics, once fired are essentially chemically inert. Finally, ceramic substrates allow for much greater miniaturization of interconnection due to superior surface characteristics over that of the organic substrates.

The ceramic materials of interest in the current study are those well suited to the cofired ceramic process. Cofired ceramic substrate material is formed by a tape casting process. The ceramic oxide materials are mixed with plasticizers, binders, solvents, and other additives to form a slurry. A

thin sheet of the slurry is pumped under a knife-edge to form sheet of uniform thickness, which is typically cast on a carrier film. The carrier films are usually a Mylar or cellulose acetate film. The resulting tape of unfired ceramic is commonly called “green tape.” Typical ceramic green tape comes in roll form with thickness’ ranging from 0.002 to 0.020 inches, and widths up to three feet. The high temperature cofired ceramics (HTCC) have compositions of the metal oxide above 90%. The result is firing temperatures near 1600 °C, which requires specialized furnaces which increases the cost of manufacture. The properties of the HTCC alumina used in this study are summarized in Table 3-1.

Property	Value
Density (g/cm ³)	3.8
Thermal Conductivity (W/m-K)	20-24
Specific Heat (W-s/g-K)	0.8-1.1
TCE (ppm/°C)	7.3
Elastic Modulus (x10 ⁶ psi)	33-52
Compressive Strength (ksi)	290-380
Bending Strength (ksi)	43

Table 3-1. Physical properties for HTCC alumina [Sergent, 1995]

Wetting Angle of Cofired Ceramic Materials

Heat pipes use a capillary wick structure to transport the working fluid within the device. The capillary pumping action of the wick structure is significantly affected by the ability of the working fluid to wet the surface of the wick. The capillary pressure developed by a wick structure is given by

$$p_{cap} = \frac{2s \cos \alpha}{w_g} \quad (3.1)$$

From the equation, it can be seen that the capillary pressure is a function of the surface tension of the working fluid, the wetting angle of working fluid on the wick material, and a geometric length scale, which for axially grooved wicks is given by the width of the groove. It is also apparent from Equation 3.1, that increasing the surface tension, decreasing the wetting angle, or decreasing the groove width will increase the capillary pressure, and hence, the capillary pumping action of the wick.

The choice of the working fluid for a heat pipe is determined by the operating temperature range of the heat pipe and its compatibility with the materials used in fabricating the heat pipe. For the cooling of electronics on ceramic substrates, the operating temperature range limits the choice of the working fluid to acetone, methanol, ethanol, and water [Faghri, 1995]. The alcohol based choices have the advantage of good wetting and low viscosity and relatively high surface tensions, however, their specific heat and latent heat are about one-fourth that of water. Hence, the heat carrying capacity of these liquids is limited as compared to water. Additionally, these liquids are flammable, have harmful vapors, and have flash points below 120 °C, increasing the handling and safety issues for manufacturers. Water, is cost-effective and manufacturing friendly, and of most common engineering liquids, has superior heat transport capability. For these reasons, water is used almost exclusively in low-temperature heat pipes (i.e. operating

temperatures from 40 to 100 °C). The only disadvantage of water is that its wetting on various surfaces can range from poor to moderate.

For optimum design of the ceramic heat pipes, it is important to quantify the wetting of the working fluid on the materials used to fabricate the heat pipe. For the ceramic materials of interest, wetting data is extremely scarce and none could be found in the literature or from the material suppliers, and it was suspected that the wetting angle of water on the ceramic material was not small (i.e. $> 10^\circ$). Hence, a quantitative measurement was sought for determining the wetting angle. Two methods were chosen, the tilted plate method and the sessile drop method because they were relatively easy to employ and are better known among all the methods. However, it should be recognized that there is considerable argument as to the extensibility of the data from the test fixture to the actual application, as well as, the accuracy of the various methods for testing the wetting angle. So a capillary rise test should also be performed on an actual wick structure to compare to the results found by the wetting angle tests.

For the sessile drop method, a Tantec Wetting Angle Meter (Model CAM-Micro) was used. The device uses a projection method to project the shadow of the sessile drop on the sample onto a calibrated grid/protractor. A micrometer driven plunger creates a drop of liquid on the tip of a blunt end syringe, which is measured visually on the projection grid for a specified diameter. Then the material is raised to contact the drop which detaches

from the syringe tip and on to the test sample. Assuming the drop is spherical and uniform, a drop of known volume can be dispensed repeatedly. The degree of wetting causes the drop to spread across the material.

It is very difficult to visual and accurately measure the actual angle at the intersection of the drop's free surface and solid material, mainly because if the high magnification that would be required and the difficulty in accurately determining the tangent to an ever curving surface. Hence, the wetting angle meter is set up so that the user measures the angle from the contact point at the drop's edge to the drop's apex point (the point of maximum height of the drop). Analytically, the angle at the intersection of the drop's free surface and the material can be related to the angle between this intersection and the apex of the drop's curved surface which is at the center of the drop. Since, the device projects the image of the drop and magnified it substantially, the user to perform the measurements visually on the calibrated grid/protractor without the aid of optics. By adjusting a compass line on the protractor from the drop's contact point to the apex point, the wetting angle can be read directly from an angular scale which has been calibrated based on the known volume of the drop dispensed by the syringe.

To reduce experimental error using the wetting angle meter, multiple measurements were taken at different spots on the test sample. The measured data was statistically analyzed to determine a wetting angle. Aside from the experimental variations in the measurements, it was observed

that even with careful use of the wetting angle meter, that an (elemental) experimental error of $\pm 1^\circ$ was typical in determining the apex point on the drop's projected image. A source of error could also be found in determining the size of the drop prior to wetting the test surface. However, using care during the procedure, it was observed these small variations in drop size appeared to have a very small effect on the measured wetting angle when compared to the statistical variation in the measurements. Furthermore, surface preparation is crucial in wetting angle measurements. For the ceramic materials, the samples were cleaned using methanol and then dried in an oven at 450°C for one hour to burn off any organic residuals.

Seven LTCC materials were tested as well as HTCC 99% alumina. All of the samples were laminated and fired as per the manufacturer's specifications. At least twelve measurements were made on each sample at multiple locations on the sample so as to minimize the chance of a single surface aberration from skewing the results. The results for the LTCC materials is given in the Appendix of this report. For the HTCC alumina, the mean wetting angle was found to be 60.1° with a standard deviation of 2.7° for 20 samples. Applying two times the standard deviation as the 95% confidence and using a RSS (root sum of the squares) method for adding in the elemental instrument error of 1° , the uncertainty of the wetting angle could be is determined to be $\pm 6^\circ$. In summary, the sessile drop method

indicated a wetting angle of water on HTCC alumina to be $60^\circ \pm 6^\circ$ (with 95% confidence).

Referring to Equation 3.1, the effect of such a high wetting angle is the reduction by the capillary pressure by about 50% from the maximum attainable. As will be shown in a later section, the wetting angle has a significant result on estimating the capillary limit for the heat pipe. Many researchers do not include the wetting angle in the determining the capillary pressure developed by the wick structure, and hence, the estimate obtained is that for the maximum possible heat transport capability. This may not appear to be problematic, but in practical applications for conventional metal heat pipes this typically results in the estimate of the capillary limit being 10 to 30% too high. However, for ceramic materials such as HTCC alumina, the wetting angle is very large, which results in the estimated capillary limit be significantly (e.g. >50%) much higher than experimental results. It is for this reason that the wetting angle will be considered in the design of the embedded heat pipes.

General Heat Pipe Operation and Design

A heat pipe consists of a sealed, hermetic enclosure, with three distinct regions: an evaporator, a condenser, and an adiabatic region separating these two regions (Figure 3-3). The enclosure contains a working fluid, which absorbs heat by evaporation at the evaporator, travels as a vapor in the adiabatic region to the condenser, where the heat is removed. Due to the

evaporation process the local vapor pressure is increased at the evaporator section of the heat pipe. Likewise, the process of condensation causes a local decrease in the vapor pressure in the condenser section. The variation in local vapor pressures sets up a negative pressure gradient from the evaporator to the condenser within the heat pipe. This pressure gradient supplies the driving force to transport the vapor from the evaporator to the condenser without the need of a pump or other external driving force.

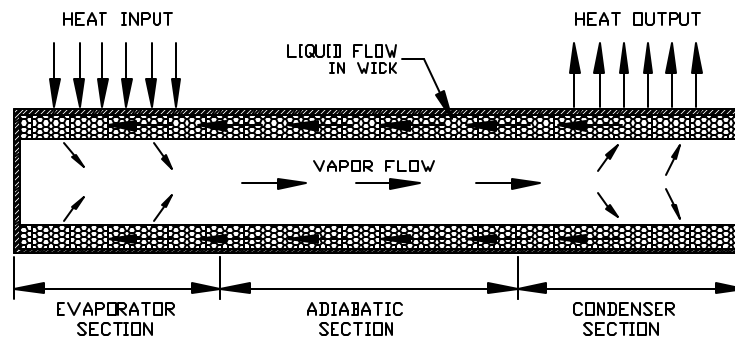


Figure 3-3. Schematic showing basic heat pipe operation.

The working fluid returns to the evaporator section from the condenser by the capillary action of a wick structure. Capillary wick structures typically used in heat pipes are sintered porous materials, fine wire screens and meshes, and axial grooves cut into the inside walls of the heat pipe's outer shell. Providing that the working fluid wets the wick material, capillary forces due to surface tension are generated in these wicks which transports the working fluid from the condenser where working fluid is being

added to the wick to the evaporator where the working fluid is being removed.

In the traditional application of a heat pipe, the primary transport of heat is along the axial direction of the heat pipe, essentially from one end to the other, which is shown schematically in Figure 3-3. This method of heat transport uses the heat pipe to move heat over relatively long linear distances with almost negligible temperature variation along the length of the heat pipe. Heat is added and removed from the ends of the pipe by conduction or convection at the outer shell of the heat pipe. The working fluid is circulates mainly along the axial direction of the heat pipe from one end to the other.

A successful heat pipe design requires a balance of several parameters, not only to get the heat pipe to function, but to attain an operating performance which will be equal or better than current heat pipe technology. As the size of the heat pipe decreases, the selection of the design parameters becomes increasingly critical, limiting the range of values that can be chosen for any given parameter. To further complicate the problem, the limitations of the manufacturing technology must be addressed, since an optimized design is only good if it can actually be fabricated.

The heat transfer limitations for miniature heat pipes have been found to be the capillary, boiling, entrainment, and sonic limitations. However, for miniature heat pipes, the capillary limitation becomes the most significant.

The formulations for the heat transfer limitations found in the current literature have been found to be in agreement with experimental results for heat pipes with geometry similar to the designs proposed in this investigation [Faghri, 1995].

Axially grooved wicks, which are commonly found in miniature heat pipes, can be manufactured in cofired ceramic technology by a relatively easy process using conventional manufacturing processes. Hence, axially grooved wick structures are the focus of this research. For miniature heat pipes employing axially grooved wick designs, the capillary limitation is given in Equation 3.2 [Faghri, 1995]. The equation relates the pumping action of the working fluid due to surface tension, σ , and the frictional forces, F_l and F_v , to flow of the working fluid from the condenser back to the evaporator. The frictional forces are described by two components, F_l , which represents the interaction of the working fluid and the wick material (structure), and F_v , which represents the resistance to the vapor flow due to the geometry of the vapor space.

$$Q_{CAP} = \frac{2s \cos a - rgL_{eff} \sin q}{w_g L_{eff} (F_l + F_v)} \quad (3.2)$$

The liquid and vapor frictional coefficients are given in Equations 3.3 and 3.4. Referring to Equation 3.3, it is seen that the vapor frictional coefficient is proportional to the friction factor, $f(Re_{vh})$ which is given in Equation 3.4 [Shah and Bhatti, 1987].

$$F_l = \frac{f(\text{Re})_l P_l^2 m_l}{8 N_g r_l A_g^3 h_{fg}} \quad (3.3)$$

$$F_v = \frac{f(\text{Re})_v P_v^2 m_v}{8 r_v A_v^3 h_{fg}} \quad (3.4)$$

The effect of inclination is important in determining the maximum capillary limitation of a heat pipe. Preliminary experimental data show that the capillary limit of the ceramic heat pipes in the vertical orientation (with the evaporator lower than the condenser) can be two to three times higher than in the horizontal orientation. The reason for this is that gravitational body forces assist the working fluid in getting back to the evaporator. The effect of the inclination component is provided by hydrostatic pressure variation component, $-r_g L_{\text{eff}} \sin \theta$, in Equation 3.2.

The wetting of the working fluid to the wick material is another very important parameter in determining the capillary limitation. The first term in the numerator of Equation 3.2, $\sigma \cos \theta$, represents the capillary driving forces due to the surface tension of the working fluid and the wetting angle of the working fluid and the wick material. It is common practice to find the maximum capillary limit by setting the wetting angle to zero. This represents the ideal case where there is perfect wetting. This approach is not too unreasonable since many researchers are testing heat pipes made of copper and aluminum, which have small wetting angles. However, for the heat

pipes studied in this research, the ceramic materials have wetting angles ranging from 20 to 65 degrees, and hence, they are not wetted as readily as the metal shell materials by water.

Since the vapor and the working fluid flow in opposite directions, there is a shear stress interaction at the liquid-vapor interface. This interaction retards the flow of the liquid, hence reducing the capillary limitation of the heat pipe. The inclusion of the shear stress interaction in the capillary limitation formulation has been shown to improve accuracy of predicted results and is incorporated in most models by researchers. The friction factor, $f(\text{Re}_{lh})$, is determined using Equations 3.5 and 3.6 which include the shear stress interaction between the vapor flow and the liquid. Finally, the effect of the shear stress interaction is included in the capillary limit calculation by the use of Equation 3.7 [Schneider and DeVos, 1980].

$$f(\text{Re})_{lh0} = 8D_g^2 \left\{ \frac{w_g^2}{4} \left[1 + 2 \frac{D_g}{w_g} \right]^2 \left[\frac{1}{3} - \frac{32w_g}{\rho^5 D_g} \tanh \left(\rho \frac{D_g}{w_g} \right) \right] \right\}^{-1} \quad (3.5)$$

$$f(\text{Re})_{lh} = f(\text{Re})_{lh0} \left\{ 1 + N_g \frac{w_g^3}{6\rho D_{vh}^3} \text{Re}_{vh} * \frac{n_v}{n_l} \left[1 - 1.971 \exp \left(\frac{-\rho D_g}{w_g} \right) \right] \right\} \quad (3.6)$$

$$\text{Re}_{vh} = 24(1 - 1.355a + 1.947a^2 - 1.701a^3 + 0.956a^4 - 0.254a^5) \quad (3.7)$$

Insight into an optimal design can be gained by showing the effect of the groove depth, D_g , and width, w_g , on the capillary limit as shown in Figure 3-4. From the figure, it is clear that an optimal groove width exists near 0.2 mm, which is approximately the same for the various groove depths shown (all other parameters held constant). It is also clear that as the groove depth increases, so does the capillary limit. The deeper groove allows for more mass flow of the working fluid while the shear stress interaction remains relatively constant because the area of the fluid which interacts with the vapor flow has not changed.

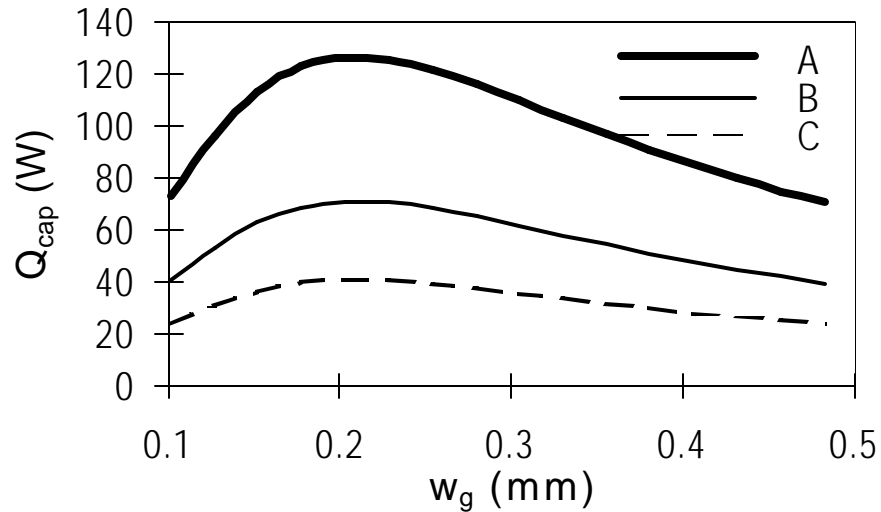


Figure 3-4. The effect on the capillary limit due to variations in groove width for groove depths of: (A) 0.64 mm, (B) 0.38 mm, and (C) 0.25 mm.

In an effort to minimize the size of the heat pipe, it is desirable to minimize the height of the vapor space. The effect of the vapor space height is shown in Figure 3-5, which shows that the capillary limit initially

increases sharply with increasing vapor space height until about 1 mm, when it then becomes relatively constant. This shows a non-linear effect of the shear stress interaction. Again, the effect of the groove depth is seen and follows the same trend as discussed for Figure 3-4. The important conclusion that is drawn from the figure is that after a certain vapor space height, there is no significant increase in the capillary limit. Hence, further increases in the vapor space height will not improve the performance of the heat pipe and serve only to increase the size of the heat pipe and most cases the thickness of the substrate itself.

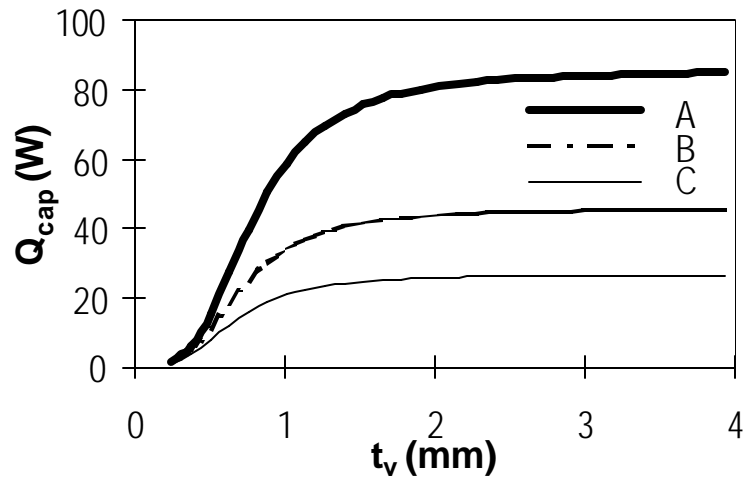


Figure 3-5. The effect on the capillary limit due to variations in vapor space height for groove depths of: (A) 0.64 mm, (B) 0.38 mm, and (C) 0.25 mm.

The effect of the interaction between the groove width and the vapor space height is made clearer by holding the depth of the grooves constant and varying the other two parameters as shown in Figure 3-6. The curves in the figure show that for small vapor space heights, smaller groove widths provide

the highest capillary limit, but as the height of the vapor space increases, increases in the capillary limit are obtained with larger groove widths. The “crossing-over” effect shown by the curves indicates that there is a competition between the shear stress interaction between the vapor and liquid flows and the ability of the wick to provide adequate mass of working fluid.

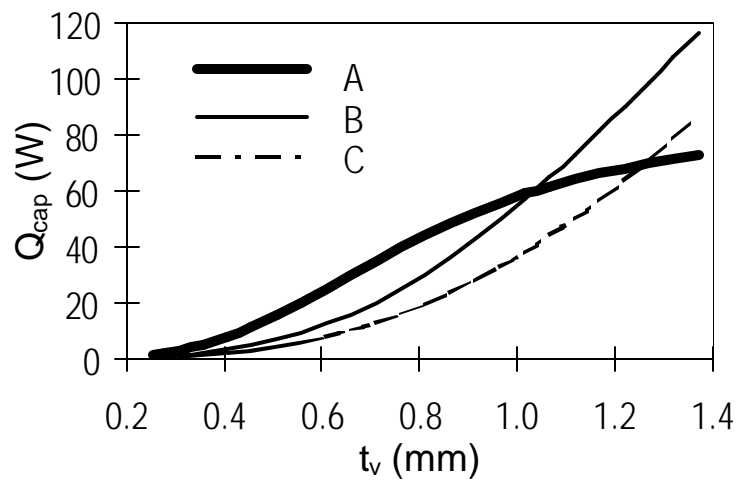


Figure 3-6. The effect on the capillary limit due to variations in vapor space height for groove widths of: (A) 0.10 mm, (B) 0.25 mm, and (C) 0.38 mm.

Small vapor space heights cause greater shear stress interaction, hence, only smaller groove widths can minimize the surface area of the working fluid interacting with the vapor flow. However, at some point, the vapor height is large enough that the shear stress interaction becomes negligible and the capillary limit becomes strongly dependent on the cross-sectional area through which the working fluid can flow.

Embedded Ceramic Heat Pipe Design

It was the primary objective of this research to develop embedded heat pipes using conventional materials and fabrication processes as much as possible. This objective drove the development of the two types of axially grooved wick structures used in this research. By no means are these wick designs considered to be optimal nor are they proposed to be highly efficient. Rather, a conceptual validation was sought using an approach that was the most compatible with current conventional cofire technology. In this manner, a baseline could be established for comparison to future, more complex designs which may or may not require new fabrication methods or materials. The first approach was to micro-machine the grooves directly into the green tape. The second approach was to use the thickness of the tape in an advantageous manner to create the grooves without the micro-machining process, but by using a standard routing process. Both these approaches will now be described.

In a conventional flat heat pipe, the wick structure is typically placed on the interior surfaces which are parallel to the heat and cooling surfaces. For simplicity, let these interior surfaces be defined as the top and bottom sides of the heat pipe. In order for grooves to be fabricated into the top and bottom surfaces of the heat pipe, the grooves must be cut into the layer(s) of tape that will be used to create the top and bottom shell surfaces of the heat pipe as shown in Figure 3-7.

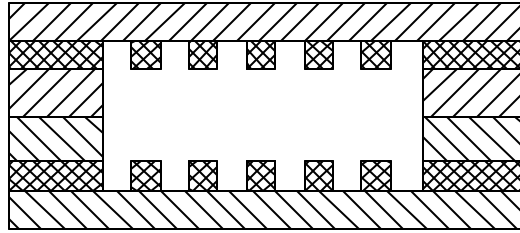


Figure 3-7. Axially cross section of an axially grooved heat pipe with the wick oriented on the top and bottom surfaces of the heat pipe.

All patterning of the ceramic tape must be performed in the green (unfired) state. After firing, all the layers of tape become a single monolithic structure, hence, the interior of the pipe is no longer accessible. Hence, machining a series of very fine grooves into the tape, requires numerically controlled machining or laser cutting techniques, both of which are costly, time consuming, and difficult to perform on unfired green tape. Additionally, if the grooves are formed by cutting a series of fine slots through a single layer of ceramic tape (as depicted in the figure), a handling problem arises in which the small lands between the grooves tear. Additionally, during the lamination process, no pressure can be applied to the lands, hence, poor adhesion is obtained to the layer of tape at the bottom of the grooves.

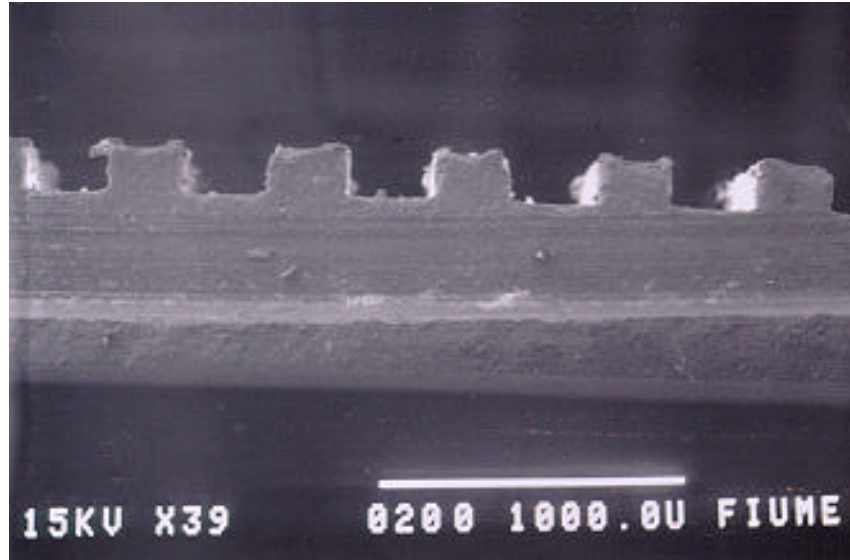


Figure 3-8. Micrograph showing top/bottom axial groove wick structure fabricated in high temperature cofire ceramic using a micro end-milling process.

The only solution to this fabrication issue is to machine the grooves into a thicker piece of cofire tape using an end milling process. This technique has been demonstrated at FIU in high temperature cofire tape which was 0.024 inches thick. High definition grooves were fabricated, but only down to 0.010 inches in width, which is larger than the desired width of 0.004 to 0.006 inches. The difficulty with micro-machining is the fine tooling required, which is fragile and costly. The conventional design is feasible and may be improved further with more research. An example of the micro-machined axial grooves is shown in Figure 3-8.

A common fabrication technique used in ceramic cofire manufacture is the cutting of slots and holes into each layer of tape. These features are created either by numerically controlled routing or by a die-cut stamping

process. Since the cofire process involves a lamination of several layers of ceramic tape to form a single monolithic structure, slots can be cut into each layer of tape forming the heat pipe, except that two slot widths will be alternated on each layer of tape. Hence, the same technique used to form the vapor space can be applied to create narrow grooves. An example of a heat pipe cross-section using the side wall grooves is shown in Figure 3-9.

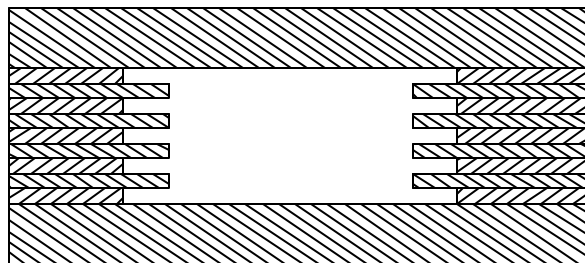


Figure 3-9. Axial cross-section of a heat pipe with the axial grooves oriented along the side walls.

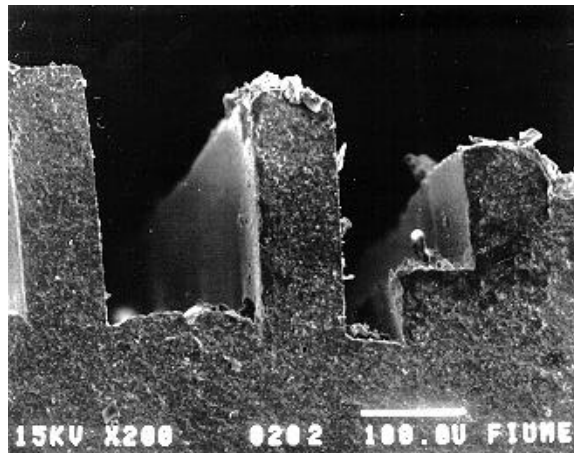


Figure 3-10. Micrograph showing “side-wall” axial groove wick structure fabricated in low temperature cofire ceramic.

The major advantage of this concept is that axial grooves may be fabricated using current manufacturing processes in cofire substrate technology. To fabricate the heat pipe, each layer of tape only needs to have a slot cut into it, either by die stamping, laser cutting, or NC routing. Another advantage of this design is that typical ceramic cofire tape has a thickness from 0.004 to 0.009 inches. Hence, by choosing a thin tape, axially grooves with small widths and spacing can be obtained just by stacking the tape. Preliminary tests have shown that axial grooves can be fabricated with the groove depth being three times the groove width after the firing process. An example of high aspect ratio grooves fabricated in low temperature cofire ceramic is shown in Figure 3-10. Grooves with such aspect ratios will be highly efficient for the anticipated heat pipe designs. Narrow, deep grooves provide a higher mass flow of working fluid while minimizing the surface area of the fluid exposed to the vapor flow. Hence, the liquid-vapor shear stress interaction is minimized.

Evolution of Ceramic Heat Pipe Prototypes

In the development of the prototype ceramic heat pipes, many samples were fabricated and various tests were performed. Indeed, the development of an embedded heat pipe in a ceramic substrate required the evaluation of several factors, including conventional and new fabrication processes, materials characterization, and effective heat pipe design as dictated by theory and practice.

In the development of the research grant that funded this investigation, a strategic decision was made to demonstrate the cofire ceramic embedded heat pipes using HTCC alumina first, and later to extend the concept to LTCC materials. Initially, the capability to manufacture cofired ceramic substrates was not available at FIU. Hence, during the development of the infrastructure to allow for cofired ceramic production, first-generation ceramic heat pipe prototypes were fabricated using post-fired alumina substrates that were laser machined to create axially grooved wick structures and vapor spaces. These substrates were 0.64 mm (25 mil) in thickness and to create a heat pipe, they were stacked and bonded together with a glass dielectric thick film ink. These prototype heat pipes were used to evaluate the ability to charge small heat pipes at FIU, the attachment of the filling tubes, and to show some feasibility of the concept by getting some positive measurable performance. Consequently, six of these heat pipes were tested to obtain preliminary thermal performance data to establish the feasibility of the embedded ceramic heat pipe concept [Zampino et al., 1997, 1998].

The second generation of heat pipe samples were fabricated in green HTCC tape with just the vapor space cavities to assess the feasibility of building long open channels in a ceramic substrate. Over fifty such pipes were generated with multiple channel widths. These samples were not used in any testing but established the feasibility of the mass fabrication of heat

pipes in large area substrates. Some of these samples were fabricated with only one surface to allow for wetting and other tests to be performed.

While the second generation heat pipes were being fabricated, testing was performed on machining axially grooved structures into the top and bottom surfaces of the heat pipe. Additionally, axial grooves were developed along the side walls of the heat pipe. With the fabrication methods developed, several third generation heat pipes were fabricated. These samples were further developed by polishing the top and bottom surfaces of the substrate, fabrication and testing of the platinum heaters, and the attachment of the filling tube.

Four third generation heat pipes were fabricated completely with heaters and filling tubes to allow for thermal performance testing to be performed. Two of these samples had top and bottom wick structures (HP#7 and HP#8), and two had side-wall wick structures (HP#9 and HP#10). While data was collected on all of these heat pipes, the most complete set of data was obtained using HP#10, which was used to assess single and multiple heater configurations at various orientations.

During the testing of these four samples, the first three samples (HP#7, 8, and 9) failed during testing with the ceramic material cracking. A failure analysis indicated that the crack was initiated by a breakdown in the platinum heater metalization, which caused a sharp rapid rise in temperature leading to a thermal shock failure of the ceramic under the

heater. Further development of the platinum heater fabrication process resulted in higher quality heaters which did not fail during operation. The improved heater process was employed on HP#10, and with the minimal machining operations required for the side wall groove design, this sample was found to work extremely well without failure for a rigorous testing period over three months.

Fabrication of Embedded Heat Pipe Prototypes

Patterning of the ceramic green tape was performed using an OZO Diversified Model 17 Manufacturing System. The OZO Model 17 is a numerically controlled micro-machining system capable of performing operations such as drilling, routing, and end-milling with a precision of 0.001 inch. It is equipped with two high speed spindle systems and an assortment of NC machining tools (bits and cutters).

Thick film metalizations were screen printed on the ceramic tape to provide for attachment of the filling tubes and for creating platinum thick film heaters on the surface of the substrate. Screen printing operations were performed on an MPM Model T-100 Screen with a 5x5 inch screen capability. Patterns were created using 5x5 inch stainless steel screens with a 375 mesh at a 45 degree orientation. The emulsion used on the screens had a thickness of 1.7 mm. A variety of thick film ink systems were used during the development of the prototypes, however, two inks were eventually used regularly with success. For attachment of the fill tubes and to create solder-

able surfaces for attachment of lead wires for the surface heaters, a high silver bearing Palladium-Silver thick film ink was used. For the fabrication of the heaters, a Platinum ink was used. The fabrication of the heaters will be discussed in greater detail later.

The lamination of the cofire tape stacks prior to firing was performed using a Carver Hydraulic Press fitted with two temperature controlled platens. Typical lamination of cofire ceramics is performed at 70 °C at a pressure of 3000 psi. However, the lamination process may be slightly different for each tape due to its material response. Ceramic tapes are viscoelastic in nature and can flow quite readily under pressure and elevated temperatures. The successful lamination of a stack of ceramic cofire tape, especially with internal cavity structures, such as heat pipes, is more of an intuitive “seat-of-the-pants” process than a scientific one at this time. For the heat pipes used in this study, the lamination process was varied as needed to create a successful prototype.

Thermal loads were applied to the substrate by thick film heaters fabricated directly on the surface of the substrate. In this manner, the heater was in intimate contact with the substrate surface with no thermal interface resistance. The heaters were made from serpentine thick film resistors patterns using a standard platinum thick film ink (ESL Inc.). Platinum was chosen as it has a linear temperature coefficient of resistance (TCR) over the range of temperatures anticipated in this study.

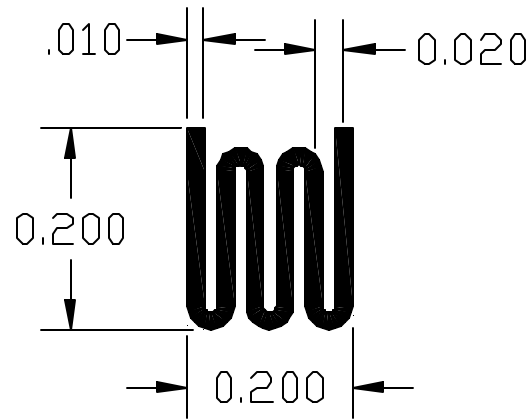


Figure 3-11. Thick-film platinum heater geometry. Dimensions are in inches.

The heater design used on the prototypes in this study is shown in Figure 3-11 and has the nominal dimensions of 0.300 x 0.300 inches. The size was chosen to be representative of typical high power semiconductor components. The platinum metalization used to fabricate the heaters had a nominal sheet resistivity of 50 m Ω per square. For the heater design used this gave a heater with total resistance between 7.5 and 10 ohms over the operating range of the heat pipe.

The platinum thick film ink produced a well defined resistor pattern that did demonstrate linear TCR performance, but that the resistor material was prone to thermal runaway and element burnout under moderate thermal loads (over 3 W). The failure of the heater element caused a large thermal spike at the surface of the substrate initiating a crack in the ceramic which led to the mechanical failure of three of the heat pipe samples (HP#7, 8, and

9) discussed in this study. An investigation of the structure of the platinum indicated that the thick film exhibited a porous structure. A technique was developed to overcome this problem by screen printing a second layer of platinum over the initial post-fired pattern [Lopez, 2001]. Using the new technique, it was found that the platinum from the second firing diffused into the porous structure of the post-fired platinum yielding an exceptionally dense resistor structure after the second firing. It was found that the enhanced resistor metalization was impervious to burnout, even when operated at temperatures in excess of 700 °C with hundreds of on/off cycles. The enhanced resistor metalization was used on the fourth heat pipe (HP#10) discussed in this study without any failure.

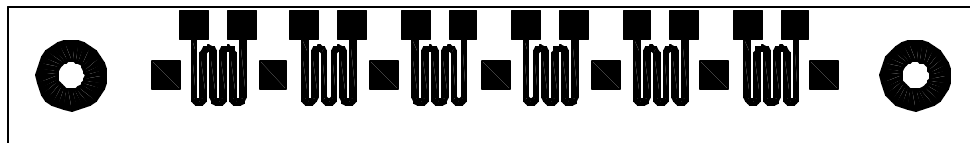


Figure 3-12. Typical artwork for thick film heater metalization on substrate surface.

To provide for multiple heating locations along the length of the heat pipe, a series of heaters was patterned on the substrate's surface. The artwork pattern shown in Figure 3-12 shows six heaters connected to an set of contact pads along the edge of the substrate for electrical hookup. Also shown in the artwork is the two metalizations around each of the fill holes for the heat pipe. A hole is located at each end of the heat pipe. In this study,

one of the holes was sealed over with a solder patch and/or a copper patch while the other was used for the fill tube attachment. The square pads between the heaters are for thermocouple bonding. The circular pads at each end are for fill/vent tube attachment. All soldering operations were performed with rosin core lead tin eutectic solders. A picture of a completed heat pipe assembly is shown in Figure 3-13. The heat pipe in the picture has the vent hole sealed over with solder and a copper filling tube attached to the other filling hole. Soldered to the contact pads along the edge of the heat pipe is the lead wires for each of the heaters along the surface.

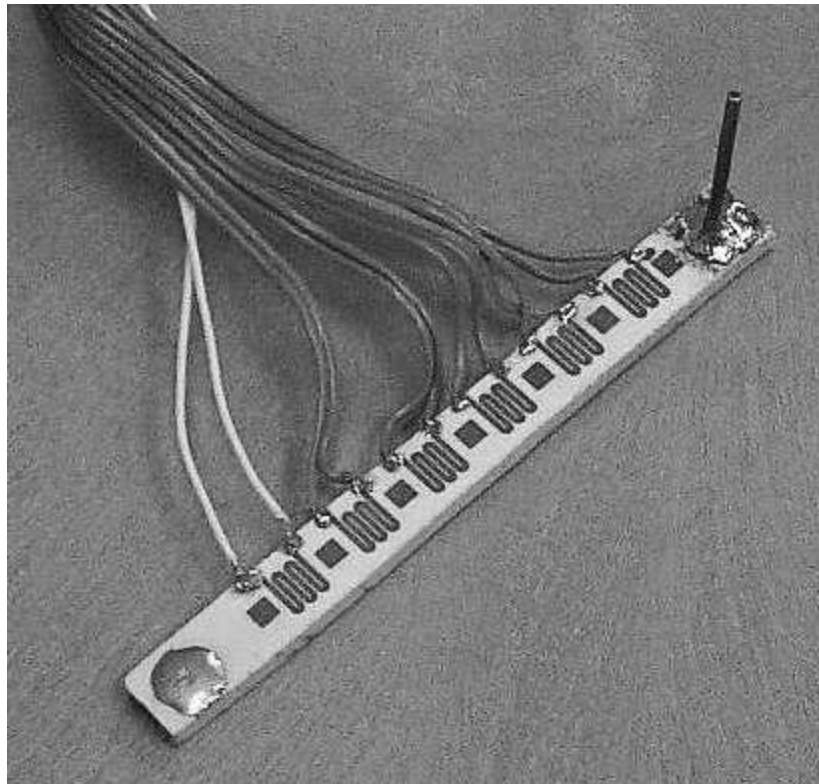


Figure 3-13. Picture of typical assembled heat pipe showing heaters, lead wires, and filling tube.

The charging process for heat pipes involves getting the working fluid inside the heat pipe, obtaining the correct amount of saturated vapor, liquid, and getting the correct working pressure. Miniature heat pipes, by their nature, make the charging process quite difficult, since small variations in the amount of working fluid can make the pipe not operate. A conventional technique for charging a heat pipe is to “boil off” excess working fluid and gases out of the heat pipe prior to sealing. This technique is common for large commercial heat pipes. However, for miniature heat pipes with very small volumes of working fluids this method is not effective because it is very easy to eject all of the working fluid out of the pipe prior to sealing it. Therefore, an alternative technique was needed.

The heat pipes in the study were charged using a method developed at FIU [Cao et al., 1997]. The method has been proven reliable and repeatable in several experiments for heat pipes of various volumes. The method has been found to have a precision of under 5 μL (micro-liters) for heat pipes with charging volumes in the range of 30 to 100 μL . The charging method is summarized briefly:

1. The heat pipe is evacuated ($10^{-2} < p < 10^{-3}$ torr) to remove non-condensable gases and to aid in the cleaning of the pipe.
2. An arrangement of a gas chromatograph syringe with a locking sample section, small diameter tubing and two teflon seals are used to inject the working fluid directly into the evacuated heat pipe while under

vacuum. Losses of charge back into the connecting tubing when vapor flash occurs is minimized by the Teflon seals.

3. The filling tube of the heat pipe is sealed by crimping and soldering.

IV. Modeling and Simulation

Due to the three dimensional structure of the heat pipe, the use of one dimensional thermal network models can, at best, provide a first order estimate of the heat transfer through the shell material. Hence, the use of finite element analysis (FEA) is highly appropriate for modeling the conduction heat transfer through the shell material of the heat pipe. For the purposes of this study, FEA will be employed to determine the conduction of heat through the shell material based on various boundary conditions which are intended to reflect the operation heat pipe within the solid material. No attempt will be made to actually model the two-phase processes within the heat pipe such as evaporation and condensation, or the liquid or vapor flow dynamics. The numerical modeling of these processes is in itself a major research task which is currently being investigated by others.

Embedding heat pipes in ceramic substrates raises a different paradigm from conventional heat pipes. First, the shell materials that would be used will have relatively low thermal conductivities, and second, the substrate is essentially a three dimensional solid in which the heat pipe occupies a very small percentage of the total volume. Furthermore, in extended applications, there may be sources of heat not directly on top of the heat pipe or possibly there can be multiple heat pipes cooling multiple components. Additionally, ceramic substrates and electronic packages are becoming three dimensional, extending beyond the traditional planar design.

In fact, the use of cofired ceramic technology lends itself to the production of electronic packages which are closer to a brick in shape than a relatively thin planar substrate. Hence, three dimensional heat conduction through the shell material will play a significant role in the thermal management design for the electronic package. To address this new paradigm, modeling techniques for embedded heat pipes would need to be more focused on the substrate rather than on the internal workings of the heat pipe. Thus, FEA will be the appropriate tool for rapid modeling of the substrate system. The primary limitation is that the heat pipe can not be modeled directly at this time, so appropriate boundary conditions will be necessary to accurately represent the heat transfer provided by the heat pipe.

In this study, the conduction heat transfer through the shell material will play a significant role in interpreting the empirical results discussed in Chapter 6. As discussed in the last section, the thermal resistance of the shell material will be the dominant factor in the temperature rise from the heat sink to the heater. Of particular interest is the temperature distribution through the shell material since the wick structures rely on both direct and indirect thermal paths for the heat to travel from the heater to the effective evaporator section of the wick.

Theoretical Overview of FEA for Heat Transfer

Consider a three dimensional body volume V , and with a surface area of S , for which the material obeys Fourier's law of heat conduction,

$$q_i = K_{ij} \frac{\partial T}{\partial x_j} \quad (4.1)$$

for which q_i is the rate of heat flow conducted per unit area in the direction i , K_{ij} is the thermal conductivity tensor for the material and $\partial T/\partial x_j$ is the temperature gradient vector in Cartesian coordinates. As written, K_{ij} would contain nine components, however, the principle of irreversible thermodynamics shows that the thermal conductivity tensor has to be symmetric. This leads to the component form for (4.1) to become,

$$\begin{Bmatrix} q_x \\ q_y \\ q_z \end{Bmatrix} = - \begin{bmatrix} k_{xx} & 0 & 0 \\ 0 & k_{yy} & 0 \\ 0 & 0 & k_{zz} \end{bmatrix} \begin{Bmatrix} \partial T/\partial x \\ \partial T/\partial y \\ \partial T/\partial z \end{Bmatrix} \quad (4.2)$$

Now applying conservation of energy to the interior of the body yields the heat conduction equation and dropping the redundant indices gives,

$$\left[\frac{\partial}{\partial x} \left(k_x \frac{\partial T}{\partial x} \right) + \frac{\partial}{\partial y} \left(k_y \frac{\partial T}{\partial y} \right) + \frac{\partial}{\partial z} \left(k_z \frac{\partial T}{\partial z} \right) \right] + q''' = \rho c \frac{\partial T}{\partial t} \quad (4.3)$$

where q''' is the heat generation per unit volume within the solid, ρ is the density of the material, c is the specific heat of the material, and t is time. This is the governing equation for conduction heat transfer in a solid material, allowing for the thermal conductivity to be different in each coordinate direction, internal heat generation, and transient heat transfer response.

For the purposes of the analysis in this study, the substrate/shell material is considered to be isotropic with constant thermal conductivity. Also, there will be no heat generation in the solid material and only steady state solutions are desired. Thus the heat conduction equation (4.3) simplifies to,

$$\nabla^2 T = 0 \quad (4.4)$$

which is known as Laplace's equation.

The boundary conditions that can be prescribed on (4.4) and are appropriate for the analysis in this study are the following:

$$\text{Prescribed Temperature:} \quad T(x) = T_s(x) \quad (4.5a)$$

$$\text{Prescribed Heat Flux:} \quad -k \frac{\partial T}{\partial n} = q^s \quad (4.5b)$$

$$\text{Adiabatic Boundary:} \quad \frac{\partial T}{\partial n} = 0 \quad (4.5c)$$

$$\text{Surface Convective:} \quad -k \frac{\partial T}{\partial n} = h(T_s - T_\infty) \quad (4.5d)$$

where T_s is the surface temperature, T_∞ is the sink or fluid temperature, n is the normal vector to the surface, h is the convective heat transfer coefficient, and q^s is the surface heat flux entering the material.

The application of the governing equations and the boundary conditions to a three dimensional model of the embedded heat pipes forms is appropriately performed using FEA, a numerical technique which approximates the solution of continuum mechanics problems using an

extension of the Raleigh-Ritz procedure. The method reduces a continuum with an infinite number of degrees of freedom to a discrete system with a finite number of degrees of freedom. The continuum is subdivided by finite elements which represent small finite volumes of the solid material. Elements are connected using a finite number of points called nodes to which loads can be applied. There is an assemblage of elements such that an approximate admissible solution is obtained, typically through matrix solution methods [EMRC, 1995].

In the present analysis, the embedded heat pipe were modeled and solved using a commercially available FEA product, NISA Version 6.0, from Engineering Mechanics Research Corporation. To avoid treating the software as a "black box" which generates results, a brief summary of the finite element formulation used in the software will be given. For heat transfer analysis, NISA solves heat transfer problems by the following functional which represents the potential energy of the system,

$$\begin{aligned} \Pi = \int_V \frac{1}{2} \left\{ k_x \left(\frac{\partial T}{\partial x} \right)^2 + k_x \left(\frac{\partial T}{\partial x} \right)^2 + k_x \left(\frac{\partial T}{\partial x} \right)^2 - 2Tq^B \right\} dV \\ - \int_S T_S q^S ds + \int_V T \left(\mathbf{r} c \frac{\partial T}{\partial t} \right) dV - \sum_i T^i q^i \end{aligned} \quad (4.6)$$

where q^S includes all types of surface heat flow (i.e. prescribed heat flux and convection), q^i represents concentrated heat flow at specific nodes with temperature T^i . For heat transfer analysis, the potential energy is set to zero, converting (4.6) into,

$$\begin{aligned} \int_V \mathbf{d} \left(\frac{\partial T}{\partial x} \right)^T \mathbf{K} \left(\frac{\partial T}{\partial x} \right) dV + \int_V \mathbf{dT} \left(\mathbf{r} c \frac{\partial T}{\partial t} \right) dV \\ = \int_V \mathbf{dT} q^b dV + \int_S \mathbf{dT}^S q^S dS + \sum_i \mathbf{dT}^i q^i \end{aligned} \quad (4.7)$$

where δ denotes a "variation in" and,

$$\left(\frac{\partial T}{\partial x} \right) = \left[\frac{\partial T}{\partial x} \quad \frac{\partial T}{\partial y} \quad \frac{\partial T}{\partial z} \right]^T \quad \text{and} \quad \mathbf{K} = \begin{bmatrix} k_{xx} & 0 & 0 \\ 0 & k_{yy} & 0 \\ 0 & 0 & k_{zz} \end{bmatrix}$$

Equation 4.7, in its general and complete form represents a nonlinear transient governing equation for the heat transfer in a arbitrary volume of material. Hence, Equation 4.7 can be applied to each of the finite elements that now make up the volume, leading to a set of equations that need to be solved simultaneously. Fortunately, for steady state analysis, this set of equations simplifies to a linear set of equations.

The FEA software starts with Equation 4.7 and follows a conventional Galerkin finite element procedure, introducing conventional shape functions to the elements to ensure that the temperature gradient across an element is compatible with the temperature at each of the element's nodes. This is performed using the following assumptions:

$$T(x) = \sum_{i=1}^n N_i(x) T_i \equiv \mathbf{NT} \quad \text{and} \quad \frac{\partial}{\partial x} T(x) = \sum_{i=1}^n \frac{\partial}{\partial x} N_i(x) T_i \equiv \mathbf{BT} \quad (4.8)$$

where i ranges from 1 to the number of nodes in the element, and T_i are the nodal temperatures. Hence, the final finite element equation for steady state heat conduction analysis with no internal heat generation and prescribed

temperature, prescribed heat flux, and convection boundary conditions is written as,

$$(\mathbf{K}_c + \mathbf{K}_h)\mathbf{T} = \mathbf{Q}^s + \mathbf{Q}^h \quad (4.9)$$

where the thermal conductivity matrix for conduction is given by,

$$\mathbf{K}_c = \int_V \mathbf{B}^T \mathbf{K} \mathbf{B} dV \quad (4.10)$$

and the thermal conductivity matrix due to convection B.C. is given by,

$$\mathbf{K}_h = \int_S h \mathbf{N}^{sT} \mathbf{N}^s dS \quad (4.11)$$

and the heat flux vector due to prescribed surface heat flux is given by,

$$\mathbf{Q}_s = \int_S q^s \mathbf{N}^{sT} dS \quad (4.12)$$

and the heat flux vector due to the convection B.C. is given by,

$$\mathbf{Q}_h = \int_S h T_e \mathbf{N}^{sT} dS \quad (4.13)$$

The software does not provide detailed documentation regarding the exact solution algorithm(s) used, as this is the most proprietary part of a commercial FEA program, and in many cases typical FEA software may utilize different algorithms depending on the overall size of the problem and the condition of the conductivity matrix (i.e. wavefront size, sparceness of off-diagonal elements etc.). However, after assemblage of the matrices and vectors given in Equation 4.9, the equation essentially enters the form of $[\mathbf{K}]\{\mathbf{T}\} = \{\mathbf{Q}\}$. This is a linear static analysis and the software solves this

system by first performing a wavefront minimization in which the elements are resequenced to minimize the numerical wavefront. The equilibrium equations are then solved by a frontal technique which uses a wavefront solution method, thus avoiding decomposition of the conductivity matrix [K] so as to obtain its inverse.

FEA Models of Embedded Heat Pipes

Two models were created to model the embedded heat pipe, one to represent the heat pipes with a Top/Bottom wick structure, and another to represent the heat pipes with a Side-Wall wick structure. The models were made using the measured dimensions of the actual heat pipes tested in this study including the location of the heaters along the surface of the substrate. More specifically, the two FEA models were intended to be as representative as possible of HP#7 and HP#10, and hence forth will be referred to by the heat pipe name they represent. The dimensions for these two heat pipes in presented in later in Chapter 5.

A symmetry condition exists along the axial length from the evaporator end-cap to the condenser end-cap of the heat pipe. Hence, only one-half of the heat pipe needs to be modeled. Using this symmetry, the total model size could be reduced allowing for faster computational times. The general structure of the models is shown by the feature line plot in Figure 4-1, in which the internal cavity forming the heat pipe can be seen. The element mesh for same model is also shown in Figure 4-1. As can be seen

from the figure, a uniform mesh was used using hexagonal brick elements. Due to the simplicity of the structure, a very organized and uniform mesh could be created.

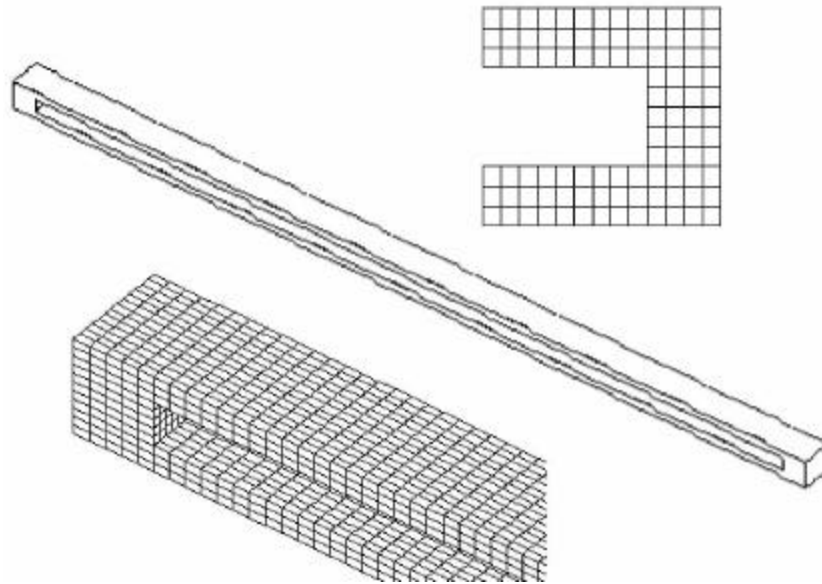


Figure 4-1. Composite showing representative parts of FEA models (HP#7 model shown): One-half symmetry model, mesh detail, and cross-section of model.

Preliminary models were created using both first and second order elements which yielded identical solutions. Additionally, the model was meshed with a more dense mesh to check mesh independence of the model. Again, identical results were obtained. This is quite expected as the model is rather simple with well defined boundary conditions. From the preliminary models, two computationally efficient models were created using first order elements. For HP#7 (Top/Bottom Wick) the model had 18331 elements and 24673 nodes, and for HP#10 (Side-Wall Wick) had 12608 elements and 15870

nodes. Actual computational times were under 200 seconds on a 233 MHz Pentium II processor with 128 Mb of RAM.

In the models, the boundary conditions used included prescribed temperature (Eqn. 4.5a), prescribed heat flux (Eqn. 4.5b), and convection (Eqn. 4.5d), noting that the finite element method implicitly applies the adiabatic condition (Eqn 4.5c) automatically at all model boundaries unless another boundary condition is prescribed. The prescribed temperature boundary condition was applied for all nodes that coincided with the interface between the substrate and the cold-plate. In the models, the temperature at these nodes was prescribed to be at 35 °C. At the location of an active heater, a prescribed heat flux is applied on all of the element faces along the surface of the substrate that correspond to the heater's cross-sectional area. The magnitude of the heat flux was obtained by dividing the power dissipated at the heater by the area of the heater pattern. Finally, convection heat transfer boundary conditions was used to model the heat transfer from the wick surface to the vapor in the heat pipe. Recalling Equation 4.5d,

$$-k \frac{\partial T}{\partial n} = h(T_s - T_\infty) \quad (4.5d)$$

this boundary condition requires three parameters to be known prior to model solution: k , the solid material thermal conductivity; T_∞ , the bulk fluid temperature; h , the coefficient of convection heat transfer. In the entire model the solid material was modeled as alumina with a thermal conductivity of 29 W/m-K. The bulk fluid temperature in this case,

represents the vapor temperature of the heat pipe, for which the value chosen was obtained from the experimental data. The model has no ability to predict the vapor temperature so it must be estimated prior to the model solution. For the two models, the vapor temperatures of 65 and 52 °C were used for the HP#7 and HP#10 models, respectively. Lastly, the coefficient of convection heat transfer was also found using the experimental data. Review of literature related to boiling and evaporation indicated that the typical range of the convection heat transfer coefficient range from 10,000 to 30,000 W/m²-K. Through iterative runs, a value of 15,000 W/m²-K was found to provide solutions that were in excellent agreement with measured temperature data.

The application of the convection boundary condition inside the heat pipe had a direct and significant impact on the results of the models. By applying the convection boundary condition in various manners along the inside surface of the heat pipe, various wick conditions could be simulated and the effect on the temperature distribution along the heater side surface of the substrate could be determined.

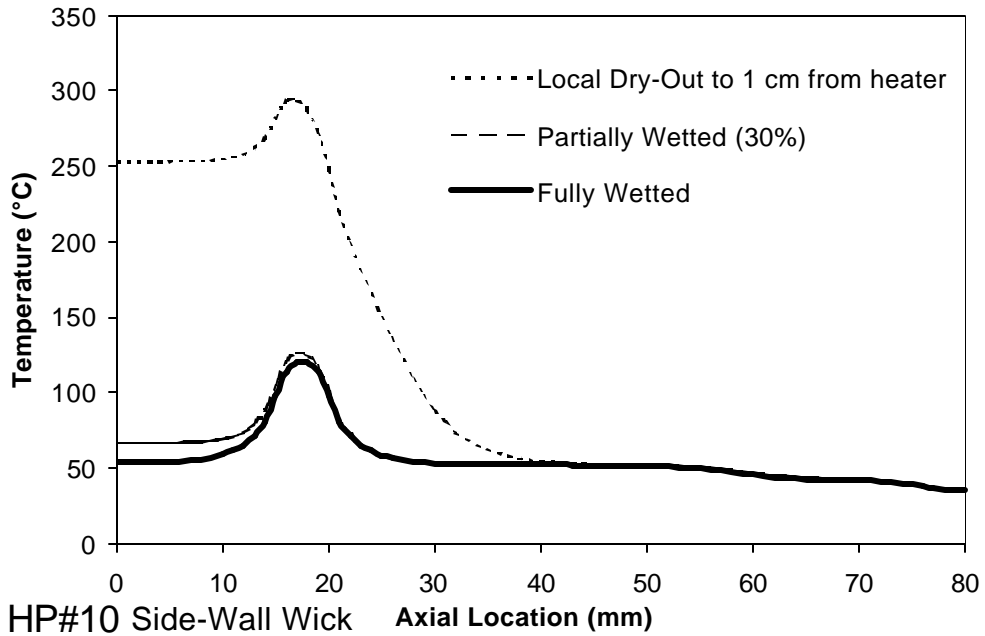
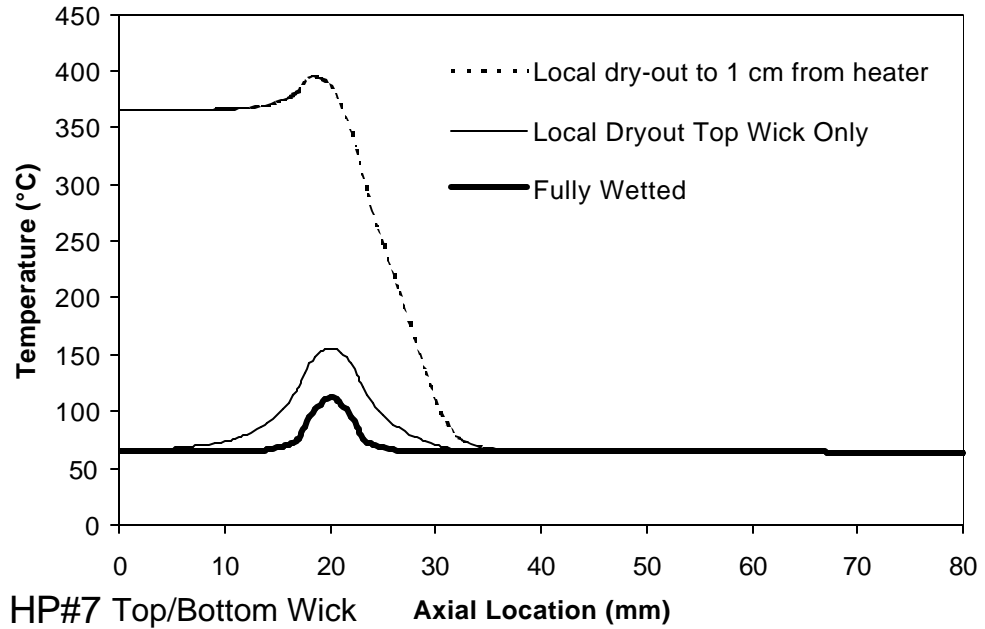


Figure 4-2. Axial temperature distribution for HP#7 and HP#10 with 10 W thermal load at heater location H1 and three wick conditions.

Heat Pipe Model	Wick Condition	Heater to Vapor Thermal Resistance (°C/W)
HP#7	Fully wetted, top and bottom sides	4.7
	Top side local dry-out to 1cm downstream from heater, bottom side fully wetted	8.9
	Both top and bottom sides local dry-out to 1 cm downstream from heater	33
HP#10	Fully wetted, both sides, full height of side walls	6.8
	Partially wetted (29% area) along both sides near condenser side of substrate	7.4
	Partial dry-out to 1 cm downstream from heater	23

Table 4-1. Comparison of thermal resistance from heater to vapor for various wick structures and dry-out conditions.

In the models, the inside surfaces of the heat pipe were smooth, without any detail of the wick geometry. This was done to keep the models as simple as possible and to use as few assumptions as possible in simulating a boundary condition, for which the true complexities exceed the capability of the numerical method employed. To simulate a wetted portion of the wick where evaporation/condensation could occur, the convection boundary condition was applied to the element surfaces that coincided with the wick location. That is, for HP#7 (Top/Bottom Wick), the boundary condition was only applied along the top and bottom surfaces of the heat pipe cavity.

Likewise, for HP#10 (Side-Wall Wick), the boundary condition was only applied along the side walls of the heat pipe's cavity.

The baseline case for both models was for the wick to be wetted along its entire length of the heat pipe, and hence, a convection boundary condition was applied on the entire wick surface along the entire length of the heat pipe. In addition to the baseline case, it is of interest to assess the effect of various wick wetting conditions, such as, dry-out of the wick at a certain axial location, or the partial dry-out of the wick on one side of the heat pipe etc. The FEA models allowed for rapid assessment of these conditions. Various wick conditions were run for each of the models and the results are shown in Figure 4-2.

Using the results shown in Figure 4-2, quantitative analysis was performed to obtain the thermal resistance of each heat pipe model operating in the various wick conditions and is shown in Table 4-1. An appropriate definition for the thermal resistance for applications in electronic packaging is given by Equation 4.14. This value would give be related to the overall system from the heat source to the heat sink. Unfortunately, using this definition for the current analysis would be misleading, because the FEA solution is not driven by the heat sink temperature at all. Rather, the convection boundary condition at the wick surface uses a predetermined value for the vapor temperature. Hence, even if the heat sink temperature was changed, the convection boundary condition would stay the same. Due to

the very high value of the convection heat transfer coefficient used in the boundary condition, the surface temperature of the wick is driven to the prescribed vapor temperature. Therefore, deriving the thermal resistance using the sink temperature would be misleading as one would only need to raise the heat sink temperature and the thermal resistance would decrease, for no conclusion physical reason.

$$R_{\text{heater-sink}} = \frac{T_{\text{heater,max}} - T_{\text{sink}}}{Q_{\text{dissipated}}} \quad (4.14)$$

Due to the convection boundary condition used in the heat pipe, the only appropriate definition for a thermal resistance would be given by Equation 4.15, which uses the maximum heater temperature and the prescribed vapor temperature. In this manner, the same thermal resistance we be obtained at any vapor temperature, as the thermal resistance is physically an attribute of the conduction heat transfer path through the shell material.

$$R_{\text{heater - vapor}} = \frac{T_{\text{heater,max}} - T_{\text{vapor}}}{Q_{\text{dissipated}}} \quad (4.15)$$

Referring to Figure 4-2, the wick condition denoted as fully wetted refers to the baseline condition described earlier. This condition provides the lowest axial temperatures, specifically the temperature rise under the heater location (denoted by the location of the peak temperature in the distribution). As indicated in Table 4-1, for the fully wetted wick condition, the heater to

sink thermal resistance for the HP#7 (Top/Bottom wick) model was 4.7 °C/W as compared to 6.8 °C/W for the HP#10 (Side-Wall wick) model. Noting that comparison between the two structures is somewhat superficial as the geometry of the shells for the two models is different. What really is important to compare is the effect that the various wick conditions have for a specific wick structure.

For both models, a localized dry-out condition was modeled whereby the wick was dry on both sides of the heat pipe at an axial position 1 cm from the heater location. Hence, the convection boundary condition was applied from $x = 30$ mm to the condenser end of the heat pipe for the HP#7 model, and from $x = 28$ mm to the condenser end for the HP#10 model. The remaining wick area had no boundary condition applied simulating a dry condition without any evaporation or condensation occurring. The result of this wick condition is a significant temperature rise under the heater as well as the surface of the substrate near the evaporator end-cap. From Table 4-1, the heater to sink thermal resistance for this wick condition are given as 33 °C/W and 23 °C/W, for the HP#7 and HP#10 models, respectively. The most important conclusion to be drawn from this is that if working fluid is not transported very close to the heater, a significant and apparent temperature rise will occur regardless of the wick structure. This is a direct result of the increased thermal path length from the heater to the location where the wick is wetted and the relatively low thermal conductivity of the shell material.

Another observation that can be made from this is that the Top/Bottom wick structure now has a greater thermal resistance than the Side-Wall Wick. Once dry-out occurs, the Top/Bottom wick structure suffers from over a ten-fold increase in the thermal resistance, while for the Side-Wall wick it only increases about 4 times.

A third wick condition is also shown in the figure which is less dramatic and more likely to occur in the heat pipes. In this condition, there is localized and partial dry-out of the wick structure. For the Top/Bottom wick structure, there is some concern that because the condenser is on one side of the substrate and the heaters are on the other, that the potential exists for the top side wick to be totally dry because no z-axis capillary transport mechanism is provided in the wick structure. Experimental data will be discussed later in Chapter 6 that will show that this is in fact not the case. However, at this point in the discussion, the third wick condition to be modeled for the Top/Bottom wick is where the condenser side wick is wetted along its entire length, but the heater side wick has dry-out occurring 1 cm away from the heater. Referring to the Figure 4-2, for the HP#7 model, it is clear that the peak temperature rise under the heater for this condition is not as drastic as for the wick with full dry-out, giving about a 50% increase in the peak temperature and a heater to sink thermal resistance of 8.9 °C/W. Now for the Side-Wall wick structure (HP#10), a similar partial dry-out condition is modeled, however, since both sides of the wick have the same orientation

relative to the condenser side of the substrate, the partial dry-out condition was modeled by applying the convection boundary condition along 29% of the total wick area which is closest to the condenser side of the substrate. The result of this wick condition, as shown in Figure 4-2 is almost no appreciable temperature rise over the fully wetted condition and a heater to sink thermal resistance of 7.4 °C/W. This occurs because both sides of the wick have identical thermal paths from the heaters to the wetted area, and in the event of partial dry-out, the impact is minimized because the wicks are oriented along the side-walls of the heat pipe cavity. In contrast for the Top-Bottom wick structure, the loss of the top side wick, forces the dissipated heat to take a significantly longer and more arduous path down along the side walls of the heat pipe cavity to the condenser side wick. This result clearly shows that the Side-Wall wick, although having a larger thermal resistance in the fully wetted condition, is less sensitive to partial dry-out conditions than the Top/Bottom wick structure.

Conduction Model	Thermal Resistance from Heater H1 to Condenser Mid-Point (°C/W)	
	HP#7	HP#10
Dry Pipe	57	66
Solid Substrate	45	58

Table 4-2. Comparison of conduction only solutions for both heat pipes.

An important model solution for the heat pipe models is that when heat is transferred only by conduction through the substrate from the heater to the cold-plate. In this case, the heat pipe is considered completely dry.

Important for comparisons later in this study is the conduction model for a solid substrate without any heat pipe cavity at all. The thermal resistance for each of these conduction models is given in Table 4-2 for each of the heat pipe models. From the table, it is apparent that the solid substrate has a slightly lower thermal resistance simply due to it having more cross-sectional area and volume of solid material between the heater location and the cold-plate. The variation in the thermal resistance between the two models is somewhat superficial as the two models do not have the same geometry. In any event, it is important to see that the magnitude of the thermal resistance in a conduction only mode is significant being around 60 °C/W for the dry heat pipe models, and about 50 °C/W for the solid substrate. These numbers represent the baseline for which the enhancement due to the addition of a heat pipe in the substrate are to be compared against.

V. Experimental Set-Up and Procedure

Experimental Set-Up

The primary experimental objective of this dissertation is to characterize the performance of the embedded ceramic heat pipe, mainly to provide for conceptual validation of the technology. In addition, the performance of the prototype heat pipe designs would provide valuable quantitative insight into the necessary design features needed for optimized design. For the thermal performance testing of the heat pipes, the experimental setup involved the following major elements: a test cell (including the heat pipe, temperature controlled cold-plate and laboratory stand), temperature controlled bath, power supply, instrumentation and data acquisition system. This system is shown schematically in Figure 5-1.

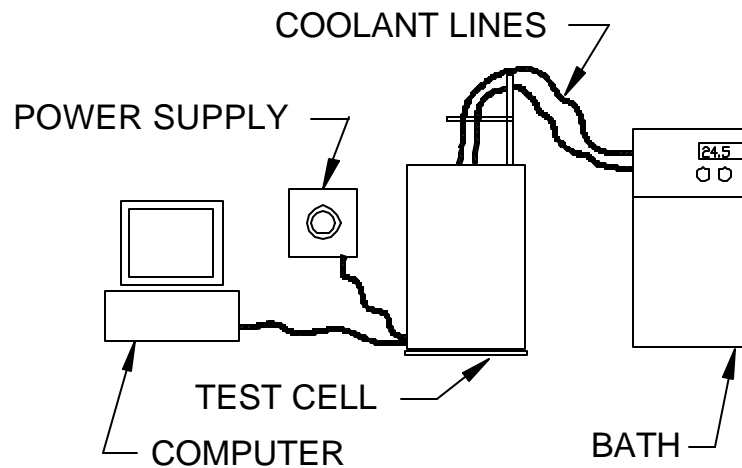


Figure 5-1. Schematic of experimental set up showing major components.

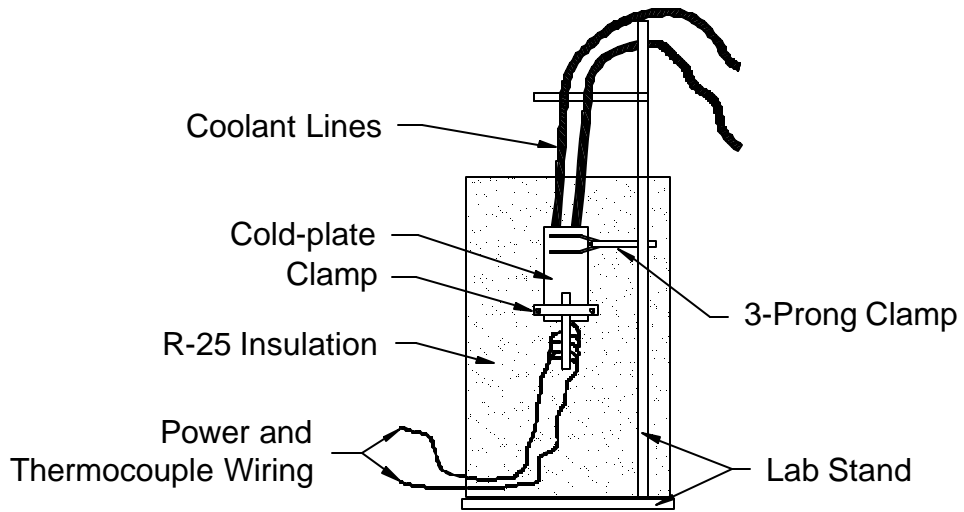


Figure 5-2. Schematic of test cell (top) showing heat pipe mounting, cold plate, wiring, lab stand and insulation jacket

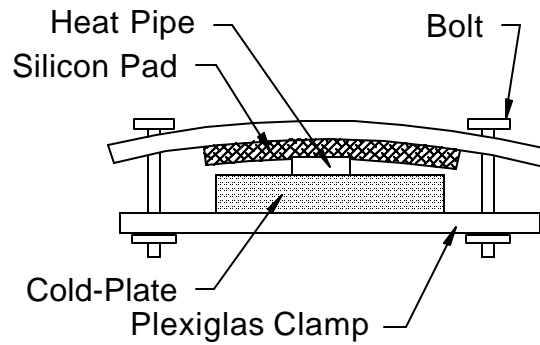


Figure 5-3. Cross-section of clamping arrangement used to secure heat pipe to cold-plate.

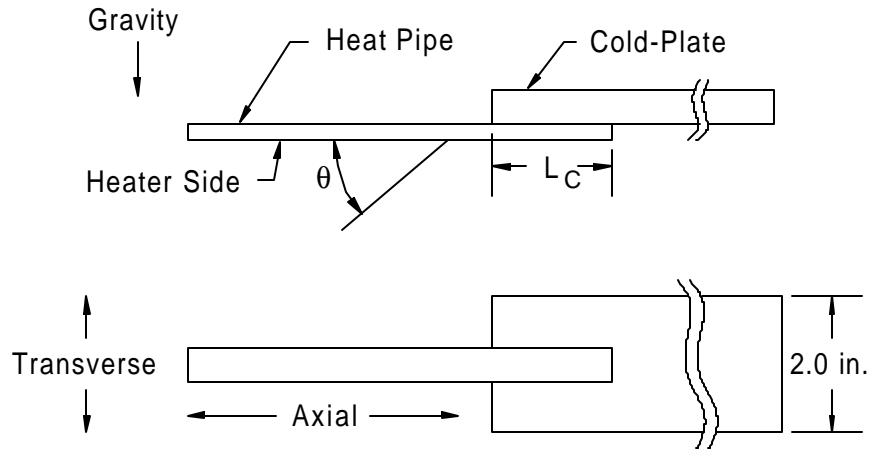


Figure 5-4. Heat pipe axial orientation relative to gravity and the axial orientation angular convention.

The test cell shown in the figure used a laboratory stand to support a copper cold-plate, to which was clamped the heat pipe under test. A more detailed schematic of the test cell is shown in Figure 5-2. As shown in the figure, the test cell included the laboratory stand, a three prong grip, a copper cold-plate (Minco Engineering Inc.), the heat pipe under test, a clamp assembly to secure the heat pipe to the cold-plate, and an insulation blanket. The cold-plate used in the experiments was 6 x 2 x 0.25 inches in dimension with a single coolant pass through it. At the end of the cold-plate, the heat pipe under test was secured by a clamping assembly shown in Figure 5-3. Approximately 2 cm of the condenser end of the heat pipe was clamped on to the cold-plate, with the remainder of the heat pipe projecting from the cold-plate as shown in Figure 5-4. Thermal grease (Omega Engineering Inc.) was used between the heat pipe and the copper surface. An estimate of the thermal resistance for this interface would be about 1.3 °C-cm²/W

($0.2 \text{ } ^\circ\text{C}\cdot\text{in}^2/\text{W}$), which would equate to about $0.65 \text{ } ^\circ\text{C}/\text{W}$ taking into account the clamped area. The clamping assembly was designed using two Plexiglas pieces, two bolts, and a silicone rubber pad. Using this arrangement the heat pipe was sandwiched between the Plexiglas pieces pressing it securely against the cold-plate. The silicon pad was used to prevent slippage and damage to the heat pipe and to reduce any heat loss into the clamping assembly. As shown in the figure, the heat pipe was extended off of the cold plate in a cantilever fashion.

Once the heat pipe was secured to the cold-plate, its orientation was checked using an inclinometer to make it parallel with the shaft on the laboratory stand. The uncertainty of this adjustment is estimated to be $\pm 2^\circ$. As shown in Figure 5.4, the axial orientation of the heat pipe with respect to gravity is indicated by the angle, θ , using the following convention: horizontal equals 0° , and vertical with the evaporator lower than the condenser is $+90^\circ$. Once the heat pipe was clamped on to the cold-plate, its orientation was adjusted by rotating the entire laboratory stand. An inclinometer was used to measure the angle of the laboratory stand's shaft, which in turn would be the orientation of the heat pipe under test. Using this method, the maximum uncertainty in the axial orientation of the heat pipe would be $\pm 4^\circ$.

It should be noted that the heat pipes were attached to the cold-plate with the heat input on one side of the substrate (by convention called the bottom or heater side) and the heat sink on the opposite side (by convention

called the top or condenser side). This configuration was chosen as a worst case scenario which could be found in typical electronic packaging applications, keeping in mind that the wick structures employed do not have any accommodation specifically for transporting working fluid from the bottom to the top side. However, to make this situation somewhat amenable, the heater side of the substrate was always oriented so that it was lower than the condenser side (refer to Figure 5-4 and note the gravity vector).

Care was taken to minimize the transfer of heat from the heat pipe to the ambient conditions or the test fixture (other than the cold-plate which is the intended heat sink). This was accomplished by using at least 10 cm of R-25 glass-wool insulation packed around all sides and ends of the heat pipe and the cold-plate assembly. Plastic "bubble wrap" was then wrapped around the insulation to keep it tightly in place and to further reduce any ambient losses. The coolant lines for the cold-plate were brought through the insulation near the top of the laboratory stand, and in a similar fashion, the thermocouple leads and the power lines for the heaters were run out near the bottom of the laboratory stand.

The cold-plate used in the experiments was cooled by circulating coolant from a temperature controlled bath (Neslab RTE-21). The coolant was an ethylene glycol and water mixture with a concentration of fifty percent. The pump on the bath provided approximately 5 liters per minute of coolant flow. Due to the flow rate of the coolant, the two gallon coolant

reservoir, and the mass/material of the copper cold-plate, the temperature of the cold-plate at the copper/ceramic interface could be kept at a steady temperature for all the power levels tested.

To supply power to the platinum heater elements on the heat pipe, a regulated DC power supply with voltage and current limiting was used. The power supply had a 3A and 60 Volt capability which was adequate for the experiments. Two digital multimeters were used to determine the voltage and the current used by the heaters. The multimeters have a listed uncertainty of 0.5% by the manufacturer. Voltage was measured directly across the outputs of the power supply and was read in Volts to two decimal places. Current was measured by measuring the voltage drop across a 1% precision shunt, which was calibrated for 50 mV for 50 A. The readings were measured in millivolts with one decimal place. Power (P) was calculated using the measured voltage (V) and current (I) drawn by the heater(s) by the relation $P=VI$.

When a single heater was employed, the lead wires for the heater were attached to the power supply and to the precision shunt. Hence, the total resistance of the circuit would include the heater, the lead wires, the precision shunt, and the a short jumper wire. The resistance of all these elements without the heater was measured and found to be no greater than 0.1 ohm in any case. Considering that the nominal heater resistance was from 9 to 12 ohms, the power dissipated in the circuit except at the heater

would be less than 1%, which can be considered negligible and that the calculated power can be considered to be completely dissipated in the heater element on the heat pipe's surface.

In the case where multiple heaters were used, the heaters were hooked up in series. Hence, the power dissipated in each heater individually could not be determined. With the total power dissipated known, the average power dissipated by each heater could be estimated. However, care would need to be taken using this procedure since the resistance of the heater element is very sensitive to temperature. Thus, with a temperature variation existing across the surface of the substrate, each of the heaters in the series configuration may have slightly different resistance, and therefore, a different amount of power being dissipated.

Data acquisition will consist of a set of thermocouples bonded directly to the surface of the heat pipe (substrate). Type K thermocouples were chosen and were bonded to the square platinum pads between the heaters on the substrate's surface. Additional thermocouples were placed at other positions on the substrate as appropriate. Actual thermocouple locations on each heat pipe tested is given later in this chapter. All thermocouples were bonded to the ceramic surface using thermally conductive epoxy (Omega Engineering Inc., OV-100). The thermocouples were connected to a personal computer based data acquisition system consisting of a CIO-EXP32 multiplexer card and a CIO-DAS802/16 data acquisition card (both from

Omega Engineering Inc). The CIO-DAS802/16 card is a high precision eight channel card, hence, in order to collect more data, the multiplexer card is required. Following the manufacturer's calibration procedures [Omega Engineering, 1999], the uncertainty introduced by the data acquisition card on temperature measurements is published to be ± 0.1 °C. This can be considered an elemental uncertainty which needs to be added to the other uncertainties involved in the total temperature measurement.

The thermocouples were checked prior to bonding for accuracy and precision by immersing them in a water bath on a hot plate and checking the temperature against a mercury-glass thermometer which has a NIST traceable uncertainty of ± 0.2 °C. The temperature of the water was varied from approximately 0 °C (ice bath) to just under 100 °C in 10-15 °C increments. The water was stirred between temperature levels and the thermocouples were tapped and to dislodge any air bubbles in the group. All thermocouples were found to as a group to have a precision of ± 0.12 °C.

Uncertainty Analysis

An uncertainty analysis can be performed for the instrumentation used in the experimental set-up. For each measured parameter, one or more elemental uncertainties can contribute to the total uncertainty for the parameter. These elemental uncertainties were combined using the following Root-Mean-Squared (RMS) rule:

$$\mathbf{w} = \sqrt{\mathbf{v}_1^2 + \mathbf{v}_2^2 + \dots + \mathbf{v}_n^2} \quad (5.1)$$

The uncertainty of each measured parameter causes error in all calculated parameters. The propagation of error for 'n' calculated parameters, X_i in a particular objective function, R , can be determined using the Root-Sum-Squares (RSS) uncertainty method:

$$U_{RSS} = \sqrt{\sum_{i=1}^n \left(w_i \frac{\partial R}{\partial x_i} \right)^2} \quad (5.2)$$

which ω represents the total uncertainty for each variable X_i in the objective function R [Kline and McClinton, 1953]. Alternatively, the maximum propagated error can be found using:

$$U_{MAX} = \sum_{i=1}^n \left| w_i \frac{\partial R}{\partial x_i} \right| \quad (5.3)$$

which perturbs each measured parameter by its uncertainty and sums all of the perturbations for a worst-case scenario.

For the measured voltage and current, the results for the elemental uncertainties are summarized in Table 5-1. Nominal values of 20 V and 1.5 A were chosen as these were representative of the largest experimental values. As shown in the table, the total uncertainty for the voltage was ± 0.1 V and for the current was ± 0.05 A. Both of these values was dominated by the fluctuation in the measured value. As shown in the table, the RSS uncertainty of the power dissipated at the heater was found to be ± 1.1 W at 30 W, which is 3.4% of the dissipated power.

	Voltage (V)	Current (A)
Nominal Value	20.0	1.5
Instrument Uncertainty	± 0.10	$\pm 0.0075 + \pm 0.015$
Readout Fluctuation	± 0.005	± 0.05
Total Elemental Uncertainty	± 0.10	± 0.05
	U_{MAX} (W)	U_{RSS} (W)
Heater Power	$\pm 3.8\%$	$\pm 3.4\%$

Table 5-1. Summary of elemental uncertainties for measured voltage and current and the propagated error in the heater power calculation.

In a similar fashion, the uncertainty of the measured temperature was determined using the following elemental uncertainties: ± 0.1 °C within the data acquisition card, ± 0.2 °C for the thermocouple calibration, and ± 0.12 °C for measurement fluctuations. Hence the total elemental uncertainty for temperature measurements was estimated at ± 0.25 °C.

The uncertainty of the temperature has its most impact in the calculation of any thermal resistance since two temperature values are used. A empirically determined thermal resistance is defined as $R = \Delta T / Q = (T_1 - T_2) / Q$. The propagation of error in this calculation was determined using Equation 5.2, and was found to be very high, over 3 °C. However, closer examination found that this method was too sensitive to magnitudes of the temperatures used in the calculations and did not provide uniform results over a reasonable range of temperatures. Hence, Equation 5.2 over estimates the uncertainty. An alternative technique was used whereby each parameter

is perturbed by its uncertainty separately. Then the differences between the perturbed and unperturbed values are squared, summed and the square root is taken. This method is described by Equation 5.3. Using this method, the uncertainty for the thermal resistance was found to be 0.21 °C.

$$U_{per} = \sqrt{\sum_{i=1}^n [R(x_i + w_i) - R(x_i)]^2} \quad (5.3)$$

The primary driver for this uncertainty is the uncertainty in the temperature difference, which becomes significant (>10%) when the temperature difference is relatively small. Additionally, it should be noted that the uncertainty for the transferred heat is based on the uncertainty of the power dissipated at the heater, hence, this would assume all of the heat dissipated is being transferred without any losses. In reality, heat will always be loss to ambient conditions and other heat sinks. The issue of ambient heat loss will be discussed later in the experimental data discussion. However, the uncertainty calculated here would represent the minimum uncertainty that would occur solely due to instrumentation.

Experimental Procedures

In all the thermal performance tests, the thermal load was adjusted over a range from 2 to about 27 Watts, usually in approximately 2 W increments. At any one power level setting, the power was set and then the heat pipe was allowed to reach steady state conditions. Steady state conditions were defined as the state when temperature at all the

thermocouple locations did not change with time, more specifically that the temperature did not change in a steady perceivable direction (up or down). In some cases, the temperature may have oscillated between two values due to the resolution of the data acquisition system. Once a change was made in the thermal load, steady state was typically achieved within a few minutes, however, a period of at least twenty minutes was given prior to any data being recorded.

It was the desire to try to ascertain the capillary limit of the heat pipes so data would be collected at increasing power levels until it was apparent that dry-out had occurred marked by a sharp non-linear temperature rise near the heater location. However, due to increased local heating near the heater due to conduction through the shell material, it was found to be difficult to really assess the temperature distributions during the experiment, i.e. the assessment could only be made post-experiment during the data reduction. Coupled with this difficulty was the fear of inducing thermal shock failure or heater burn-out at conditions at high power levels. Hence, the power level was increased until the maximum temperature at any of the thermocouple positions exceeded 90 °C. This temperature was chosen mainly because the other heat pipes experienced heater and mechanical failure at temperatures above 100 °C.

Heat Pipe Samples Tested

The dimensions of the sample heat pipes are given in Table 5-2 and 5-3. In Table 5-2, the type of wick structure is given for each heat pipe tested, the target charge volume of working fluid, and the outer dimensions of the sample. Additionally, the length of the sample which was clamped on to the cold-plate is indicated (as the condenser length, L_c). The location of the heaters on each of the samples is given in Table 5-4. Since the heaters were screen printed on to the samples, the distance between heaters will be the same for all samples, but the global placement of the heater patterns relative to the evaporator end-cap may have some offset from sample to sample. Lastly, the location of the thermocouples along heat pipe is given in Table 5-5.

Heat Pipe	Wick Type	Charge (μL)	L (mm)	L_c (mm)	W (mm)	H (mm)
7	Top-Bottom	80	81	25	12.2	2.9
8	Top-Bottom	80	81	26	9.6	2.9
9	Side-Wall	80	81	25	9.7	3.4
10	Side-Wall	50	81	23	12	3.4

Table 5-2. Overall dimensions of heat pipe samples.

Heat Pipe	D _g (mm)	w _g (mm)	s _g (mm)	t _v (mm)	w _v (mm)	N _g	H _{cap} (mm)	Q _{cap} (W)
7 / 8	0.16	0.16	0.43	1.4	4.5	14	38	20
9 / 10	0.50	0.16	0.32	4.2	2.0	8	38	62

Table 5-3. Wick dimensions of the of heat pipe samples.

Two samples (HP#7 and HP#9) were cross sectioned so that the details of the wick structures could be evaluated as shown by the micrographs (captured on a JEOL Scanning Electron Microscope) in Figures 5-1 and 5-2. Using these micrographs, the dimensions of the wick details was obtained and are to be considered representative of the wick structures in the other samples.

As should be evident in the photos, the wicks were not of high uniformity but the photos should be representative of the wick dimensions of the other heat pipes fabricated in the set. Much of the non-uniformity of the wick structure is due to poor fabrication methods, which have significantly improved by the time this dissertation was written and continued to be improved with the on-going research in this field. However, the quality of the internal wicks used in this study was adequate to meet the objectives of the research which was to show feasibility and provide baseline performance data for this new technology.

For both types of wick structures, the other samples in the fabrication set were cut-up to evaluate the wick structure along the length of the heat pipe. Some samples were cut axially along the heat pipe's centerline to allow for visual inspection of the liquid transport at various orientations. It was found that liquid could easily flow along the entire length of the wick structures (without flooding the wick) in the horizontal orientation.

Heater Location	Distance from evaporator end cap. (mm)			
	HP#7	HP#8	HP#9	HP#10
H1	20	20	18	18
H2	30	30	28	28
H3	40	40	38	38
H4	50	50	48	48

Table 5-4. Heater locations on the heat pipe samples.

T/C	Distance from evaporator end cap. (mm)			
	HP#7	HP#8	HP#9	HP#10
1	4	15	13	13
2	15	25	23	23
3	25	35	33	33
4	35	45	43	43
5	45	55	53	53
6	55	65	63	63
7	65	75	73	73
8	75	n/a	n/a	n/a

Table 5-5. Thermocouple (T/C) locations on the heat pipe samples..

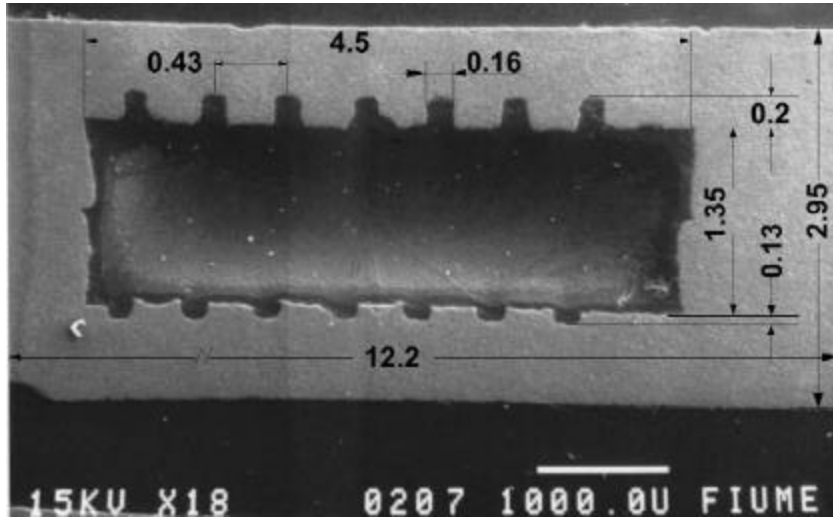


Figure 5-1. Cross-section of HP#7 showing internal geometry for top/bottom grooved wick heat pipe samples. Dimensions shown are in millimeters.

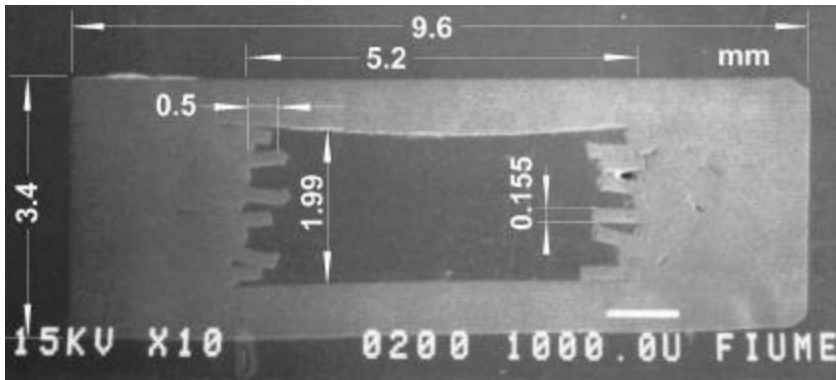


Figure 5-2. Cross-section of HP#9 showing internal geometry for side wall grooved wick heat pipe samples. Dimensions shown are in millimeters.

VI. Thermal Performance Testing

Overview of Testing

Comparative thermal performance data was obtained for four HTCC heat pipes, two with Top/Bottom grooved wicks, and the other two with Side Wall grooved wicks. As discussed in Chapter 3, the heater failure which led to the mechanical failure of HP#7, 8, and 9, did not allow for a comprehensive data set to be obtained. However, HP#10, operated reliably with repeatable results throughout a daily testing regime for three months. This allowed for a significant amount of data to be collected which, allows for many comparisons to be made. A summary of the experimental matrix obtained is given in Figure 6-1 and is discussed as follows:

Single Heater Operation: All heat pipes were tested using the (H1) heater that was the furthest from the condenser region. Additionally, HP#10 was tested for a single heater operating in one of three heater positions (H1, H2, and H3) along the heat pipe. Refer to Table 5-4 for the location of the heaters on each sample.

Multiple Heater Operation: Only HP#10 was tested with four multiple heater configurations with 1, 2, 3, and 4 heaters operating simultaneously. Heater designations are assigned using the following convention: H1, Heater H1 only; H12, Heaters H1 and H2 together; H123, Heaters H1, H2, and H3 together; H1234, Heaters H1, H2, H3, and H4 together.

Operational Configuration	Number of Samples (Thermal Load Range)			
	HP#7	HP#8	HP#9	HP#10
Single Heater	All orientations included in number of samples.			
H1	28 (2-27W)	6 (2-19W)	6 (5-22W)	39 (2-18W)
H2				23 (2-12W)
H3				14 (4-10W)
Multiple Heater	All orientations included in number of samples.			
H12				37(2-16W)
H123				28 (2-16W)
H1234				34 (2-18W)
Axial Orientation	All heater configurations included in number of samples.			
0°	9 (4-15W)		6 (5-22W)	47 (2-18W)
30°	7 (3-23W)			39 (2-18W)
45°	4 (2-20W)			41 (2-18W)
90°	8 (3-27W)	6 (2-19W)		42 (2-18W)
Transverse Orientation	All data is Heater Side Down unless specified otherwise.			
Heater Side Up				7 (4-12W)
Heater Side Vertical				3 (3-12W)
Uncharged Testing	4 (2-6W)			3 (2-5W)

Table 6-1. Summary of experimental configurations. Blank indicates no data available for that configuration.

Axial Orientation: Data were collected at 0°, 30°, 45° and 90° relative to the horizontal (evaporator lower than condenser) for heat pipes HP#7 and HP#10. HP#8 was tested in the vertical orientation and HP#9 was tested in the horizontal orientation.

Transverse Orientation: HP#10 was tested in three transverse orientations with the heater substrate side up (heater on the top side and cold-plate on the bottom), down (heater side on the bottom and the cold-plate on the top), and vertical (top and bottom side of the substrate being vertical). In all cases, the axial orientation of the heat pipe was horizontal ($\theta = 0^\circ$).

Varying Thermal Loads: Various thermal loads were taken starting from 2 W and extending to greater than 18 W, so that any non-linear effects due to the thermal load could be determined.

Wick Configuration: Data is available to allow for a comparison of the Top/Bottom (HP#7 and 8) and Side-Wall (HP#9 and 10) wick structures.

Uncharged Mode: HP#7 and HP#10 were tested uncharged (i.e. no working fluid) to provide a comparison between the conduction only heat transfer mode and when the heat pipe is charged.

Comparison of Charged and Uncharged Samples

The most dramatic evaluation of the effect of the heat pipe to the substrate is to compare two samples with similar overall dimensions, one with an embedded heat pipe and the other being solid ceramic. An alternative is to test a substrate sample with its embedded heat pipe charged

and uncharged which provides a direct evaluation of what the addition of the working fluid does to the same substrate. It is prudent to note that the uncharged sample has less cross-sectional area than it would if it were a truly solid substrate sample. For the samples tested, the heat pipes accounted for 21 to 30% of the cross-sectional area of the sample.

Data for two samples was obtained for uncharged operation and is shown in Figure 6-1. With the sample uncharged, data was obtained at a few thermal loads. Also shown in the figure is data for the same heat pipe operating when charged at approximately 10 W thermal load. In all cases, the heat pipe was mounted in the fully insulated test cell attached to the cold-plate as discussed previously. For HP#7, heater H1 ($x = 20$ mm) was used and for heat pipe HP#10, heater H2 ($x = 18$ mm) was used. Unfortunately, during the preliminary uncharged testing of HP#10 (to check the instruments and wiring), heater H1 was used and failure occurred in the heater at the solder pads to the lead wires. It was also noted that the insulation was browned due to the high temperatures reached when running the samples uncharged. Hence, heater H2 ($x = 28$ mm) was used for the remainder of the testing. Consequently, during the testing using heater H2, the thermocouple at $x = 23$ mm was showing over 30 °C lower than expected. Later inspection revealed that the thermocouple detached during the testing which appear to be due to thermal failure of the epoxy. Hence, its data was removed from the set shown in Figure 6-1.

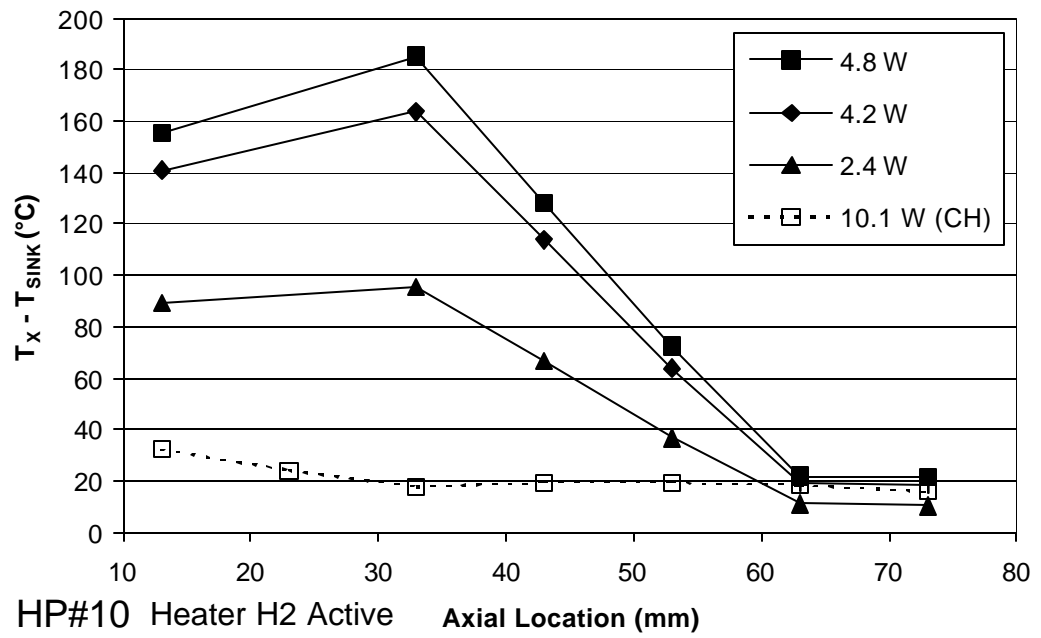
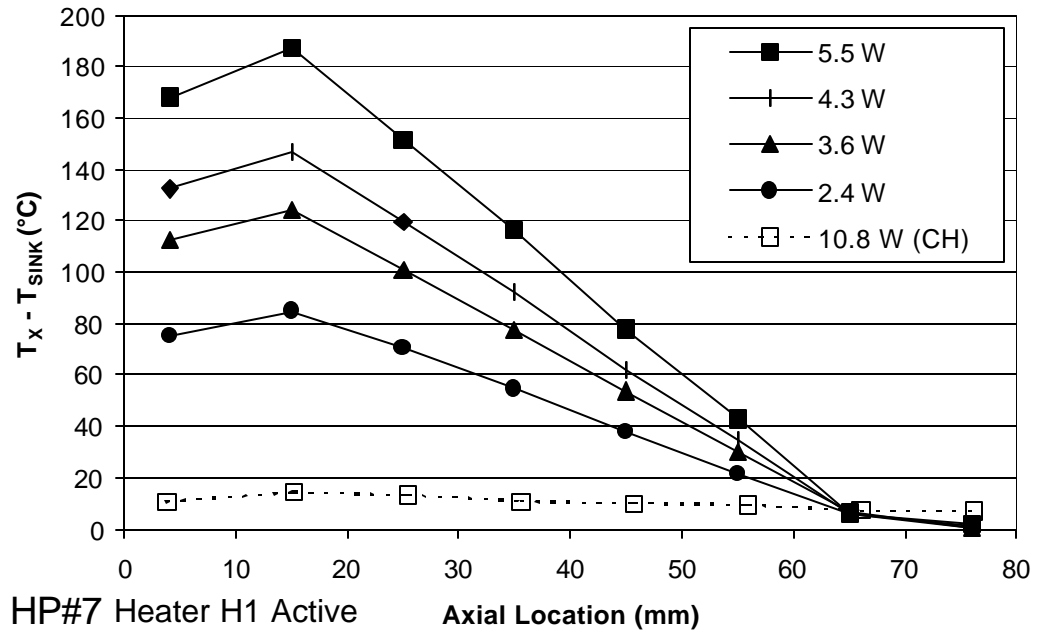


Figure 6-1. Conduction mode (uncharged) operation of samples HP#7 and HP#10 at various power levels. A representative comparison is provided for each sample operating with a liquid charge (CH) at 0° axial orientation. Vertical axis has been normalized using the sink temperature.

Trends common to both HP#7 and HP#10 in Figure 6-1 are the two nearly linear portions of the temperature distribution on the left and right hand side of the heater location. On the right side of the heater location the heat is transferred through the ceramic material to the cold-plate acting as a heat sink, and along this path some heat is loss to the ambient through the insulation. On the left of the heater location, the heat must be transferred to the end of the ceramic material and then through the insulation to the ambient. On the right side the ceramic material is acting like a extended surface, for which the temperature distribution is typically logarithmic due to the competition of the heat conducting through the material and that being continual loss to the ambient. However, the slope of the curves on the right side of the heater location are nearly linear, indicating that the insulation is adequate enough to make losses to the ambient very small.

Using one-dimensional heat conduction theory, the thermal resistance of the insulation can be calculated using the material properties of typical glass-wool insulation. In a similar fashion, the thermal resistance through the ceramic material can also be determined. For the purpose of evaluation, the left-side and right-side slopes of the curves shown can be used to obtain a thermal resistance of the two thermal paths described. For the purposes of this conservative evaluation, the maximum temperature difference is divided by the total heat dissipated, noting that in reality there is a component of the total heat transferred through each path. Using this method, it was found

that thermal resistance was somewhat insensitive to the thermal load and thus an average was obtained for the right-hand side curves. Finally, for the charged data shown in the figure, the maximum temperature difference along the heat pipe can be divided by the thermal load. All these thermal resistances were calculated and shown in Table 6-2.

Thermal Path Description	Thermal Resistance (°C/W)	
	HP#7	HP#10
Conduction through ceramic only	59.5	42.6
Average for left hand side	3.5	4.8
Average for right hand side	30.5	34.6
Insulation blanket	150	150
Charged Heat Pipe	0.47	1.64

Table 6-2. Comparison of thermal resistance for various paths through the substrate and the insulation blanket during uncharged heat pipe testing.

One possible way to get an estimate of the thermal losses to the ambient would be to look at the ratio of the left-hand and right-hand thermal resistances shown in Table 6-2. This method gives an estimate of the thermal loss to be 11% for HP#7 and 14% for HP#10. Another approach which is more robust is to consider the conduction heat transferred through the ceramic material on the right-hand side only, that is, from the heater location to the heat sink. The heat entering near the heater location must equal to the heat leaving at the heat sink plus the heat loss along the path to

the ambient through the insulation. Applying Fourier's Law of Conduction and the conservation of energy for this section of ceramic material,

$$Q = kA_C \frac{dT}{dx} \quad Q_{in} = Q_{out} + Q_{Loss} \quad (6.1)$$

it can be shown that,

$$\% \text{ Ambient Heat Loss} = \frac{Q_{Loss}}{Q_{in}} = 1 - \frac{dT/dx|_{Loss}}{dT/dx|_{in}} \quad (6.2)$$

The curves on the right side of the heater location in Figure 6-2, do appear essentially linear, however, there is a small amount of curvature present with a slope change from the heater location to the heat sink location. The local slope of the curves near the heater was determined using the thermocouples at $x = 15$ and 25 mm for HP#7 and $x = 33$ and 43 mm for HP#10. Similarly, the local slope of the curve was determined near the heat sink using the thermocouples at $x = 55$ and 65 mm for HP#7 and $x = 53$ and 63 mm for HP#10. The values for the local slopes for both heat pipe samples are summarized in Table 6-3. From the table it can be seen that the ambient loss of heat was about 7% for HP#7 and about 11% for HP#10. The variation in the ambient loss is very consistent for all of the thermal loads for each heat pipe. However, between the two samples, there is a variation which should be due to an experimental uncertainty such as the variation in the wrapping of the insulation blanket around the sample. For the ambient loss calculation itself, the uncertainty of the temperature measurements was propagated

through the calculation and was found to give a propagated RSS uncertainty of $\pm 4.6\%$.

Heat Pipe	Thermal Load (W)	$(dT/dX)_{in}$ ($^{\circ}C/mm$)	$(dT/dX)_{in}$ ($^{\circ}C/mm$)	Ambient Loss
HP#7	5.5	3.63	3.38	6.9%
	4.3	2.84	2.67	6.0%
	3.6	2.33	2.33	7.7%
	2.4	1.69	1.69	7.1%
HP#10	4.8	5.71	5.05	12%
	4.2	4.98	4.45	11%
	2.4	2.89	2.57	11%

Table 6-3. Summary of calculations for estimating the ambient heat loss using the conservation of energy through the ceramic from the heater to the heat sink.

Overall Thermal Performance

The overall thermal performance of the heat pipes tested can be shown clearly by plotting the temperature rise across the heat pipe as a function of thermal load. This is shown for the heat pipes with the Top/Bottom wick structure (HP#7 and HP#8) shown in Figure 6-3, and for the heat pipes with the Side-Wall wick structure (HP#9 and HP#10) in Figure 6-4. To allow for a ready comparison between the four samples, the vertical axis in the figures uses the average evaporator region temperature minus the average condenser region temperature. For the purposes of this discussion, the average temperature for the evaporator region was determined by averaging the temperatures from thermocouples on each side of a heater location. Likewise, the average condenser region temperature was determined by

averaging the temperature from the two thermocouples that were at axial locations located over the portion of the heat pipe that was mounted on the old-plate. Keep in mind that all the thermocouples were bonded to the same side of the substrate as the heater elements. The horizontal axis in the figure represents the thermal load or the calculated dissipated power at the heater location. In both Figure 6-3 and 6-4, the thermal load was provided by heater H1, and for HP#7 and HP#10, data is shown for multiple orientations. For HP#8, data was only available for the vertical orientation with the evaporator region being lower than the condenser region. Lastly, for HP#9, data was only available for the horizontal orientation.

For both figures, the data follows a linear trend with the correlation coefficients being 0.84 or higher. A linear trend is expected as the major contributor to the overall thermal resistance of the heat pipe is the shell material at the heater and the cold-plate locations. Since this thermal resistance is a result of the conduction through the ceramic material, it is constant regardless of the thermal load, assuming that the thermal path to the working fluid is relatively constant in length and cross-sectional area. Hence, the slope of the curves shown in Figures 6-3 and 6-4 represent the average thermal resistance of the heat pipe system from the heat source to the heat sink. The slopes of the fitted lines in the two figures give an overall thermal resistance from 0.55 °C/W (for HP#7) to 2.42 °C/W (for HP#9).

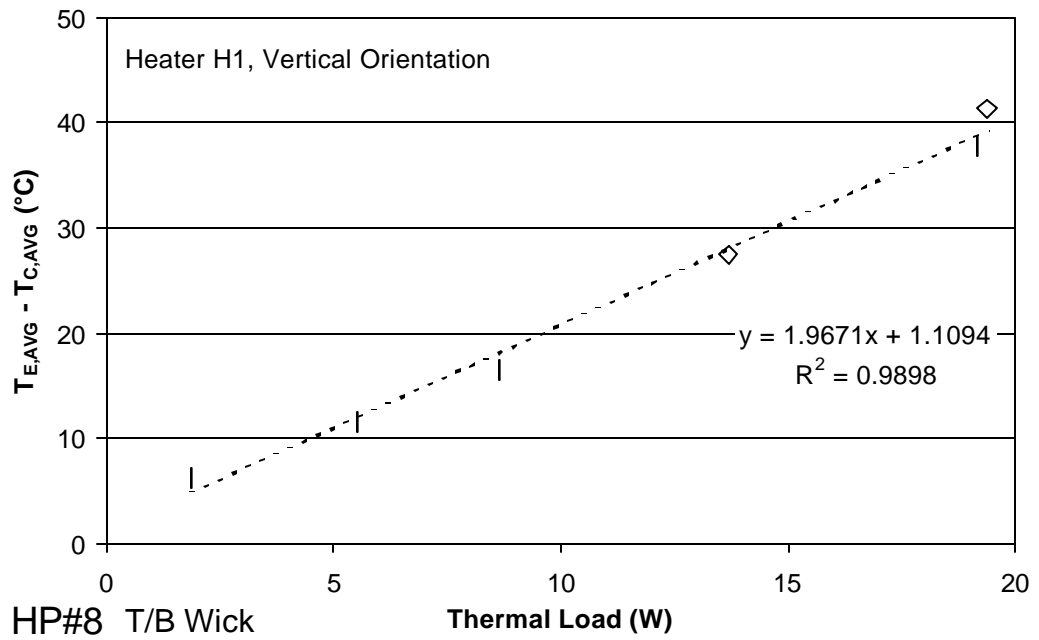
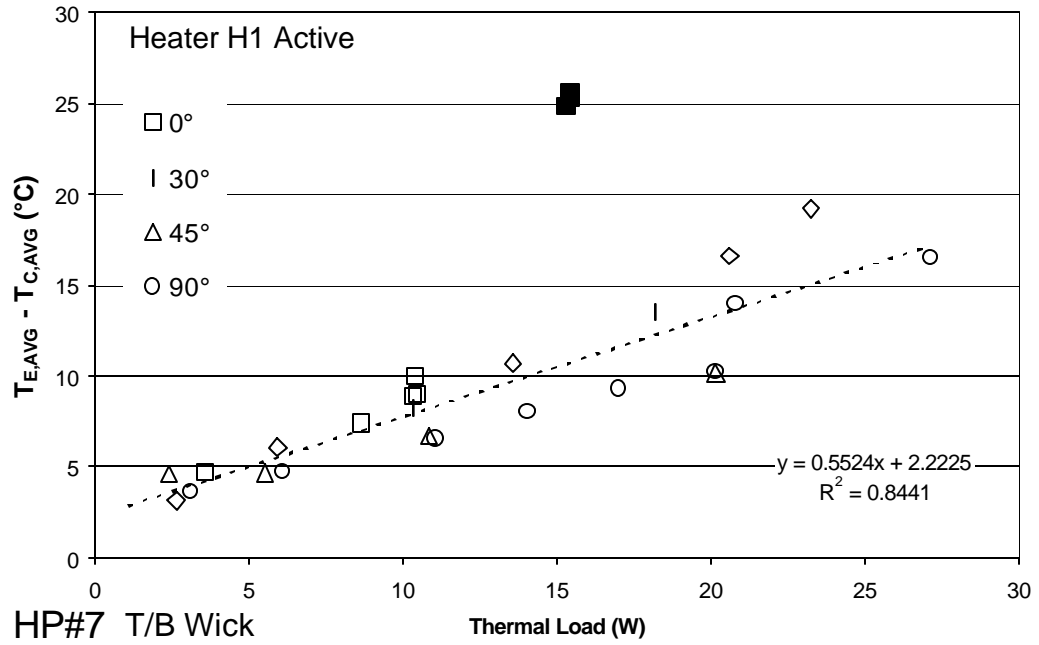


Figure 6-3. Average temperature rise at the evaporator region over the sink temperature for heat pipe samples which had Top-Bottom wick structure.

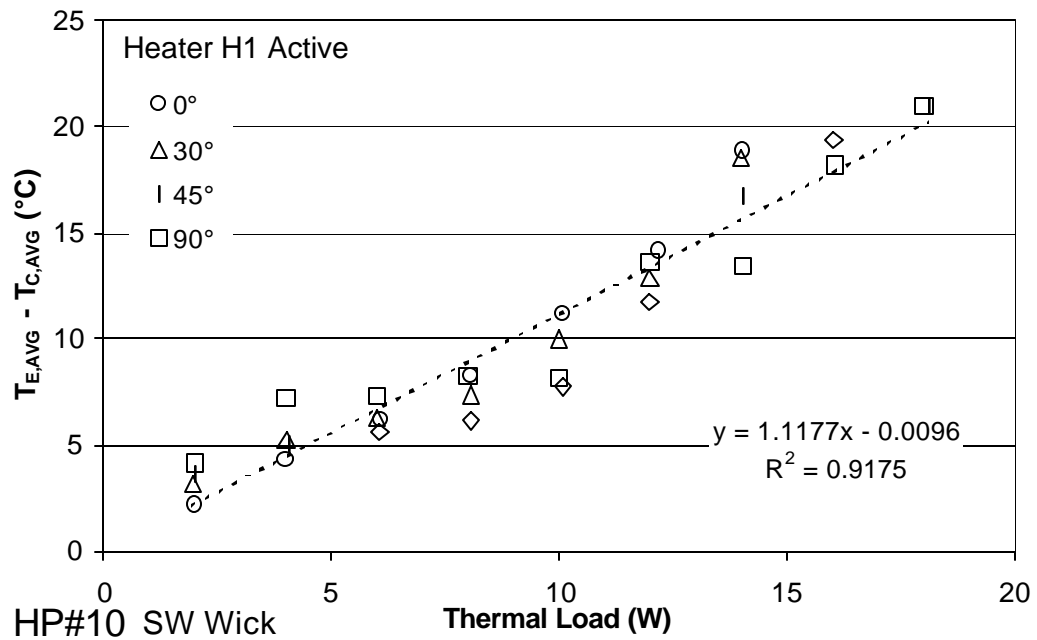
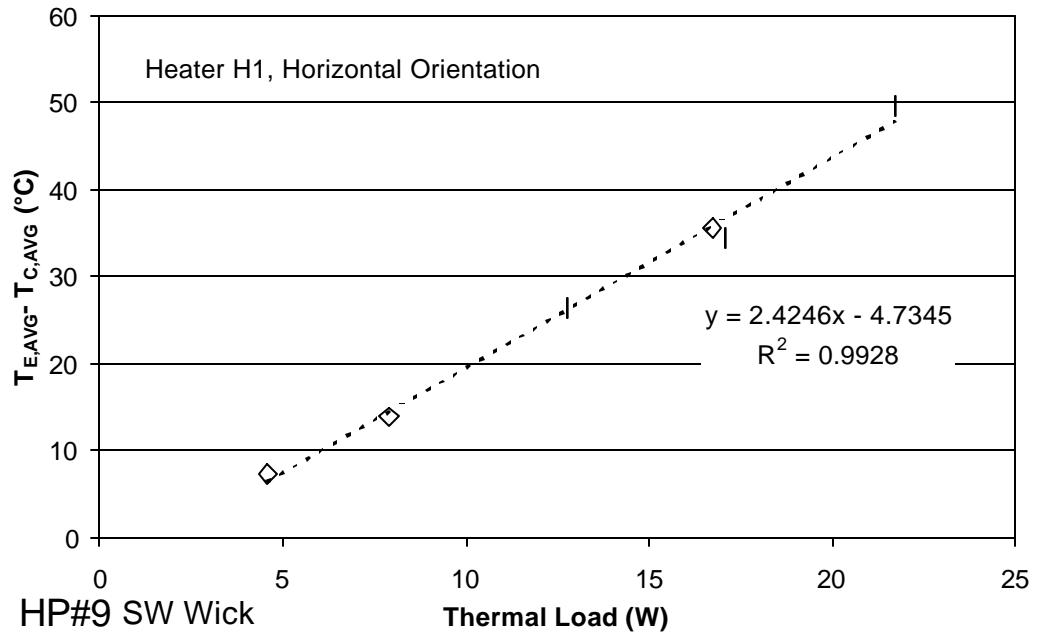


Figure 6-4. Average temperature rise for the evaporator region over the sink temperature for heat pipe samples which had Side-Wall wick structure.

A significant anomaly appears in Figure 6-3 for HP#7. Three data points depart from the linear trend at a thermal load of about 15 W. All three of these points are for the horizontal orientation ($\theta = 0^\circ$) and for a thermal loads of 15.2, 15.4 and 15.4 W. During the experiment it was noted that when the thermal load was increased from 12 to 15 W, a non-linear temperature rise occurred. To verify if this anomaly was repeatable, the thermal load was decreased back to 12 W, whereby the temperatures returned to the previous values. Then upon increasing the thermal load again to about 15 W, the same elevated temperatures were obtained. This anomaly was repeated consistently three times, and is most likely attributed to a localized dry-out condition in the upper wick of the heat pipe (the wick along the heater side of the substrate). With the wick not wetted by the working fluid, the heat dissipated by the heater would have to travel further in both the axial and z-axis directions to wetted regions of the top and bottom wicks.

Upon closer examination of the data for HP#7 in Figure 6-3, it may be inferred that the data points for $\theta = 30^\circ$ may also depart from the linear trend starting at a thermal load of about 18 W. This response would make sense as the slight downward tilt of the heat pipe would now provide some additional pumping force for returning the working fluid to the heater location. Considering only the data at $\theta = 30^\circ$ only, a regression analysis for these data points indicates that the standard error for a linear trend is ± 0.7 °C, with a

95% confidence interval of is ± 1.5 °C. These statistics give a measure of the scatter in the data relative to the linear trend generated from the data. Unfortunately, the magnitude of the departure is just a little larger than the scatter in the data set. Hence, it is difficult to assess whether the departure is in fact, a physical trend or if it is just normal scatter in the experimental data.

From Figures 6-3 and 6-4, there does not appear to be any indication that there is a significant difference between the heat pipes with the Side-Wall or the Top/Bottom wick structures. However, it can be noted that the lowest overall system thermal resistance is found for HP#7 (with a Top/Bottom wick) and the highest thermal resistance is found for HP#9 (with a Side-Wall wick). The data for HP#7 and HP#10 include data for multiple axial orientations and the grouping of the data in the figures appear to have a random grouping along the fitted linear trend. Hence, the data does not show a clear correlation between the axial orientation and the thermal performance. The issue of axial orientation will be covered again in more detail for HP#10 later in this section.

The next set of figures which are highly representative of the overall thermal performance are Figures 6-5 and 6-6, which show the axial temperature distribution for HP#7 and HP#10 for both the vertical and horizontal orientations and at several thermal loads. For the purposes of comparison between these figures, the temperature has been modified by

subtracting the temperature of the cold-plate (i.e. the heat sink reference temperature).

In both figures, the temperature distribution is relatively uniform from the condenser through the adiabatic region, with a sharp temperature rise in the vicinity of the heater. Considering the temperatures distribution in the condenser and adiabatic regions first, the figures show that in general, the temperature distribution for particular orientation and heat pipe, remains the same at all thermal loads except for a roughly linear translation upward with increased thermal load. This trend is expected as the thermal resistance of the shell material at the condenser will cause the condenser end-cap temperature to rise with thermal load. This drives the minimum temperature the heat pipe can attain, and hence, all the other temperatures rise accordingly.

Now, considering the temperature rise near the heater location, each of the figures appear to show a unique trend. As shown by the FEA modeling in Chapter 4, the thermal resistance of the shell material between the heater and the wick will cause a predictable and linear rise in temperature from the heater to the heat pipe. Furthermore, it was shown that conduction of heat in the axial direction with heat pipe will cause a localized temperature rise up to 1 cm on both sides of the heater location.

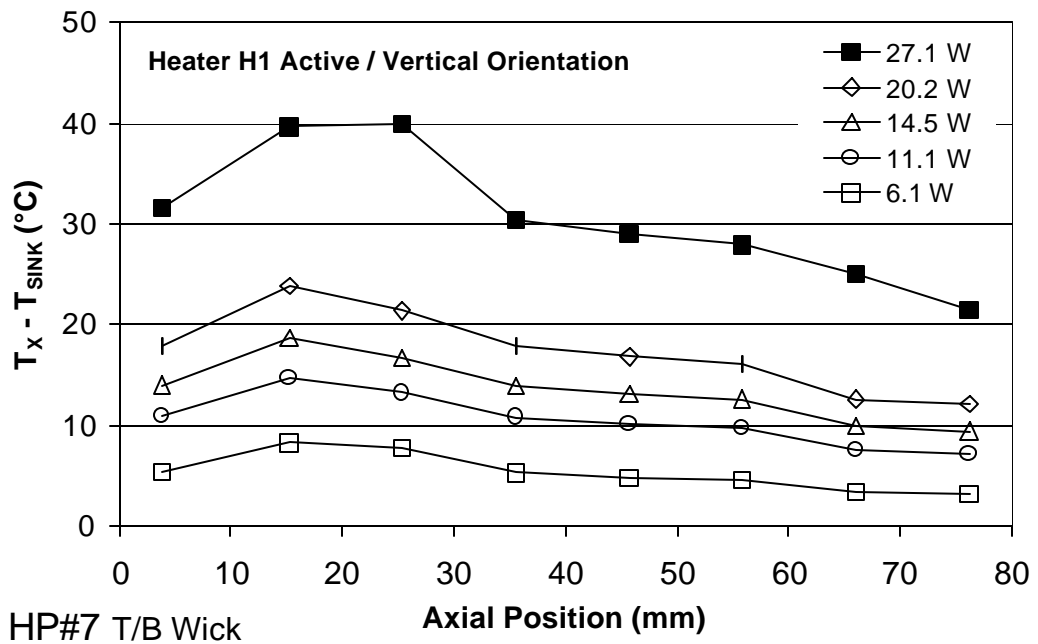
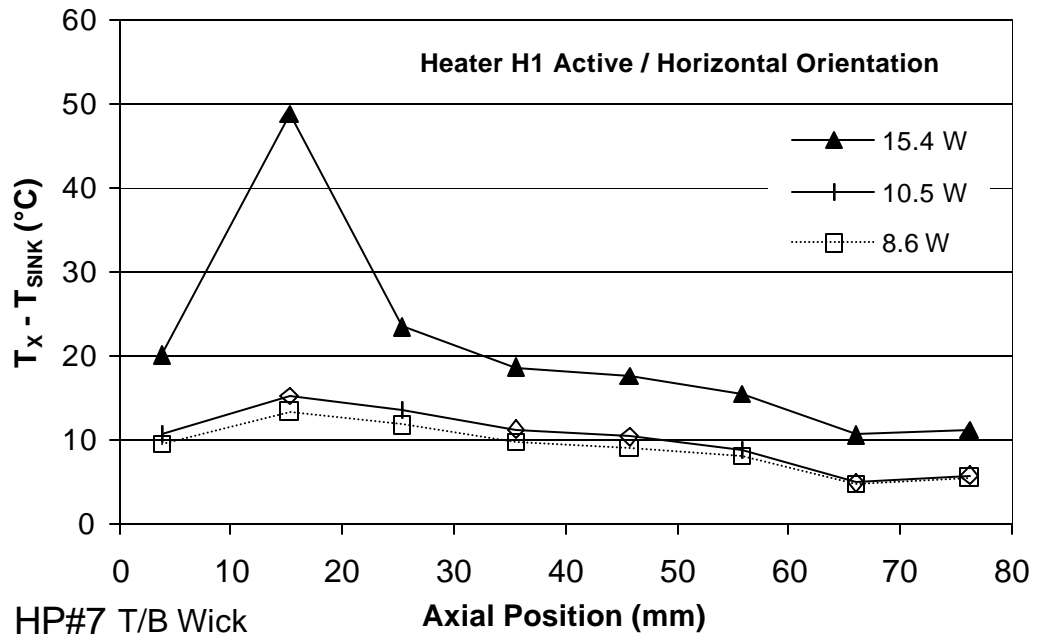


Figure 6-5. Temperature distribution for HP#7 with a Top/Bottom wick structure operating at various power levels in both horizontal and vertical (evaporator side down) orientations. Heater is located at $x = 20$ mm.

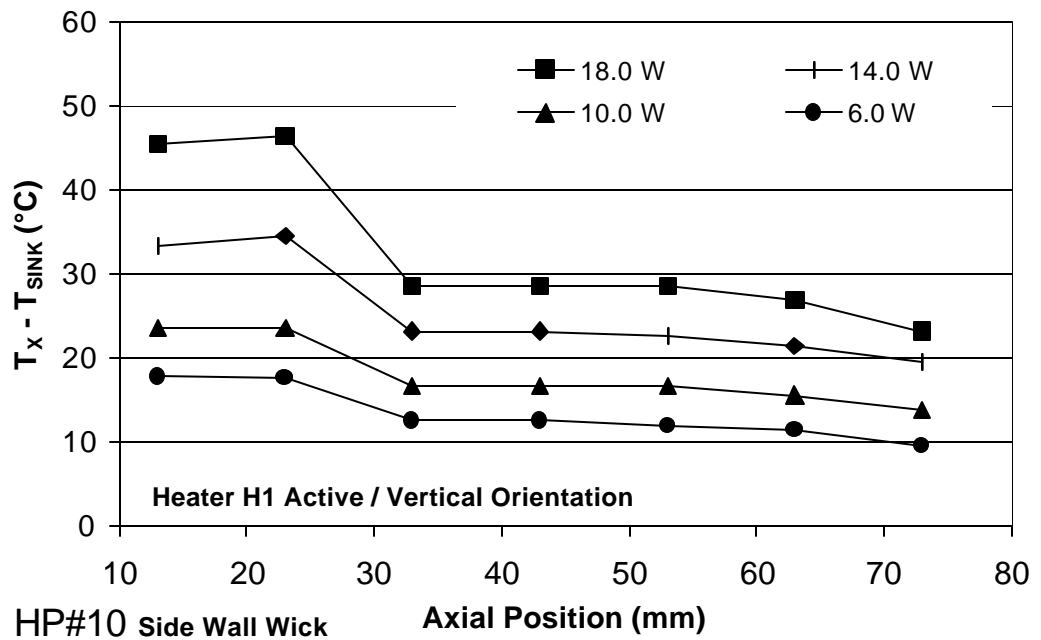
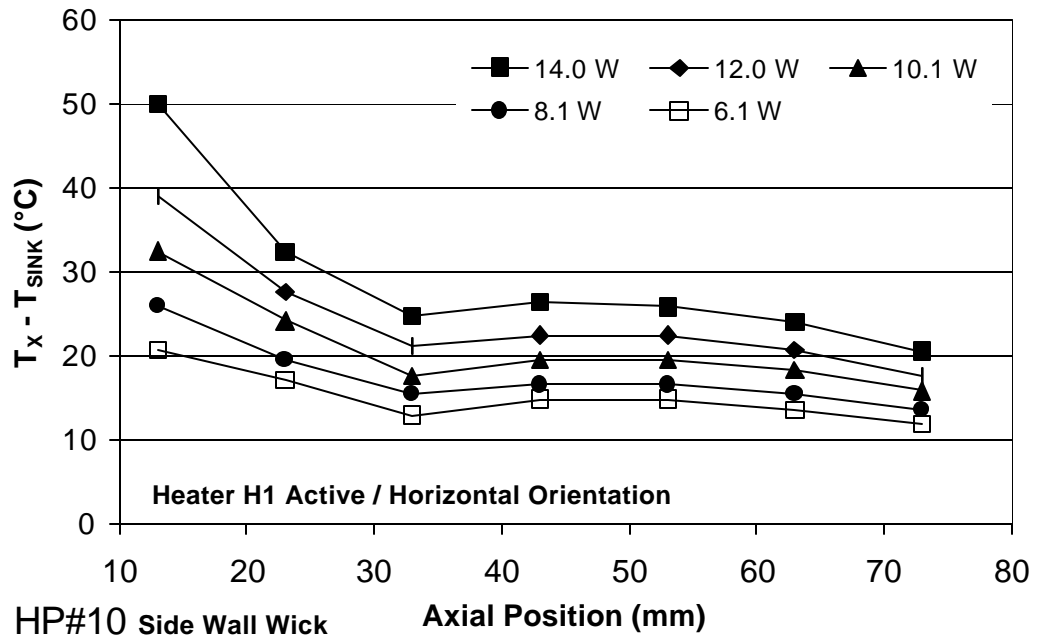


Figure 6-6. Temperature distribution for HP#10 with a Side-Wall wick structure operating at various power levels in both horizontal and vertical (evaporator side down) orientations. Heater is located at $x = 18$ mm.

Upon reviewing Figure 6-5, the most dramatic element is the sharp temperature spike seen for HP#7 in the horizontal orientation at 15.4 W thermal load. This data point corresponds to one of the three data points in Figure 6-3 that departed the linear trend. The almost 30 °C rise in temperature further supports that capillary dry-out must be occurring. Of interest is that the maximum temperature is found at $x = 15$ mm, which is closer to the evaporator end-cap, but then at $x = 4$ mm, there is a rapid temperature drop back to approximately 20 °C, which is close to the adiabatic region temperature. For this to occur, one or both of two things must be occurring: 1) vapor is present near the evaporator end-cap, driving the temperature of the ceramic to be near the adiabatic region temperature, and 2) localized dry-out is only occurring on the top wick and the bottom wick is still wet, bringing working fluid all the way to the evaporator end-cap. Heat is then being conducted to the wetted portions of the wick and evaporation is occurring, driving the ceramic material to the vapor temperature. A similar temperature rise is seen for HP#7 in the vertical orientation at a thermal load of 27.1 W, however, referring back to Figure 6-2 will show that the maximum temperature is still following a linear trend. Hence, the temperature distribution is expected and predictable.

When reviewing Figure 6-6 for HP#10, it is important to note the scale for the axial position. For HP#10, the first thermocouple position is located at $x = 13$ mm with the first heater (H1) being at $x = 18$ mm. Hence, when

comparing the temperature distribution with those shown for HP#7, note that there is an extra thermocouple between Heater H1 and the evaporator end-cap. Using this information, it should be apparent that the temperature distributions for HP#10 in the vertical orientation are very similar to those for HP#7 in the vertical orientation, albeit, the curves are translated up about 6 °C and the temperature rise near the heater is slightly more pronounced.

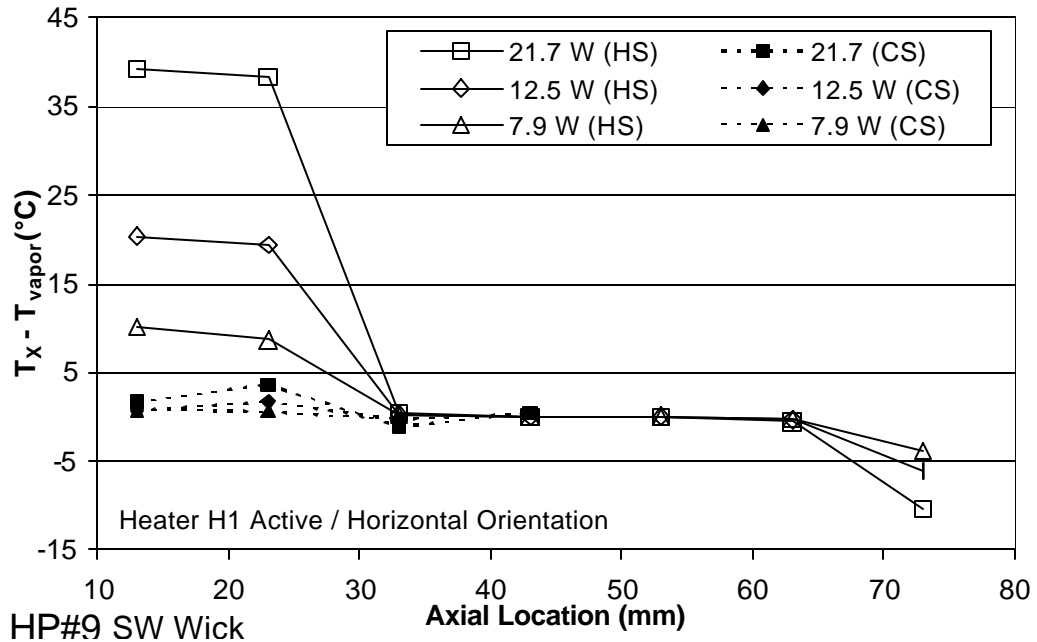


Figure 6-7. Comparison of temperature distributions on the heater side (HS) and the condenser side (CS) of the heat pipe for HP#9.

The last figure in this section is provided to show the temperature distribution on both sides of the heat pipe, that is the heater side (HS) and the condenser side (CS). This data was only available for HP#9 and is shown in Figure 6-7. In this figure the temperature has been modified by

subtracting the vapor temperature as determined by taking the average of the temperatures in the adiabatic region. The trends are clearly apparent in the figure. The temperatures along the condenser side of the substrate are within 3 °C of the temperature in the adiabatic region (i.e. the vapor temperature). The temperature along the heater and condenser sides of the substrate are essentially the same in the adiabatic region, being driven by the vapor temperature. The characteristic temperature rise near the heater is only seen on the heater side of the substrate. An important conclusion can be drawn from the data shown in Figure 6-7. If the wick was fully dried out in the end of the heat pipe (from the heater location to the evaporator end-cap), then the temperature of both sides of the heat pipe would have to be elevated. However, with the condenser side temperatures being constant along the entire length of the heat pipe, then there is a strong indication that the wick must be wetted, particularly along or near the condenser side for the entire length of the heat pipe, thus capillary dry-out is not strongly supported by the temperature rise near the heater, but rather it must be due to the conduction thermal resistance of the shell material.

Single Heater Operation

It was desired to investigate the effect of the heater's axial location on the heat pipe. The location of the heater will affect the effective length of the heat pipe, although the physical length of the heat pipe remains the same. In traditional operation, the evaporator and condenser regions are always at the

opposite ends of the heat pipe. However, for the purposes of electronic packaging, it may be useful to run a single heat pipe under several heat dissipating components, hence, some of the heat sources may be closer to the middle of the heat pipe. Additionally, there are potential applications where a heat pipe could have a single evaporator region near the center of the heat pipe with an active condenser region at the both end-caps.

Using HP#10 (Side-Wall wick), the temperature distribution for the heater configurations, H1, H2, and H3 are shown in Figures 6-8, 6-9, and 6-10, respectively. Temperature distributions are shown for both the horizontal and vertical orientations. The location of the heater from the evaporator end cap is given in the caption for each figure along with the temperature of the cold-plate.

The single heater configurations are indicated by the notation H1, H2, and H3. For the H1 configuration, heater 1 ($x = 18$ mm) was connected to the power supply, with the other heaters not powered. In a similar fashion, the H2 and H3 configurations, indicate that heaters 2 ($x = 28$ mm) or 3 ($x = 38$ mm) were operated as the heat source. By comparing the H1, H2, and H3 configurations, the thermal performance of the heat pipe can be assessed for a similar heat source operating at different locations along the length of the heat pipe with approximately the same heat flux at similar power levels.

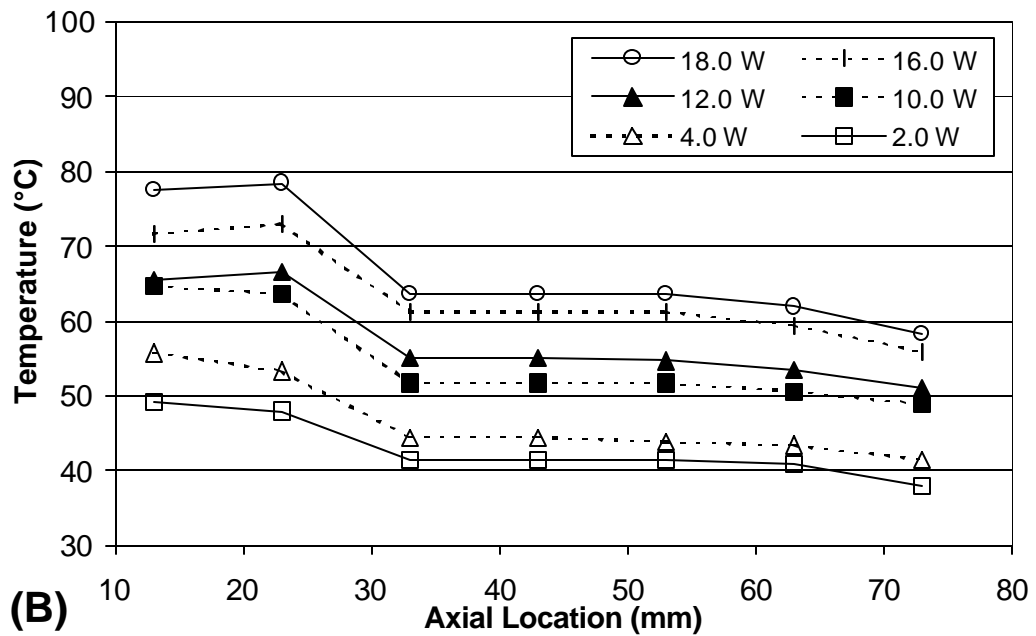
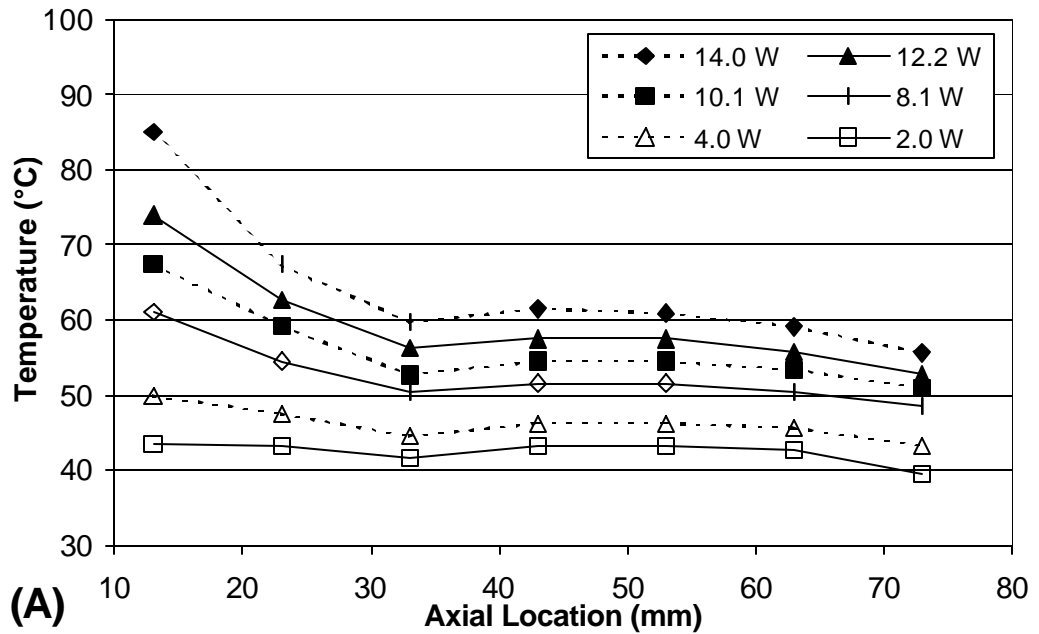
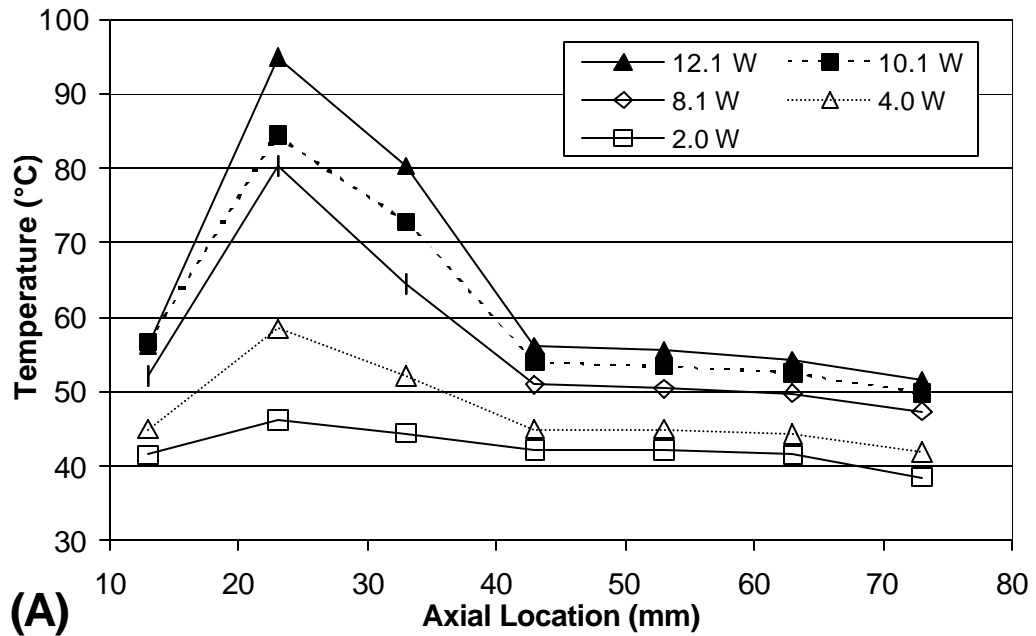
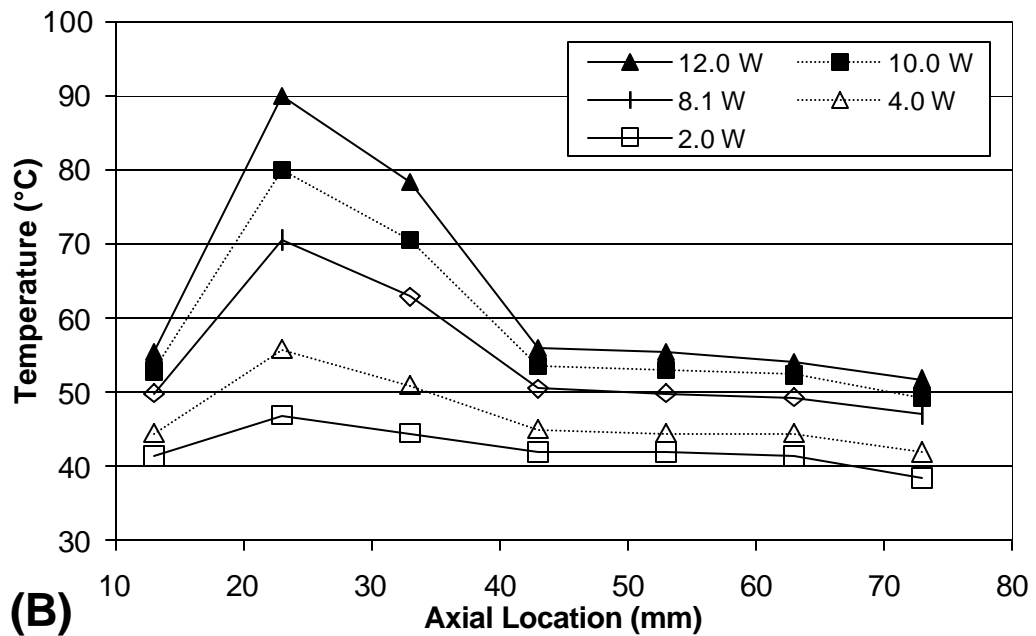


Figure 6-8. Temperature distribution along HP#10 for H1 configuration at various power levels for (A) 0° and (B) 90° axial orientation. Heater 1 is located at x=18mm and the sink temperature was 35 °C.



(A)



(B)

Figure 6-9. Temperature distribution along HP#10 for H2 configuration at various power levels for (A) 0° and (B) 90° axial orientation. Heater 2 is located at x=28mm and the sink temperature was 35 °C.

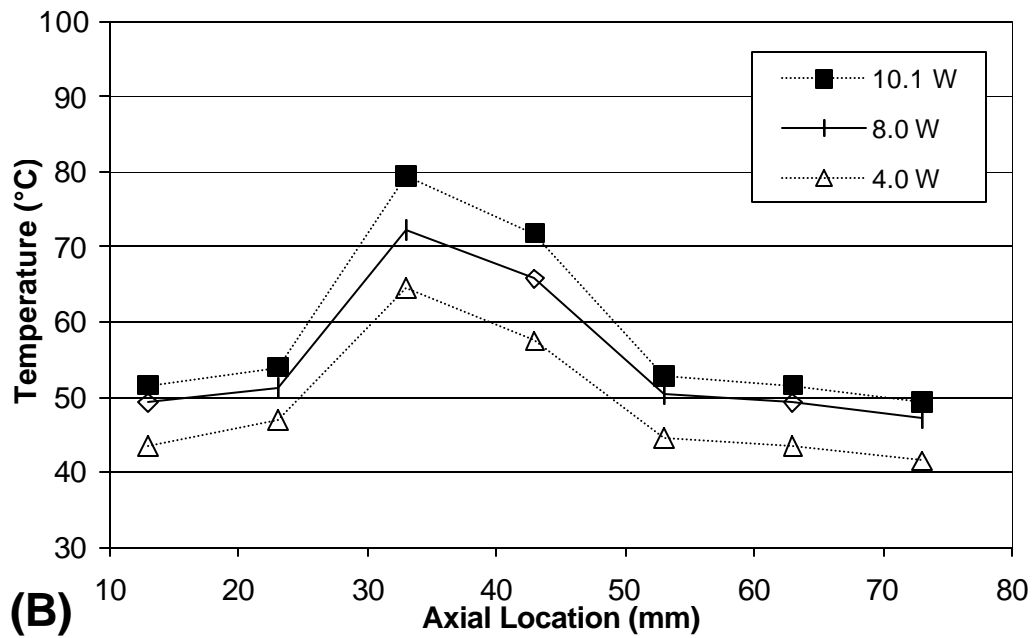
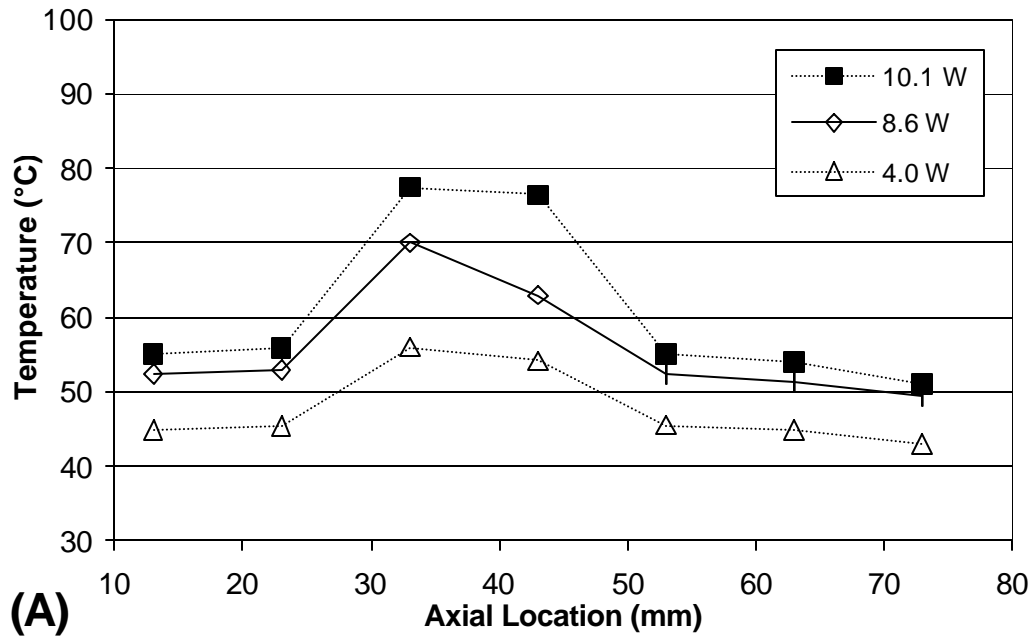


Figure 6-10. Temperature distribution along HP#10 for H3 configuration at various power levels for (A) 0° and (B) 90° axial orientation. Heater 3 is located at x=38mm and the sink temperature was 35 °C.

Recalling the discussion for Figures 6-5 and 6-6 (Overall Thermal Performance Section) it can be seen the same trends apply for all three heater configurations, noting that as the heater location moves axially along the heat pipe, so does the localized temperature "hump". The data for the H2 and H3 configurations clearly show that temperature on both sides of the heater location are relatively uniform and correspond to the temperature of the adiabatic regions of the heat pipe. Noting that as the heater moves closer to the condenser region, a second adiabatic region is created on the evaporator end-cap side of the heater. This trend is not seen for the H1 configuration (Figure 6-8), due to its proximity to the end-cap and the lack of an additional thermocouple at the end-cap itself as was discussed earlier.

In all three single heater configurations, the temperature is maximum in the immediate proximity of the heater (i.e. at the two thermocouple locations next to the heater), but quickly decreases and attains approximately the same temperature on both sides of the heater. This trend is clearly illustrated in Figures 6-8 and 6-9, for the H2 and H3 configurations. For the H1 configuration (Figure 6-7), there is approximately 1 cm of vapor space upstream (toward the evaporator end-cap) of the heater and two different trends are shown. In the horizontal orientation, the temperature continues to increase toward the evaporator end-cap, while in contrast, for the vertical orientation, the temperature on both sides of the heater is about the same. It is believed that if an additional thermocouple was available closer to the

evaporator end-cap (as for HP#7) it would be seen that the temperature would decrease back to the vapor temperature.

Upon a deeper analysis of the data from Figures 6-8, 6-9, and 6-10, it was found that the evaporator temperature in the H2 and H3 configurations was higher than that for the H1 configuration at similar power levels. To clearly see this effect refer to Figure 6-11, where the average evaporator temperature ($T_{E,AVG}$) is plotted as a function of the thermal load for all three heater configurations. Noting that all three configurations were tested using the same cold-plate temperature of 35 °C, the average evaporator temperature can be directly compared for the three configurations.

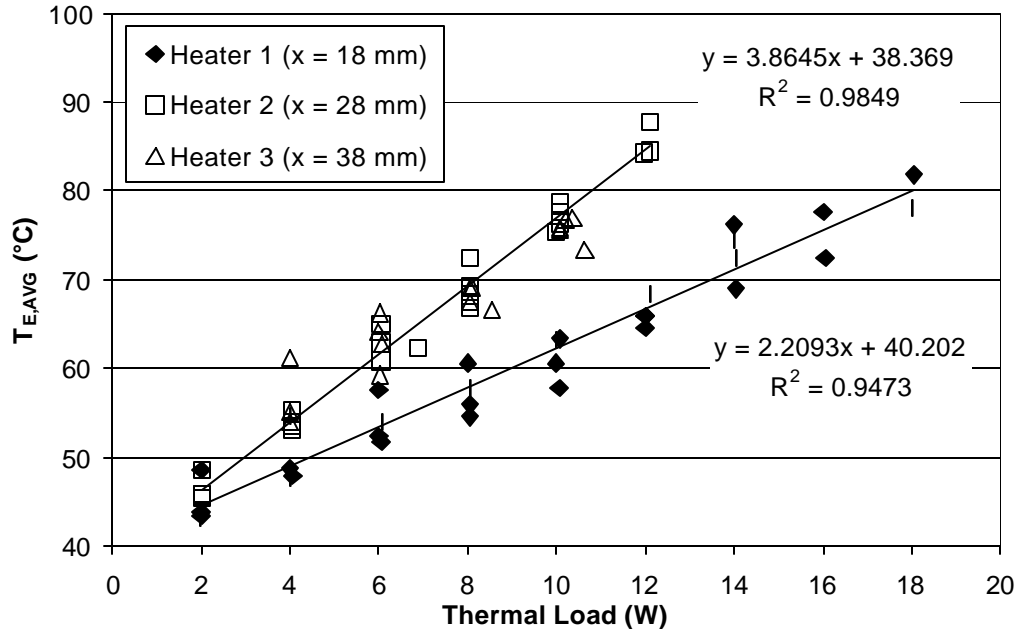


Figure 6-11. Average evaporator region for HP#10 for single heater operation. Note: Heater 2 and 3 data combined for fitted line analysis.

Referring to Figure 6-11, it is clear that the data for the H2 and H3 configurations group tightly together and apart from the data for the H1 configuration. Two lines have been fitted to the data shown with the line equations and the correlation coefficients given. For both of the lines, the intercept is near 38-40 °C which is an acceptable temperature rise over that of the cold-plate due to the thermal interface between the copper and the ceramic material. The high correlation coefficients of 0.95 and 0.98 clearly indicate that the appropriate data is well fitted by the linear trend.

The data in Figure 6-11 supports the conclusion that there is negligible axial conduction of heat through the shell material since as the heater moves toward the condenser, the axial thermal resistance would decrease causing a reduction of the evaporator temperature. This also supports that the heat pipe must be functioning with no capillary dry out occurring, because if heat had to use a conduction path through the ceramic material, then the temperature of the evaporator for H3 would be the lowest and H1 would be the highest. Furthermore, the data in the figure also infers that being passed a certain point away from the condenser end-cap causes a heat pipe to run with a higher temperature rise in the vapor from the condenser to the evaporator. A higher temperature rise in the vapor must be accompanied by an larger vapor pressure rise as well. It is surmised that this increase in the vapor pressure at the evaporator may be due to a secondary vapor flow being set up in the section of the pipe on the side of the heater away from the

condenser. This secondary vapor flow might be interfering with the primary vapor flow by requiring an increased local vapor pressure near the evaporator, or possibly by reducing the convective heat transfer process when the working fluid evaporates.

Multiple Heater Operation

During multiple heater operation, the heat pipe was run with two or more of the heaters running simultaneously. For the applications in electronic packaging, there is the potential to use a single heat pipe to cool multiple components. Each of these components would create a discrete source of heat input into the heat pipe. If these components were placed fairly close to each other, then the heat pipe would effectively have an increased evaporator region with a diminishing adiabatic region. The potential exists for a heat pipe for which the majority of its axial length is evaporator region with no adiabatic region and a relatively small condenser region.

To gain some insight into the performance of the embedded heat pipe in a multiple heater configuration, HP#10 was tested using the H12, H123, and H1234 configurations. For each of the heater configurations, the heat pipe was tested in axial orientations of 0°, 30°, 45°, and 90°. The active heaters were connected in series to the power supply, hence the total power dissipated by the set of heaters could be measured, but the power dissipated at any specific heater could not be determined. Since the resistance of the

heaters was close, a good estimation of the heat dissipated at each individual heater would be to divide the total dissipated power by the number of heaters.

In the H12 configuration, heaters 1 ($x = 18$ mm) and 2 ($x = 28$ mm) were connected in series to the power supply and operated as one single electrical load. In a similar fashion, the H123 configuration indicates that heaters 1, 2, and 3 ($x = 38$ mm) were powered together, and the H1234 configuration indicates that heaters 1, 2, 3, and 4 ($x = 48$ mm) were powered together.

The temperature distribution along the heat pipe for multiple heater operation is shown in Figures 6-12, 6-13, and 6-14. In each figure, the temperature distribution for several thermal loads is shown for both the horizontal and vertical orientations. Similar to the single heater configurations, increases in the thermal load result in a relatively linear increase in the temperature at any one specific location along the heat pipe. Also, it is clear that the highest temperatures are between active heaters and near the center of a group of heaters.

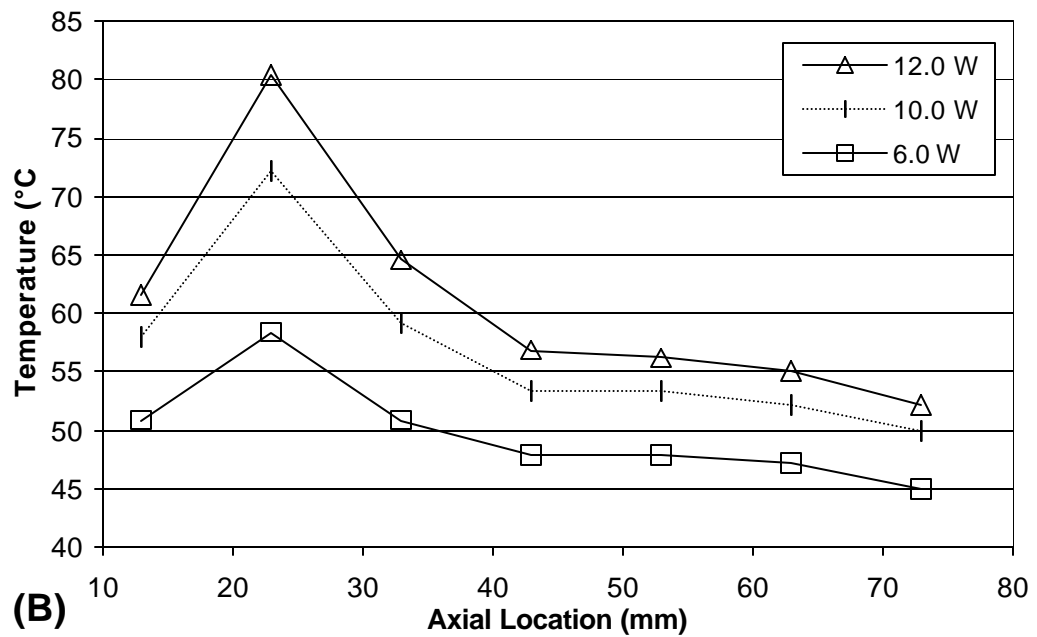
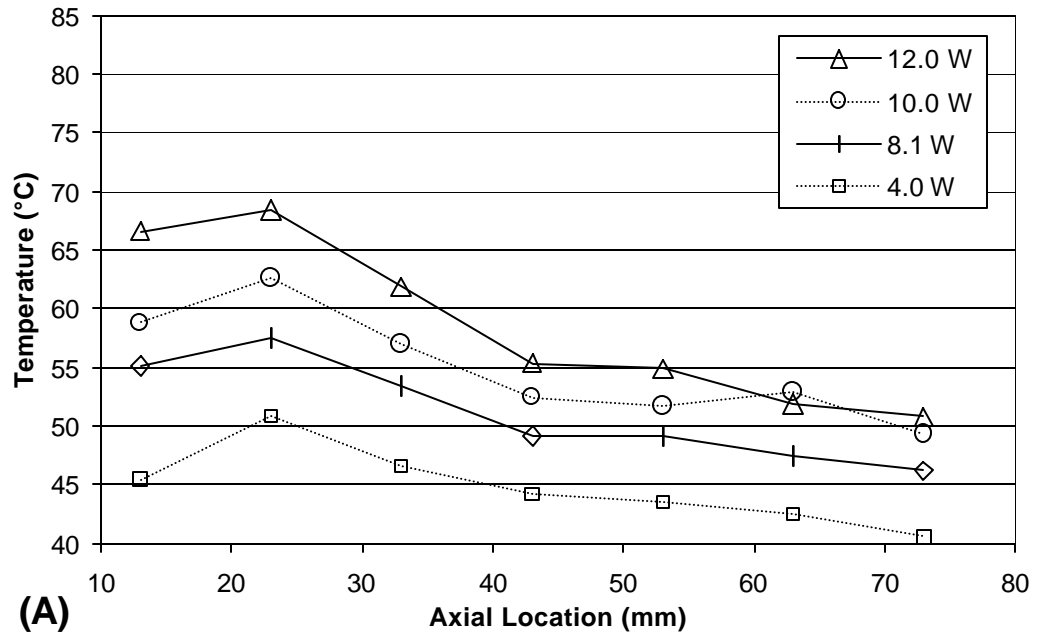


Figure 6-12. Temperature distribution along HP#10 for H12 configuration at various power levels for (A) 0° and (B) 90° axial orientation. Sink temperature was 35 °C. Heaters are located at x = 18 and 28 mm.

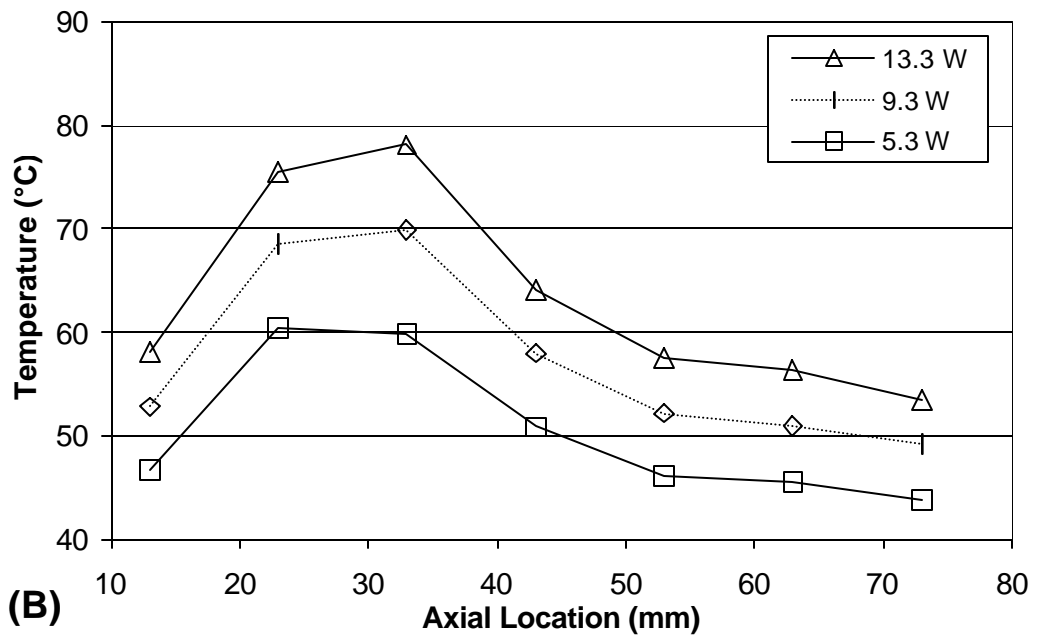
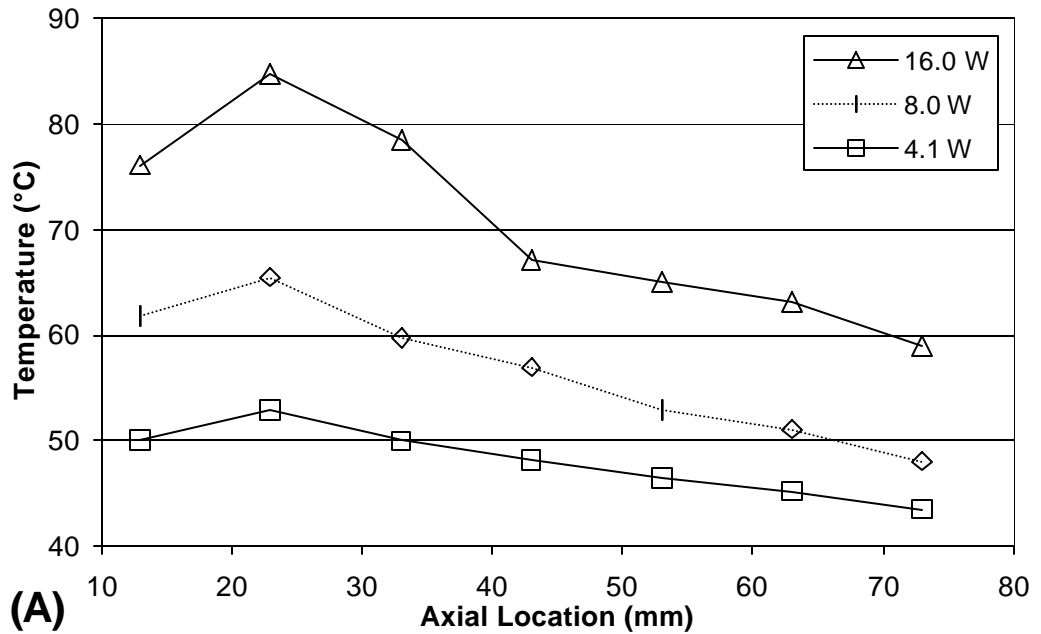


Figure 6-13. Temperature distribution along HP#10 for H123 configuration at various power levels for (A) 0° and (B) 90° axial orientation. Sink temperature was 35 °C. Heaters are located at x = 18, 28, and 38 mm.

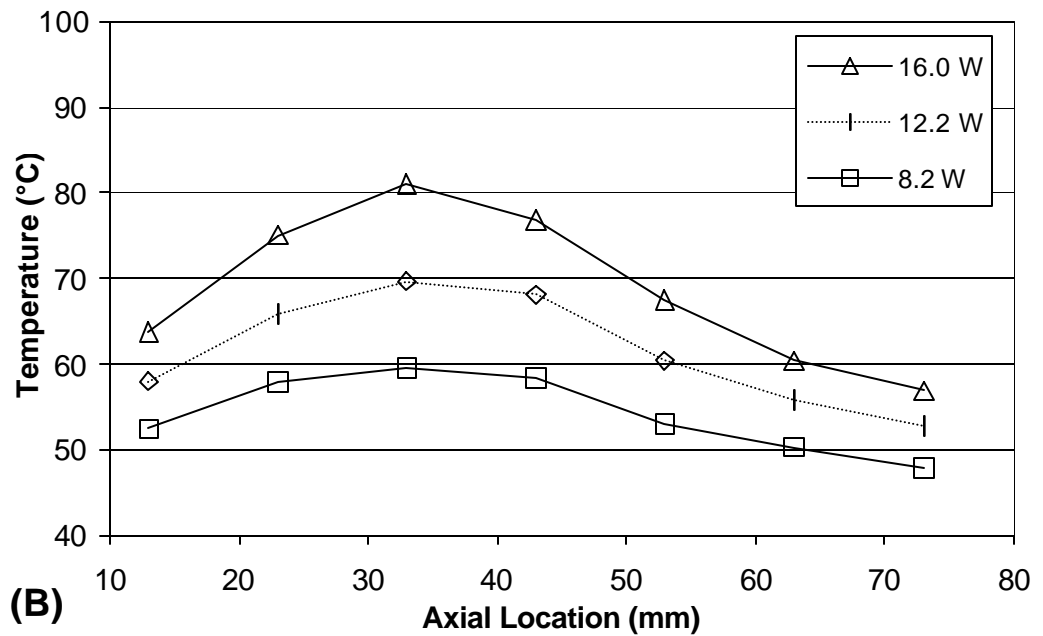
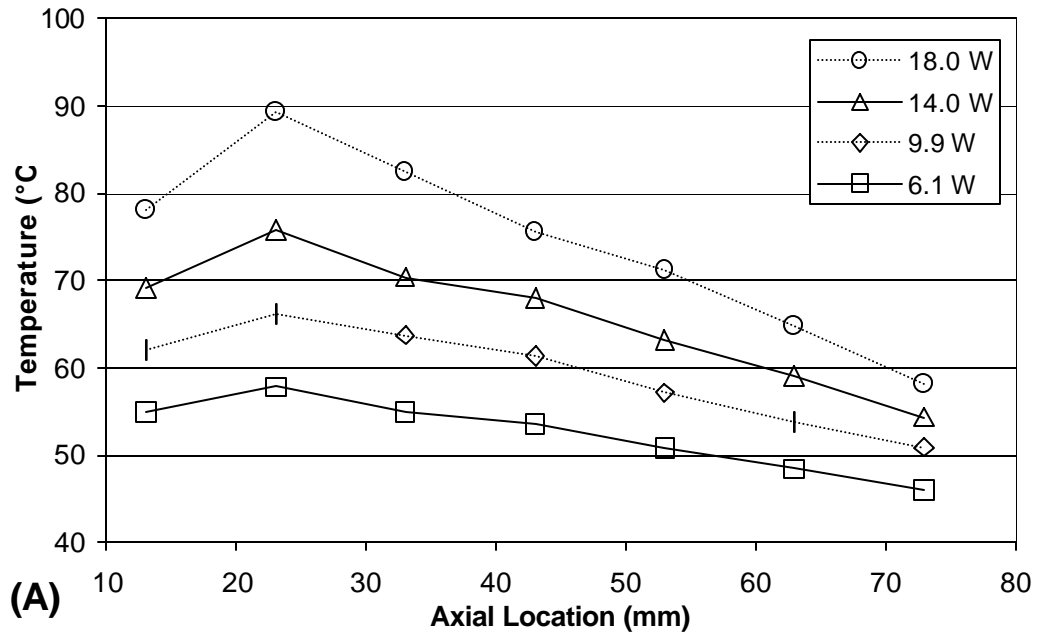


Figure 6-14. Temperature distribution along HP#10 for H1234 configuration at various power levels for (A) 0° and (B) 90° axial orientation. Sink temperature was 35 °C. Heaters are located at x = 18, 28, 38 and 48 mm.

Review of the figures indicates that the orientation of the heat pipe does appear to have a minor effect on the temperature distribution of the unheated portions of the heat pipe. For the horizontal orientation, it appears that the temperature distribution from the heaters to the condenser is more linear than those for the vertical orientation. That is, the characteristic temperature "hump" near the heaters is more distinguishable in the vertical orientations. It is surmised that this is due to some form of capillary dry-out, most likely local and partial (i.e. only a portion of the wick near the heater). However, there still must be an active two-phase heat transfer mechanism at work because the thermal resistance from the heaters to the condenser is an order of magnitude lower than for an uncharged heat pipe (refer to Figures 6-1 and Table 6-2). Furthermore, the same trend can not be found for any of the single heater configurations (refer to Figures 6-8, 6-9, and 6-10).

It is difficult to apply a quantitative trend to the data in Figures 6-12, 6-13, and 6-14. However, plotting the average evaporator temperature against the thermal load as shown in Figure 6-15 will provide a more quantitative analysis. For completeness, data for the H1 configuration has also been added to the figure to allow for a comparison of four types of heater configurations, noting that with the addition of a heater, the heat flux dissipated at each heater decreases, the effective evaporator area increases, and the effective length of the heat pipe decreases. In the figure, the data for

regression analysis for the fitted line shows that the standard error for the predicted temperature is ± 3.0 °C based on the random error in the aggregate data set.

Comparison of the data in Figure 6-11 (single heater configurations) and 6-15 (multiple heater configurations) show that for the range of thermal loads tested, the average temperature for the evaporator region for multiple heater configurations are slightly lower. This makes sense as the vapor temperature is primarily set by the total amount of heat transported by the vapor and the thermal resistance of the shell material at the condenser is the same for the configurations. Only two other thermal resistances in the system vary with heater configuration, which are the conduction path through the shell material from the heater to the wick, and the axial conduction path through the shell material.

For a specific thermal load, each heater in a multiple heater configuration dissipates less heat than a single heater configuration. Hence, there will be a smaller temperature rise due to the thermal resistance of the shell material. Additionally, for the multiple heater configurations tested, the effective length of the heat pipe decreased with additional heaters (i.e. the center of the heater group was not maintained at a specific axial location along the heat pipe). Hence, it would be expected that temperatures should be lower as the number of heaters increased in the configuration, but this is not supported by the data. This would occur if the thermal resistance of the

radial (from the heater to the wick) path was significantly smaller than the axial path. Indeed, by inspection, it can be seen that the thermal path length in the radial direction is roughly 16 times shorter than the axial path (considering the distance to the next heater location vs. the distance from the heater to the wick). Additionally, the thermal path's cross sectional area is also larger in the radial path as opposed to the axial path.

Comparison of Experimental and FEA Results

Using the methodology outlined in Chapter 4, the temperature distribution is predicted using finite element analysis and is compared to experimental data in Figures 6-16 and 6-17. A representative data set is obtained using HP#10, for which single and multiple heater configurations were tested at four axial orientations. A representative thermal load of 10 W is used for the comparison. The thermal load of 10 Watts was chosen because: (1) data for this power level was available in all the orientations and heater configurations; (2) it is near the center of the range of thermal loads tested; and (3) it was representative of the data at all of the thermal loads. Figure 6-16 compares the single heater configurations H1, H2, and H3, and Figure 6-17 compares the multiple heater configurations H12, H123, and H1234.

The set of figures has three principal uses, the first being to show a composite temperature distribution for a specific heater configuration at all available orientations. In this manner, the representative effect of the axial

orientation on the temperature distribution along the heat pipe is better illustrated than in previous figures. Secondly, the figures also provide a clear way to assess the effect of each heater configuration on the overall temperature distribution by using the same total thermal load. Third, the figures allow a comparison between FEA and experimental results.

Comparing H1, H2, and H3 heater configurations can show the effect of the heater location, and comparing H1, H12, H123, and H1234 heater configurations can show the effect of varying the effective evaporator area and the evaporator heat flux. For a total thermal load of 10 Watts and using the total area of the heater pattern of 0.258 cm^2 (0.040 in^2), the heat flux at the surface of the substrate directly under each heater can be determined. For the H1, H12, H123, and H1234 configurations, this heat flux is 38.8 W/cm^2 (250 W/in^2), 19.4 (125), 12.9 (83.3), and 9.69 (62.5), respectively.

Referring to all the figures, it is clear that the orientation has: (1) no conclusive effect on the temperature distribution; (2) any scatter in the data is relatively small; (3) any particular variations in the data can be conclusively related to the axial position. In all the figures, at any specific axial position, the scatter in the temperature data is under 10°C , and in most cases, the scatter is less than 5°C .

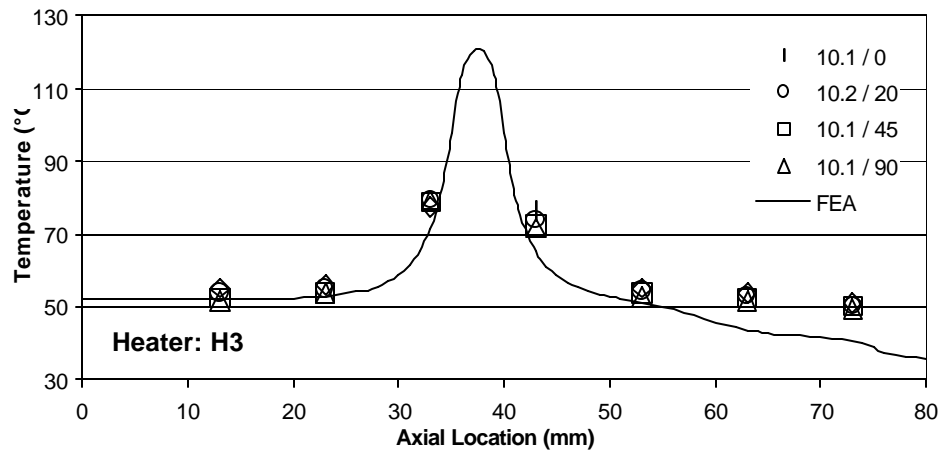
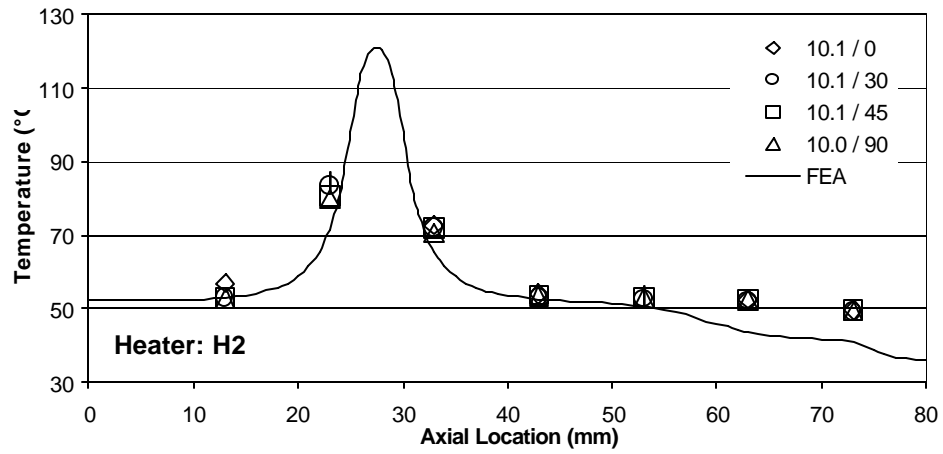
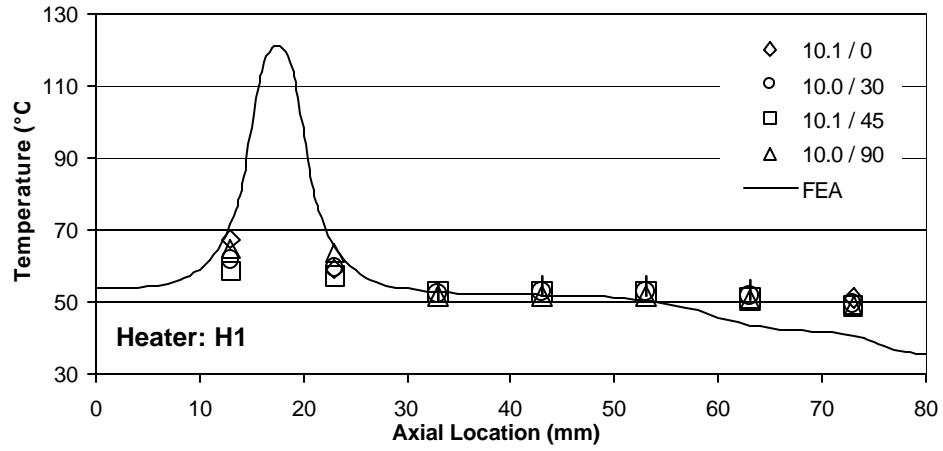


Figure 6-16. Comparison of experimental and numerical temperature data for HP#10 at various axial orientations and single heater configurations. Legend indicates Power Level (W) / Axial Orientation (degrees).

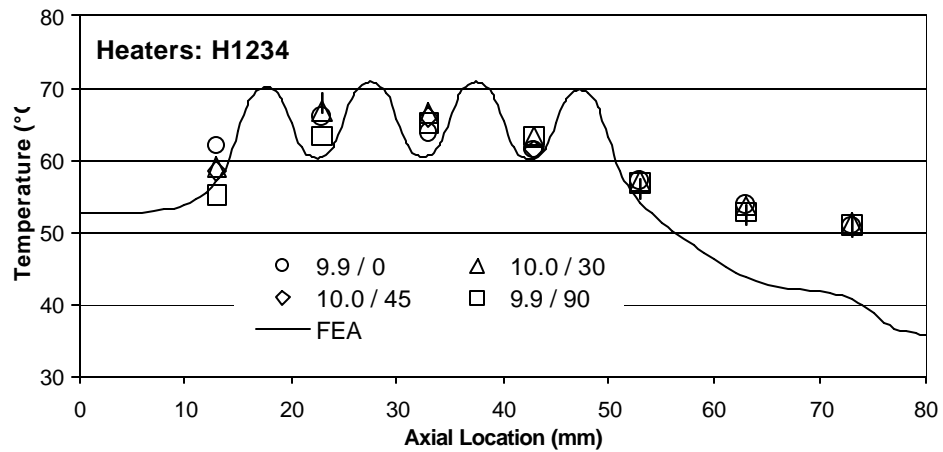
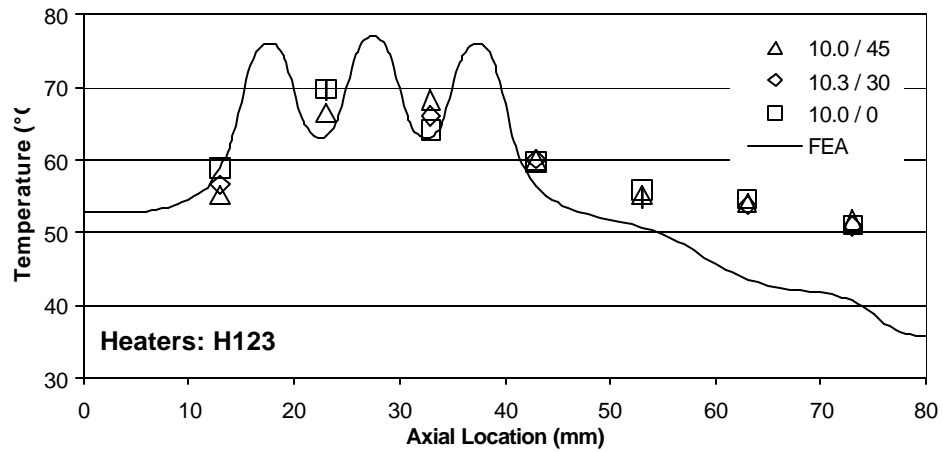
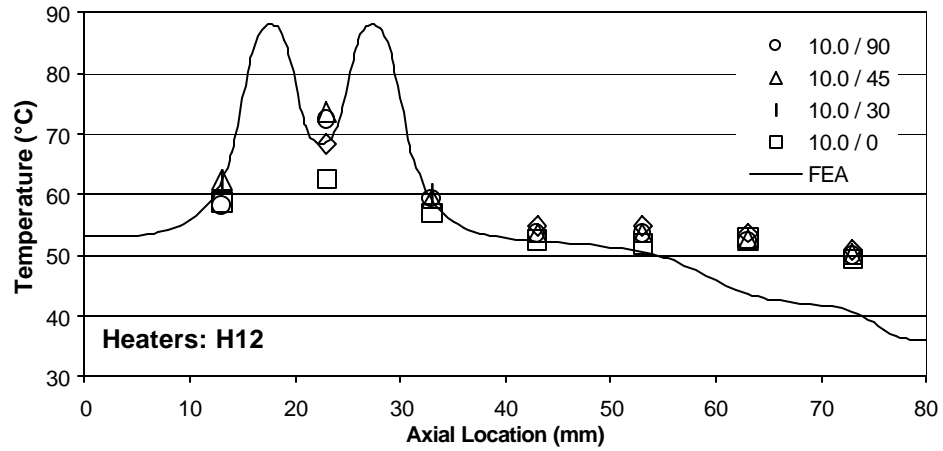


Figure 6-17. Comparison of experimental and numerical data for HP#10 at various axial orientations and multiple heater configurations. Legend indicates Power Level (W) / Axial Orientation (degrees).

The noticeable deviation of the FEA results and the measured results in both figures is in the condenser region where the FEA results predict a lower temperature than the measured data. This is explained by noting that the boundary conditions only allowed convection heat transfer along the wick surface. This convection heat transfer represents the heat transfer between the vapor and the internal surfaces in the heat pipe where condensation exists. Condensation will occur along all surfaces where the surface temperature have the necessary sub-cooling, i.e. at or near the vapor temperature and heat is removed at a sufficient rate to cause condensation. It is not known a priori what surfaces will satisfy this condition, hence, to be conservative in the FEA models, it was assumed that this condition would occur only along the wick at axial locations coincident with the cold-plate interface. It is clear from the experimental data shown in Figures 6-16 and 6-17, that the heater side of the substrate is at or near the vapor temperature. This supports that condensation was actually occurring along the heater side of the substrate. and being that this surface is the farthest from the interface between the cold-plate and the substrate, then condensation was occurring along all four sides of the heat pipe in the condenser region. Therefore, a more realistic boundary condition would be to allow convection (i.e. condensation) along all four sides of the heat pipe in the condenser region. This would have essentially driven all of the nodal temperatures to the vapor temperature in the region and making the

predicted temperature distribution shown in the figures match the measured data.

Now, focusing on the evaporator region, it is clear that the measured data is in excellent agreement with the FEA results, specifically near the locations of the active heater(s). The data in Figure 6-16 show that the numerically predicted axial temperature distribution is essentially identical for all the single heater configurations except for the axial translation of the temperature peak location to coincide with the location of the heater. This translation is expected, as the boundary conditions for each heater configuration were identical except for the translation of the heat source. In Figure 6-17, the numerical results capture the larger temperature "hump" along the extended evaporator region and agree well with the measured temperatures between each heater location. It appears that the FEA results may be slightly lower than the measured data between the heaters, especially for the H123 and H1234 configurations. However, this deviation is under 5 °C in all figures and would be due to the convection heat transfer coefficient used in the boundary condition being slightly too high. It was surmised in previous sections that for the multiple heater configurations, the presence of multiple heat sources has some effect on the vapor flow within the heat pipe. This can now be extended to include that this affects the evaporation process by reducing its effectiveness.

The important use of the FEA results is to predict the temperature under the heater locations, which could not be directly measured. With the excellent agreement of the measured temperature data and the FEA results, the models are validated for use in determining the local temperature directly under the heater(s) by numerical extrapolation. Reviewing both Figures 6-16 and 6-17, it is apparent that the temperature of the heaters can be significantly increased over that of the vapor temperature, and even the nearby ceramic material. As the number of heaters increased, the local dissipated power decreased proportionately causing multiple temperature "spikes" to emerge within the more global temperature "hump". In any event, the use of the finite element analysis, clearly supports that the cause of the temperature rise is due to the low thermal conductivity of the shell material and not due to global dry-out of the wick structure (recalling that this is addressed directly in Chapter 4).

The FEA results for the multiple heater configuration (Figure 6-17) also help to clearly show that the temperature of an individual heater is relatively insensitive to the conditions of nearby heaters. This is seen by the very discrete temperature spikes being formed with lower temperatures found between the heaters. Due to the relatively low thermal conductivity of the ceramic material, the thermal path in the radial direction from the heater to the wick is roughly ten times shorter than the path in the axial direction to the next heater. Thus, as long as the heat pipe is operating, little thermal

spreading should occur that would cause one heater to affect the temperature at another heater location. This is a sharp contrast to conventional metal miniature heat pipes with multiple heat sources which tend to attain a more uniform temperature distribution throughout the heated area, causing a greater thermal interaction between heater sites.

System Thermal Resistance

In order to assess the thermal performance enhancement due to the embedded heat pipes, the thermal resistance of the substrate/heat pipe system needs to be known. The system thermal resistance was defined by Equation 4.14 using the maximum heater temperature and the heat sink temperature. In this chapter, the results of the FEA models was compared with experimental data, showing excellent agreement between the two, and validates the use of the FEA results in estimating the maximum heater temperature and the thermal resistance between the heater and the vapor temperature. Using this data, an estimate of the thermal resistance from the heater to the vapor is about 4.7 °C/W for HP#7 (Top/Bottom wick) and about 6.8 °C/W for HP#10 (Side-Wall wick).

The vapor temperature can be estimated quite reliably for the single heater configurations at various thermal loads, however, for multiple heater configurations the vapor temperature is not as clearly defined. The comparison of the FEA model results and the experimental data shows that using the average evaporator region temperature (measured data shown in

Figures 6-11 and 6-15) can provide a conservative estimate of the vapor temperature. The slopes of the fitted lines in these figures lead to an estimate of the thermal resistance from the vapor to the heat sink of about 2.2 °C/W for all heat pipes. Thus, the system thermal resistance is estimated to be about 6.8 °C/W for HP#7 and about 8.9 °C/W for HP#10.

To determine the enhancement in the substrate due to the addition of the embedded heat pipe, the system thermal resistance should be compared to that of a solid substrate without any embedded heat pipe. As presented in Table 4-2, the thermal resistance for a solid substrate (thermal load at H1) is 45 °C/W and 58 °C/W for HP#7 and HP#10, respectively. No experimental data is available for a solid substrate sample, however, data was discussed in this chapter for a dry heat pipe which indicated (after losses to the ambient were considered) that the thermal resistance for samples with a dry heat pipe were about 60-65 °C/W. This experimental range of values agrees well with the FEA results of 57-66 °C/W. Hence, the FEA results can be used in the absence of experimental data. Therefore, taking the ratios of the thermal resistance for a solid substrate and the substrate with a heat pipe indicates, conservatively, that there is a 6.6X and 6.5X reduction in the thermal resistance of the substrate system due to the embedded heat pipe, for HP#7 and HP#10, respectively.

VI. Conclusions

Miniature heat pipes have been embedded in HTCC substrates using conventional cofired ceramic fabrication methods. Furthermore, these heat pipes have been demonstrated to operate successfully in transporting heat through the substrate material providing at least a 6X reduction in the thermal resistance from the heat source to the thermal sink. Successful fabrication of the heat pipes as an integral part of the electronic substrate validates the concept for a new thermal management technology for ceramic microelectronic packages and should serve to initiate the development of other substrate integrated fluid-thermal systems. The overall objective of the research was satisfied with the development and testing of the prototype heat pipes. The practical knowledge and data gathered provides a quantitative and qualitative baseline for the design and use of embedded heat pipes as a thermal management technique in ceramic substrates and packages. Furthermore, the knowledge and data gathered in developing and testing the embedded heat pipes gives a clear direction for future research in improving this thermal management technique.

Reviewing the discussion of Chapter 3 (i.e. fabrication) several key topics related to the fabrication of embedded heat pipes in cofired ceramic materials were discussed. The first conclusion to be drawn is that cofired ceramic materials are very different from conventional metals and have a unique set of processing needs. Hence, the development of embedded heat

pipes in cofired ceramic substrates forces one to discard conventional heat pipe manufacturing techniques and to develop new approaches to designing and building functional heat pipes within the restrictions of the ceramic material and the cofire ceramic process. The wick structures developed were the two simplest that were feasible using conventional fabrication methods. Using these same techniques, wick designs which incorporate z-axis fluid transport are feasible and should further increase the performance of the heat pipes.

A critical weakness in the cofired ceramic fabrication is the viscoplastic deformation of the green tape during the lamination process. Using the standard lamination approach, the successful fabrication of substrates with internal cavities of any form is problematic to non-feasible. In this study, the development of a multi-step lamination process minimized the viscoplastic deformation to allow for heat pipes to be fabricated. However, sag of the material on the top and bottom of embedded cavities is inevitable due to the viscoplastic deformation of the tape during lamination, and the fabrication of wide cavities appears to be not practicable. Fortunately, research subsequent to this study was initiated to develop an enhanced lamination process. At the time of the writing of this dissertation, significant advances were made in the use of organic inserts which are laminated inside the ceramic tape stack. These inserts provide an internal reaction force for all unsupported tape

areas during lamination. During the firing process, the insert material burns-out of the ceramic entirely.

The fill tube attachment on the prototype heat pipes is simple, functional, and adequate to meet the objectives of this study. However, for industrial application a more robust fitting should be employed. Such a fitting will probably be brazed to the ceramic instead of soldered and will be sealed by arc welding, ball insertion, or crimp/weld. Additionally, the footprint and total height of the fitting will need to be reduced for microelectronic applications.

The prototype heat pipes were tested to evaluate their thermal performance. In the evaluation, the temperature distribution along the substrate's surface was measured for varying thermal loads supplied from single and multiple sources. Thermal loads up to 27 Watts were tested in several configurations with variations in axial orientation and wick structure. The data provided insight into the operation of the heat pipes in various operating configurations. The overall conclusion drawn from all the thermal data is that the heat pipes were fairly insensitive to variations in axial orientation, heater configuration, and wick structure. In the end, all the pipes provided roughly the same enhancement in heat transfer in the substrate regardless of the various configurations. Essentially, it is felt that the same uniform trends were observed in all the data with appropriate variations attributed to heater location or more than one heat source.

The primary reason for the lack of any unique phenomena among all the various configurations tested is attributed to the relatively low thermal loads tested, which appear not to be large enough to cause a total capillary dry-out condition. Although there is some support in the data that very localized wick dry-out may have occurred at higher thermal loads, the data and the numerical modeling clearly indicate that if the wick below a heater location is totally dry, an extreme temperature rise would have occurred. At the thermal loads tested, such a temperature rise would have been in the 200-1600 °C range, which did not occur, hence, working fluid must have been directly under the heater locations and a stable two-phase heat transfer mechanism must have been occurring.

The key limitation is the testing of the heat pipes was initially poor heater construction, which led to the mechanical failure of some of the samples. However, with the heater problem resolved, the single largest factor limiting the testing at higher thermal loads and the practical use of the technology developed in this study, is the large thermal resistance of the shell material. This problem is significant for the HTCC alumina material used in the samples, but becomes critical if this technology is to be transferred to the more cost-effective LTCC materials. The solution to this problem is the use of thermal vias in the shell material to provide an increase in the effective thermal conductivity of the shell material in the location of the heaters and the heat sink. Such thermal via arrays can increase the effective thermal

conductivity of the HTCC materials to over 120 W/m-K, effectively eliminating the problem. Unfortunately, thermal via fabrication in HTCC was not feasible under the scope of this research. Fortunately, concurrent to this study, cofired ceramic fabrication capabilities for LTCC materials was being developed at the University with a focus on building large area thermal via arrays. During the writing of this dissertation, large area thermal via arrays were demonstrated by other researchers at the University, with an effective thermal conductivity starting at 80 W/m-K and higher.

With the recent developments in LTCC fabrication, specifically large area via arrays and large cavity lamination, embedded heat pipes should be demonstrated successfully in LTCC substrates. Internal wick structures can initially be conventional as the ones developed in this study, however, the insert lamination process provides great promise for highly intricate wick designs to be practicable, further improving upon the thermal performance presented in this study.

List of References

- Babin, B.R., Peterson, G.P., and Wu, D., 1989, "Steady State Modeling and Testing of a Micro Heat Pipe," *ASME Journal of Heat Transfer*, Vol. 112, pp. 565-601.
- Bauer, R., Luniak, M., and Rebenklau, L., 1997, "Realization of LTCC-Multilayer With Special Cavity Applications," *Proceedings of 1997 International Symposium on Microelectronics*, IMAPS, Philadelphia, PA.
- Cao, Y., Faghri, A., and Mahefky, E.T., 1993, "Micro/Miniature Heat Pipes and Operating Limitations", *ASME HTD-Vol. 236*, pp. 55-62.
- Cao, Y., Gao, M., Beam, J.E., and Donovan, B., 1997, "Experiments and Analyses of Flat Miniature Heat Pipes", *AIAA Journal of Thermophysics and Heat Transfer*, Vol. 11, No. 2, pp. 158-164.
- Chen, H., Groll, M. and Rosler, S., 1992, "Micro Heat Pipes: Experimental Investigation and Theoretical Modeling," *Proc. 8th Int. Heat Pipe Conf.*, Beijing.
- Cotter, T.P., 1984, "Principles and Prospects of the Micro Heat Pipes," *Proc. 5th Int. Heat Pipe Conf.*, Tsukuba, Japan.
- Engineering Mechanics Research Corporation, 1995, NISA II User's Manual.
- Espinoza-Valejos, P.A., Santiago-Aviles, J.J., Sola-Laguna, L., Zhong, J., and Gongora-Rubio, M., 1997, "Meso-Scale Electromechanical Systems for the Measurement and Control of Sagging in LTCC Structures", *Proceedings of the Material Research Society Conference Proceeding*.
- Faghri, A., 1995, Heat Pipe Science and Technology, Taylor and Francis, Washington, D.C.
- Gao, M. and Cao, Y., Beam, J.E., and Donovan, B., 1999, "Structural Optimization of Axially Grooved Flat Miniature Heat Pipes," *Proc. 1999 AIChE Symposium Series in Heat Transfer*, Vol. 93, Baltimore.
- Gerner, F.M., Longtin, J.P., Henderson, H.T., Hsieh, W.M., Ramadas, P., and Chang, W.S., 1992, "Flow and Heat Transfer Limitations in Micro Heat Pipes," *ASME HTD-Vol. 206-3*, pp. 99-105.
- Ha, J.M., and Peterson, G.P., 1998, "The Heat Transport Capacity of Micro Heat Pipes," *ASME Journal of Heat Transfer*, Vol. 120, pp. 1064-1071.
- Hopkins, R., Faghri, A., and Khrustalev, D., 1999, "Flat Miniature Heat Pipes With Micro Capillary Grooves", *ASME Journal of Heat Transfer*, Vol. 121, pp. 102-109.

- Kline, S.J., and McClintock, F.A., 1953, "Describing Uncertainties in Single-Sample Experiments," *Mech. Eng.*, January.
- Kojima, Y., Yamazaki, N., Yoshida, K., Mishiro, H., and Murakami, M., 1992, "LSI Cooling System with Micro Heat Pipe," *Proc. 8th Int. Heat Pipe Conf.*, Beijing.
- Lee, Y.S., Lee, Y.P., and Lee, Y., 1992, "An Experimental Study on Micro Two-Phase Closed Thermosyphons With Inserts," *Proc. 8th Int. Heat Pipe Conf.*, Beijing.
- Li, T., Cao, L., and Xiang, L., 1992, "Research and Application for the Heat Transfer Performance of Small Heat Pipes," *Proc. 8th Int. Heat Pipe Conf.*, Beijing.
- Longtin, J.P., Badran, B., and Gerner, F.M., 1994, "A One Dimensional Model of a Micro Heat Pipe During Steady-State Operation," *ASME Journal of Heat Transfer*, Vol. 116, pp. 709-715.
- Lopez de Uralde, R., 2000, M.S. Thesis, Florida International University.
- Lynch, H., Park, J., Espinoza-Valejos, P.A., Santiago-Aviles, J.J., Sola-Laguna, L., 1998, "Meso-Scale Pressure Transducers Utilizing Low Temperature Cofired Ceramic Tapes", *Proceedings of the Material Research Society Conference Proceeding*.
- Ma, H.B., and Peterson, G.P., 1996, "Experimental Investigation of the Maximum Heat Transport in Triangular Grooves," *ASME Journal of Heat Transfer*, Vol. 118, pp. 740-746.
- National Electronic Manufacturer's Initiative, 1995, "Technology Roadmap."
- Omega Engineering Inc., 1999, "Technical Manual for CIO-DAS802/16."
- Peterson, G.P., Duncan, A.B., and Weichold, M.H., 1993, "Experimental Investigation of Micro Heat Pipes Fabricated in Silicon Wafers," *ASME Journal of Heat Transfer*, Vol. 115, pp. 751-756.
- Plesch, D., Bier, W., Seidel, D., and Schubert, K., 1991, "Miniature Heat Pipes for Heat Removal from Microelectronic Circuits," *ASME DSC-Vol. 32*, pp. 303-313.
- Schneider, G.E., and DeVos, R., 1980, "Nondimensional Analysis for the Heat Transport Capability of Axially-Grooved Heat Pipes Including Liquid/Vapor Interaction," *AIAA Paper No. 80-0214*.
- Semiconductor Industry Association, 1995, "Technology Roadmap."
- Shah, R.K. and Bhatti, M.S., 1987, "Laminar Convective Heat Transfer in Ducts", in Handbook of Single-Phase Convective Heat Transfer, Eds., Kakac, S., Shah, R.K., and Aung W., Wiley, New York.

- Thelemann, T., Thust, T. Bischoff, G., and Kirchner, T., 1999, "Liquid Cooled LTCC-Substrates for High Power Applications", *Proceedings of 1999 International Symposium on Microelectronics*, IMAPS..
- Wilcox, D., Huang, R.F., Andersen, D., 1997, "The Multilayer Ceramic Integrated Circuit (MCIC) Technology: Opportunities and Challenges," *Proceedings of 1997 International Symposium on Microelectronics*, IMAPS, Philadelphia, PA.
- Wilcox, D., 1971, "Ceramics for Packaging", Parts I and II, *Solid State Technology*, Jan. and Feb.
- Wu, D., and Peterson, G.P., 1991, "Investigation of the Transient Characteristics of a Micro Heat Pipe," *AIAA Journal of Thermophysics and Heat Transfer*, Vol. 5, pp. 129-134.
- Zampino, M. and Jones, W.K., 1997, "Substrate Embedded Heat Pipes Compatible With Ceramic Cofire Processing", *Proceedings of 1997 International Symposium on Microelectronics*, IMAPS, Philadelphia, PA.
- Zampino, M. Jones, W.K., and Cao, Y., 1998, "Substrate Embedded Heat Pipes Compatible With Ceramic Cofire Processing", *IMAPS Journal of Microcircuits and Electronic Packaging*, Vol. 21, No. 1, pp. 52-58.
- Zhou, J., Yao, Z., and Zhu, J., 1992, "Experimental Investigation of the Application Characters of Micro Heat Pipe," *Proc. 8th Int. Heat Pipe Conf.*, Beijing.

Appendix

Wetting Angle Assessment of Various Ceramic Substrate Materials

As discussed in Chapter 3, the wetting angle was measured using a Tantec Wetting Angle Meter, which employs the sessile drop method. Seven LTCC materials were tested and compared to HTCC 99% alumina. All of the samples were laminated and fired as per the manufacturer's specifications and at least twelve measurements were made on each sample as multiple locations on the sample so as to minimize the chance of a single surface aberration from skewing the results. The mean wetting angle for each of the materials is shown in Figure A-1. Additionally, descriptive statistics were performed on the measurements and are shown in the following Table A-1.

Material								
DuPont 943	DuPont 951AT LTCC	Motorola T2000	Hereaus CT-800	Hereaus CT-700	Ferro A-6	HTCC Alumina	Englehard A2282 / Alumina	Englehard A2282 / 951AT
60	18	50	28	28	36	60	50	52
54	19	48	32	34	24	60	16	46
64	22	42	30	40	24	59	16	44
64	18	54	30	55	22	60	17	18
56	25	52	32	28	34	68	22	20
66	26	48	36	28	22	60	50	30
58	24	20	36	32	28	58	48	30
62	18	48	35	32	28	59	48	36
54	20	58	38	31	28	58	58	38
66	24	44	36	30	24	56		
58	28	42	42	42	28	59		
54	22	46	38	42	30	60		
66	25	22	38	30	24	60		
58	24	42	36	45	38	64		
58	28	62	36	44	26	58		
	28	42		34	24	58		
	26	42		38	32	62		
	29	50		30	30	64		
	20	50		34	30	58		
	30	44		38	26	60		
	28	42		42				
	28	42		38				
	20							
	26							

Table A-1. Raw data samples of wetting angle for water on various ceramic substrate materials.

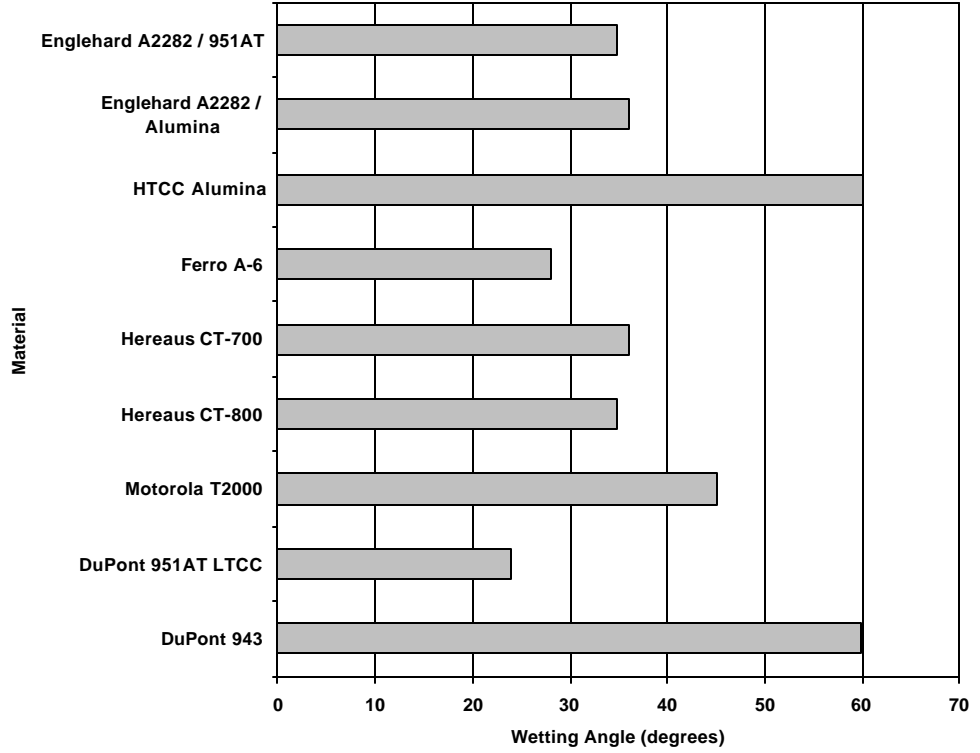


Figure A-1. Measured wetting angle of water on various cofired ceramic materials.

Material	DuPont 943	DuPont 951AT LTCC	Motorola T2000	Hereaus CT-800	Hereaus CT-700	Ferro A-6	HTCC Alumina	Englehard A2282 / Alumina	Englehard A2282 / 951AT
Mean	59.9	24.0	45.0	34.9	36.1	27.9	60.1	36.1	34.9
Standard Deviation	4.5	3.9	9.5	3.8	6.9	4.5	2.7	17.8	11.5
Minimum	54	18	20	28	28	22	56	16	18
Maximum	66	30	62	42	55	38	68	58	52
Count	15	24	22	15	22	20	20	9	9
Confidence Level(95.0%)	2.5	1.6	4.2	2.1	3.1	2.1	1.3	13.6	8.9

Table A-2. Descriptive statistics for measured wetting angle of water on various cofired ceramic materials.

Enhancement of Wetting on Cofired Ceramics

It is understood that the wetting of a liquid on a surface can be increased through the use of surface treatments and surfactants. Two surface treatments were investigated, as they were compatible with the cofired ceramic materials and fabrication process. The first material was a silver metallo-organic coating (Engelhard A2272) and the second material was a platinum electrode ink (Engelhard A6090XF). A metallo-organic is an organic compound which has as part of its molecular chains a metal component. Upon firing at elevated temperature, the organic structure breaks down leaving behind the metal component, which adheres to the surface to be treated. Such a material is ideal for use with the cofired ceramic heat pipes as it can be applied after the firing of the ceramic substrate and then injected into the heat pipe and allowed to flow into the wick structure via capillary action. The second material is a thick film ink which contains no frit, or glass, material, hence, it is designed to be fired on the inner layers of the cofired ceramic substrate. This material is slightly viscous and can not be readily poured into the heat pipe after the firing of the ceramic as it is too viscous to be drawn into the wick structure by capillary action. Hence, this material would have to be applied during the stacking and lamination process.

Both materials were tested on samples of DuPont 951AT (LTCC) and 99% alumina (HTCC). The results of the wetting tests for the silver metallo-

organic are given in Figure A-1, and show that the silver material gives a relatively constant wetting angle of approximately 35° on both the LTCC and HTCC materials. This is expected as the wetting will become more dependent on the surface material and not the substrate material. Referring to Table 4-2 it can be seen that the random error in the measurements were about twice that of the substrate materials alone. This is most likely due to the increase in surface waviness that results after the silver metallo-organic is fired onto the ceramic materials. In any case, for the materials with a higher wetting angle, the use of the metallo-organic should provide an increase in the wetting of the working fluid. A micrograph of the metallo-organic on the DuPont 951AT sample is shown in Figure A-A, which shows that the coating is relatively consistent with occasional voids. Additionally, the surface appears to have a slight waviness, which may have resulted from the thick application of the liquid prior to firing.

Wetting data for the platinum surface treatment was not readily available as the material absorbed the water without forming a sessile drop. This indicated that the material was porous. This conclusion was verified when the surface was examined with a scanning electron microscope. A micrograph of the platinum coating is shown in Figure 4-3, from which one can estimate visually that the coating has a porosity of 20-40%. The porous nature of the material is not unexpected as the ink contained no frit component, and it was fired at 850 °C, which is below the melting point of

platinum. At the lower firing temperature, the platinum particles will begin to sinter, causing 'necking' between particles. The temperature is not high enough for aggressive necking to occur, which would cause the particles to sinter together forming a more homogeneous material. The ability of this material to wet and readily transport the fluid by capillary action, makes it an ideal candidate for use a wick structure or as an enhancement for wetting along axially grooved wick structures. Similarly, the porosity of the material may also provide some enhancement for the evaporation and condensation processes within the heat pipe.



Figure A-2. Micrograph of silver metallo-organic surface coating on DuPont 951AT (LTCC).

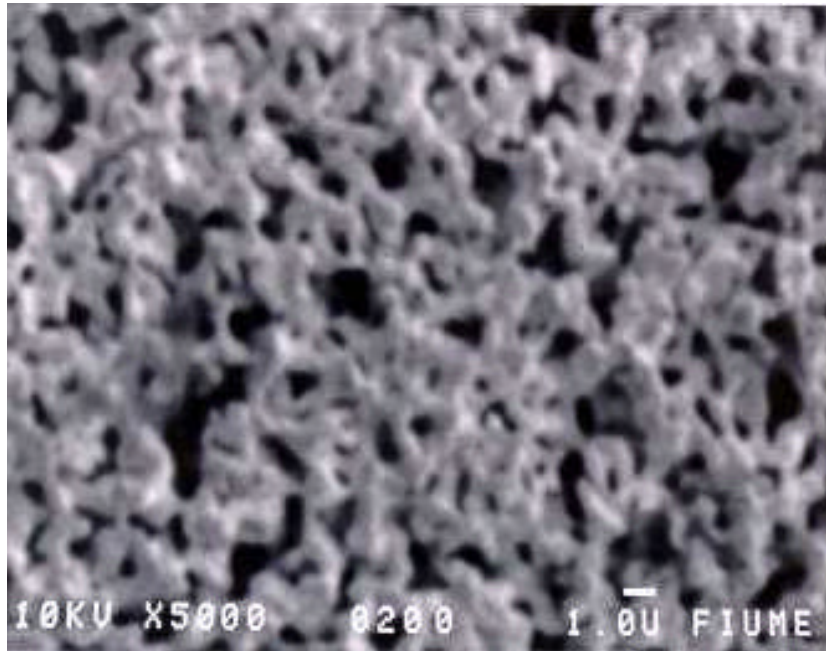


Figure A-3. Micrograph of platinum surface treatment on HTCC alumina.

Uncertainty Analysis: Sample Calculations

Given a nominal voltage of 20.0 Volts and a nominal current of 1.5 Amps and the following elemental uncertainties as shown in following table:

	Voltage (V)	Current (A)
Instrument Uncertainty	± 0.10	$\pm 0.0075 + \pm 0.015$
Readout Fluctuation	± 0.005	± 0.05

The elemental uncertainty of the voltage measurement is determined as follows:

$$w_V = \sqrt{v_1^2 + v_2^2 + \dots + v_n^2} = \sqrt{(0.10)^2 + (0.005)^2} = \pm 0.100 \text{ V}$$

and similarly for current:

$$w_V = \sqrt{(0.0075)^2 + (0.015)^2 + (0.05)^2} = \pm 0.0527 \text{ A}$$

The propagated error in the Power (Power = Voltage x Current) due to the elemental uncertainties in V and I is determined using the following methods:

$$U_{P,RSS} = \sqrt{\sum_{i=1}^n \left(w_i \frac{\partial R}{\partial x_i} \right)^2} = \sqrt{(w_V I)^2 + (w_I V)^2}$$

$$= \sqrt{(0.10 * 1.5)^2 + (0.05 * 20)^2} = \pm 1.0112 \text{ W}$$

$$U_{P,MAX} = \sum_{i=1}^n \left| w_i \frac{\partial R}{\partial x_i} \right| = w_V I + w_I V = 0.10 * 1.5 + 0.05 * 20 = \pm 1.155 \text{ W}$$

VITA

MARC A. ZAMPINO

June 1, 1963	Born, Brooklyn, New York
1986	B.S. in Aerospace Engineering The Pennsylvania State University State College, Pennsylvania
1986 to 1989	Lead Flight Test Engineer Veda Incorporated Lexington Park, Maryland
1992	M.S. in Mechanical Engineering Florida International University Miami, Florida
1993	Cooperative Research Assistant Martin Marietta Corporation Orlando, Florida
1994 to 1996	Mechanical Engineer Lambda Novatronics, Inc. Pompano Beach, Florida
1999-present	Manager, Teaching Laboratories Florida International University Dept. of Mechanical Engineering Miami, Florida

PUBLICATIONS AND PRESENTATIONS

Zampino, M.A. and Jones, W.K., "Embedded Heat Pipes in Ceramic Cofire Substrates", *Proc. SAE Aerospace Power Systems Conf.*, SAE Paper No. 1999-01-1361, Mesa, Arizona, 1999.

Zampino, M.A., and Jones, W.K., "Embedded Heat Pipes In Cofire Substrates For The Transport and Spreading of Heat", *Proc. Advanced Technology Workshop on Thermal Spreaders and Heat Sinks*, IMAPS, San Diego, 1999.

- Zampino, M.A., and Jones, W.K., "Embedded Heat Pipes With MCM-C Technology", *Proceedings of NEPCON West*, Anaheim, 1998. (Presentation)
- Zampino, M.A., Jones, W.K., and Cao, Y., "Substrate Embedded Heat Pipes Compatible With Ceramic Cofire Processing", *Int. J. Microcircuits and Electronic Packaging*, Vol. 21, No. 1, pp. 52-58, 1998.
- Zampino, M. and Jones, W.K., 1997, "Substrate Embedded Heat Pipes Compatible With Ceramic Cofire Processing", Proc. 1997 Int. Sym. Microelectronics, IMAPS, Philadelphia, PA.
- Jones, W.K., Liu, Y.Q., Zampino, M.A., and Gonzalez, G., "The At-Temperature Properties of Lead-Tin-Based Solder Alloys", *Proceedings of the 1996 International Symposium on Microelectronics*, Minneapolis, 1994.
- Zampino, M.A., and Jones, W.K., "Aluminum Nitride Ball/Pad Grid Array MCM-C/D", *1994 ISHM North Florida Symposium on Microelectronics*, Orlando, 1994. (Presentation)
- Zampino, M.A., Jones, W.K., Diaz, E., and Maltass, E., "Electrical Characterization of AlN Ball/Pad Grid Array MCM-C/D", *Proceedings of the 1994 International Symposium on Microelectronics*, Boston, 1994. (Presentation)
- Zampino, M.A. and Zhuge, R., "Finite Element Modeling of Multilayer Structures for Advanced Packages in MCM Applications", *1993 ISHM North Florida Symposium on Microelectronics*, Orlando, 1993. (Presentation)
- Zampino, M.A., Chellaiah, S. and Waters, R.A., "Experimental Study of Freezing of Binary Solutions", *AIAA Journal of Thermophysics and Heat Transfer*, Vol. 7(1), pp. 133-138, 1993.
- Chellaiah, S., Zampino, M.A., Waters, R.A., "Comparison of the Solidification of Aqueous Sodium Chloride with Augmenting and Opposing Thermosolutal Buoyancy Forces", *Journal of Materials Processing and Manufacturing Science*, Vol. 1(4), pp. 399-416, 1993.
- Chellaiah, S., Waters, R.A., and Zampino, M.A., "Solidification of An Aqueous Salt Solution in the Presence of Thermosolutal Convection", *Warme- und Stoffuebertrag*, Vol. 28, pp. 205-216, 1992.
- Zampino, M.A., Waters, R.A., and Chellaiah, S., "An Experimental Study of Freezing of Binary Mixtures", *Proceedings of the National Heat Transfer Conference*, Minneapolis, MN, 1991.